Thermodynamic and structural anomalies of water nanodroplets from computer simulations

by

©Shahrazad Malek

A thesis submitted to the School of Graduate Studies in partial fulfillment of the requirements for the degree of

PhD

Department of Physics and Physical Oceanography
Memorial University of Newfoundland

Memorial University of Newfoundland

August 24, 2018

ST. JOHN'S NEWFOUNDLAND

Abstract

Liquid water nanodroplets are valuable for studying supercooled water because they resist nucleation well below the bulk freezing temperature and conveniently self-pressurize in the interior. These features make nanodroplets good candidates for studying the properties of liquid water and for probing the liquid-liquid critical point (LLCP) in water hypothesized to exist in the deeply supercooled state at high pressure, at which a distinct low density liquid (LDL) phase becomes distinct from a high density liquid (HDL) phase.

We conduct extensive molecular dynamics computer simulations to study the properties of water nanodroplets using the TIP4P/2005 potential over a wide range of size and temperature. In order to improve the sampling of independent microstates, we conduct "swarms" of independent simulations, in which we monitor the approach to equilibrium from the potential energy autocorrelation function. After a swarm of this size attains equilibrium, the ensemble of final microstates from each run is sufficient to evaluate equilibrium properties and their uncertainties in the shortest real time.

In order to study the possibility of recovering bulk properties using nanodroplets, we evaluate the Laplace pressure inside the nanodroplets from direct evaluation of the local pressure tensor. We use a modification of a coarse-graining pressure tensor method that calculates the components of the microscopic pressure tensor as a

function of radial distance r from the centre of a spherical water droplet. The pressure tensor beneath the surface region becomes approximately isotropic and constant with r. From this region where the components of the pressure tensor are equal, we determine the Laplace pressure of the droplets.

Defining the pressure and the density inside the nanodroplets enables us to probe the properties of liquid water nanodroplet cores. We find that the bulk properties and related anomalies are present in the nanodroplets, such as the appearance of a density maximum. We simulate water nanodroplets under extremly low temperature conditions that have not been investigated thoroughly before. At such low temperatures, the nanodroplets show interesting emergence of structural complexity in the interior which may be linked to the LLCP and may indicate a HDL-like to LDL-like transformation in the nanodroplets.

We also study the surface tension of water nanodroplets using different approaches. When employing the thermodynamic route to calculating surface tension, we find that the Tolman correction is small and can be neglected. Therefore, the surface tension of nanodroplets can be approximated by the planar surface tension. We also observe a sudden increase in the planar surface tension at low temperature on crossing the Widom line, which may signal the emergence of a LDL-like network in the interior of water nanodroplets.

Co-Authorship

The thesis author (Shahrazad Malek) was the main contributor for all of the manuscripts included in this thesis, sharing authorship with Dr. Ivan Saika-Voivod and Dr. Peter Poole, the supervisors for this graduate project, Dr. Richard Bowles from University of Saskatchewan, and Dr. Francesco Sciortino from Sapienza University of Rome. This work resulted in three published manuscripts and a manuscript in preperation: one entitled *"Swarm relaxation": Equilibrating a large ensemble of computer simulations* published in the European Physical Journal E (Ch. 3), another entitled *Evaluating the Laplace pressure of water nanodroplets from simulations* published in the Journal of Physics: Condensed Matter (Ch. 4), the third work entitled *Thermodynamic and structural anomalies of water nanodroplets* published in Nature Communications (Ch. 5), and the fourth entitled *Surface tension of deeply supercooled* TIP4P/2005 *water nanodroplets using direct evaluation of the pressure tensor* (Ch. 6). In all four works, Dr. Saika-Voivod and Dr. Peter Poole assisted with checking the computer codes, analyzing data and writing the manuscripts. Dr. Peter Poole produced the Monte Carlo part reported in Ch. 3. Dr. Richard Bowles and Dr. Francesco Sciortino provided feedback on drafts of manuscript reported in Ch. 3 and Ch. 4. As a main contributor, Shahrazad Malek wrote all the analysis codes used in this thesis, performed 90% or more of the calculations, carried out literature reviews and wrote first drafts of the manuscripts, except for Ch. 3 which was drafted by Dr. Peter Poole with

input from all authors.

Acknowledgments

I thank God for everything He granted me in my life. I would like to thank my supervisors Dr. Ivan Saika-Voivod and Dr. Peter Poole for their trust in me, and for never giving me a feeling that I disappointed them during the learning process. I thank them for being patient and for their marvellous role as teachers in many aspects of life along my academic path. I would thank them for the absolutely amazing conversations I had with them.

I thank my committee members Dr. Martin Plumer and Dr. Mykhaylo Evstigneev. I have known Dr. Martin for six years now. Without a doubt, he is a source of wisdom and happiness for me.

I thank my mother Ibtihaj, my father Mohammad, and my siblings for their wonderful support, especially my beloved sister Camellia. As water plays a pivotal role on Earth, Camellia plays a pivotal role in my life.

A special shout-out to my friend Christopher Power, with whom I spend countless lovely and precious conversations. I thank Chris for the genuine smile he puts on my face. He is the one that helps me in my life while I am away from my family. And for that, I will always cherish our friendship until my last breath on this planet.

I thank Maureen Wade and Donna Coombs for their tremendously uplifting words when things start to become struggles. The same gratitude is due to all staff at MUN, especially Lisa O'Brien, Joy Simmons, Fred Perry ("Fred! You know what I would

say, eh?"), and John Jerrett.

Finally, I thank all my friends, especially Somayeh Khajehpour, Ahmad Almudallal, Sarah Ayoub, Tatsuo Izawa, and Razyeh Behbahani.

Table of Contents

Abstract **ii**

Co-Authorship **iv**

Acknowledgments **vi**

Table of Contents **xi**

List of Tables **xii**

List of Figures **xv**

Abbreviations **xvii**

1 Introduction **1**

1.1 Water: the key of life 1

1.2 Liquid-liquid phase transition 4

1.3 Water nanodroplets 8

1.4 Outline 10

2 Methodology **18**

2.1 The TIP4P/2005 model of water 18

2.2 Molecular Dynamics 20

2.3 Monte Carlo: Metropolis algorithm 22
Bibliography 25

3 "Swarm relaxation": Equilibrating a large ensemble of computer simulations 26

3.1 Abstract 26
3.2 Introduction 27
3.3 Definitions 30
3.4 Test cases 31
3.4.1 Bulk ST2 water 31
3.4.2 TIP4P/2005 water nanodroplet 39
3.5 Computational efficiency 44
3.6 Discussion 46
3.7 Acknowledgements 49
3.8 Author Contributions 49
3.9 Appendix: Fluctuations of the autocorrelation function 52

4 Evaluating the Laplace pressure of water nanodroplets from simulations 54

4.1 Abstract 54
4.2 Introduction 55
4.3 Simulations 58
4.4 Microscopic pressure 60
4.4.1 Pressure profiles 60
4.4.2 Comment on calculating $P_T(r)$ 68
4.4.3 Obtaining the local pressure from the potential energy 70
4.5 Results 71

4.5.1 Radial pressure profiles 71
4.5.2 Laplace pressure relation 74
4.6 Discussion and conclusions 75

5 Thermodynamic and structural anomalies of water nanodroplets 85
5.1 Abstract 85
5.2 Introduction 86
5.3 Results 89
5.3.1 Anomalous variation of the nanodroplet radius 89
5.3.2 Density profile of nanodroplets 93
5.3.3 Laplace pressure and equation of state for nanodroplets 95
5.3.4 Nanodroplet behaviour approaching the LLPT 98
5.4 Discussion 102
5.5 Methods 104
5.5.1 Computer simulations 104
5.5.2 Droplet definition 106
5.5.3 Relaxation times 107
5.5.4 Testing for crystal formation 107
5.5.5 Stability of liquid nanodroplets at low T. 108
5.5.6 Droplet radius 108
5.5.7 Voronoi volumes and isothermal compressibility 109
5.5.8 Surface region of density profiles 110
5.5.9 Laplace pressure 110
5.5.10 Error estimates 111
5.5.11 Data availability 111
5.6 Acknowledgements 117
5.7 Author contributions 117

5.8 Competing financial interests 117
5.9 Additional information 118
5.10 Supplementary information 118

6 Surface tension of deeply supercooled TIP4P/2005 water nanodroplets using direct evaluation of the pressure tensor 127

6.1 Abstract 127
6.2 Introduction 128
6.3 Simulations 133
6.4 Results 134
6.4.1 Surface tension 134
6.4.2 Local structure ordering 144
6.5 Discussion and conclusions 148
6.6 Acknowledgments 153

7 Summary and Future Work 157

7.1 Summary 157
7.2 Future work 159

List of Tables

2.1 Potential parameters of the TIP4P/2005. 19

3.1 Run parameters and time scales for each of our swarm relaxation test cases. 34

4.1 List of all 16 solution sets that contribute to coarse-grained pressure and the resulting limits of integration. 65

5.1 Run parameters and relaxation time scales for our SLR nanodroplet simulations for $N = 100$, 200, 360, and 776. 124

5.2 Run parameters and relaxation time scales for our SLR nanodroplet simulations for $N = 1100$, 1440, and 2880. 125

5.3 Run parameters and relaxation time scales for nanodroplet simulations carried out using the swarm relaxation method. 126

List of Figures

1.1 Phase diagram of water 2

1.2 Temperature range of water at atmospheric pressure. 4

1.3 Liquid-liquid coexistence line on the pase diagram of water. 6

1.4 Melting curves of ices III, IV, V, and XIII. 7

2.1 A sketch of the TIP4P/2005 water model. 19

2.2 Trial move in MC 23

3.1 time dependence of $\langle\rho\rangle$ and $\langle U\rangle$ for ST2 runs 32

3.2 C_ρ and C_U for ST2 runs 33

3.3 Relaxation times τ_ρ and τ_U for ST2 runs 34

3.4 $\langle\rho\rangle$ and $\langle U\rangle$ as a function of t for ST2 runs, plotted relative to the corresponding values of $\bar{\rho}$ or $\bar{U}$ 35

3.5 $\langle\rho\rangle$ for ST2 runs and $\langle U\rangle$ for ST2 and TIP4P/2005 runs as a function of $t/\bar{\tau}$ for ST2 38

3.6 $\tau_x/\bar{\tau}$ and $\tau_{\max}/\bar{\tau}$ versus $t/\bar{\tau}$, for ST2 and TIP4P/2005 runs 39

3.7 Comparison of our results for $\langle\rho\rangle$ and $\langle U\rangle$ for ST2 runs with ST2 data taken from Ref. [12] 40

3.8 Comparison of C_U from our TIP4P/2005 nanocluster runs 41

3.9 Time dependence of $\langle U\rangle$ for TIP4P/2005 runs 42

4.1 A sketch of all possible contributions to P in $\tilde{V}$ from the coarse-graining method 63
4.2 A sketch of the geometry for a sample calculation of the transverse pressure component at a radius r. 69
4.3 A sketch for the calculation of the derivative of the local potential energy $U(r)$ with respect to volume. 71
4.4 Pressure as a function of radial distance from the centre of a nanodroplet of size $N = 1100$ at $T = 220$ K. 72
4.5 Consistency check on the calculation of $P_N(r)$ and $P_T(r)$ for $N = 1100$ and $T = 220$ K. 74
4.6 Test of the Laplace pressure relation. 75

5.1 Snapshots of simulated liquid water nanodroplets. 88
5.2 Variation of nanodroplet radius R with temperature T and number of molecules N. 89
5.3 Equations of state for bulk liquid and nanodroplets of TIP4P/2005. . 90
5.4 Nanodroplet density profiles. 92
5.5 Density maximum of liquid nanodroplets. 93
5.6 Emergence of density differences within nanodroplets with decreasing temperature. 96
5.7 Laplace pressure inside nanodroplets. 97
5.8 Variation of density and pressure with temperature inside nanodroplets of various sizes. 99
5.9 Isothermal compressibility of the nanodroplet core. 102
5.10 Comparison of density profile definitions. 118
5.11 Nanodroplet density profiles. 119
5.12 Contributions to the pressure inside water nanodroplets. 120

5.13 Variation of the nanodroplet surface tension with temperature. 121
5.14 Variation with temperature of characteristic densities for nanodroplets. 122
5.15 Melting of nanocrystals. 123

6.1 Contributions to the pressure inside water nanodroplets as a function of r. 135
6.2 Isotherms of P_L as a function of R_e^{-1}. 137
6.3 Tolman length δ as a function of T obtained from different means. . . 138
6.4 Isotherms of $2/(P_L R_e)$ as a function of R_e^{-1}. 139
6.5 γ_s as a function of R_s^{-1}. 140
6.6 γ_s as a function of R_s^{-1} and R_e^{-1}. 141
6.7 The variation of planar surface tension γ_p with T. 142
6.8 Surface tension of curvature γ_s as a function of R_e at $T = 300$ K. . . 145
6.9 Isotherms of γ_s as a function of R_e. 146
6.10 d_5 and q_T as a function of radius r. 149
6.11 Local measures of structure as a function of density. 150

Abbreviations

CNT Classical Nucleation Theory

EOS Equation of State

HDA High Density Amorphous ice

HDL High Density Liquid

Ic Cubic Ice

Ih Hexagonal Ice

LDA Low Density Amorphous ice

LDL Low Density Liquid

LJ Lennard-Jones potential

LLCP Liquid-Liquid Critical Point

LLPT Liquid-Liquid Phase Transition

MC Monte Carlo

MCS Monte Carlo Step

MD Molecular Dynamics

mW Monatomic water model (involves short range and three-body interactions)

RTN Random Tetrahedral Network

SLR Single Long Run

ST2 5-site water model involving electrostatic and van der Waals interactions (1974)

TIP4P 4-site water model that includes electrostatic and van der Waals interactions

TIP4P/2005 A variant of TIP4P re-parameterized for better accuracy

TIP5P 5-site water model involving electrostatic and van der Waals interactions (2000)

Chapter 1

Introduction

1.1 Water: the key of life

Perhaps every one of us has the passion to understand the universe. Some are eagerly watching and studying enormous planets, while others are obsessed with small atoms. But if each one of us would pick one element that we are utterly fascinated by, I can fairly say the element would be water.

We all refer to water as the matrix of life [1]. There are countless reasons as to why water has such a privilege. The tremendous amount of water on our earth only is overwhelmingly impressive [2]. Water has not stopped fascinating us with its many unique and unusual properties. At sufficiently cold conditions, water exhibits anomalies, such as a density maximum at 4°C, and it becomes more compressible on cooling, while it becomes less viscous when compressed [3]. The anomalies of water become more pronounced as liquid water is supercooled further [2, 4]

Over decades, the richness of the phase diagram of water has attracted scientists in astrophysics, condensed matter physics, and chemistry; see Fig. 1.1. Water exists in three phases, gas, liquid, and solid [5]. Moreover, solid water can exist in different

crystal forms. Nine of the forms that have been identified to date are thermodynamically stable over a range of pressure P and temperature T [6, 7]. Water exists as a stable ice in hexagonal form (ice Ih) at atmospheric P (and up to about 100 MPa) in the T range between 72 and 273 K. It can also exist in two amorphous forms, namely, high density amorphous (HDA) ice and low density amorphous (LDA) ice [8].

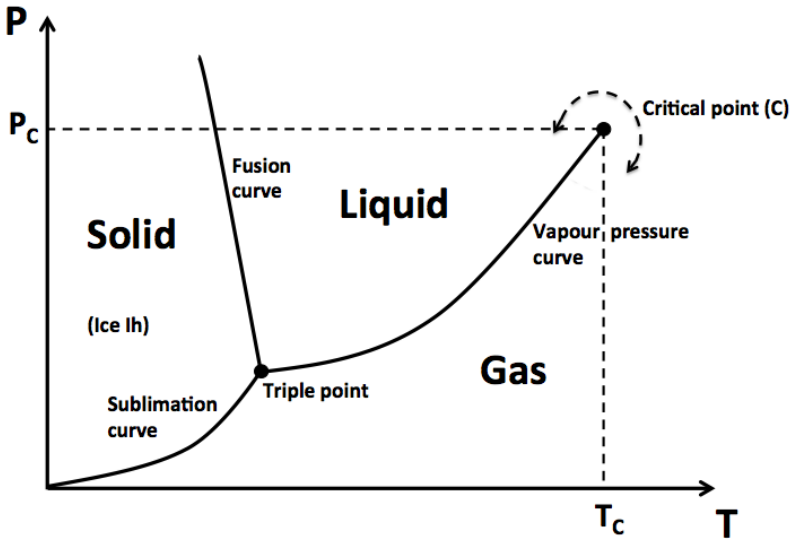

Figure 1.1: Phase diagram of water. A projection of coexistence lines of the $P(\rho, T)$ surface onto the P-T plane. Figure is adapted from Ref. [5]

The thermodynamic parameters, P, T, and density ρ, are connected through a functional relation called the equation of state (EOS), which forms a three dimensional surface, $f(P, \rho, T) = 0$. In the plane of P and T, these phases are separated by lines, called coexistence lines, where two phases can coexist with each other in equilibrium; see Figure 1.1.

The coexistence lines are the "fusion curve" between solid and liquid, the "sublimation curve" between solid and gas, and the "vapour pressure curve" between gas and liquid, which terminates at the "critical point". The three lines meet at the "triple point", where all phases are in equilibrium with each other.

The coexistence lines in Figure 1.1 are defined in the thermodynamic limit (num-

ber of particles $N \to \infty$, observation time $t \to \infty$). A phase of water, as for any other substance, can be observed as a metastable state on the other side of the coexistence line without undergoing a phase transition on a finite time scale [9]. For instance, water can exist for finite time below the freezing point 0°C in a liquid phase, where we call it supercooled water. The degree to which you can keep supercooled water in the liquid phase depends on the nucleation rate for crystallization. The experimental limit of supercooling for bulk water is 231 K at atmospheric pressure (1 bar) [10]. On a phase diagram, the limit of supercooled water at different P is called the homogeneous nucleation limit, T_h.

Figure 1.2 shows the temperature range for observing liquid water at atmospheric pressure. The lines correspond to coexistence temperatures, and the dotted lines correspond to metastability limits, where homogeneous nucleation to gaseous and crystal phases become unavoidable at T_{SH} and T_h respectively. Above the glass transition temperature T_g, there is a highly viscous form of liquid water that crystallizes to cubic ice (Ic) at T_x [2].

Intensive research on amorphous forms of water was spurred on by an important review article by Angell [11]. The two distinct forms of amorphous water are separated by an apparently first-order phase transition. One of the most important conclusions of this extensive and rich review is that supercooled liquid water and amorphous water are closely related. Therefore, a comprehensive understanding of metastable water requires understanding water in its supercooled and glassy states and the connection between them.

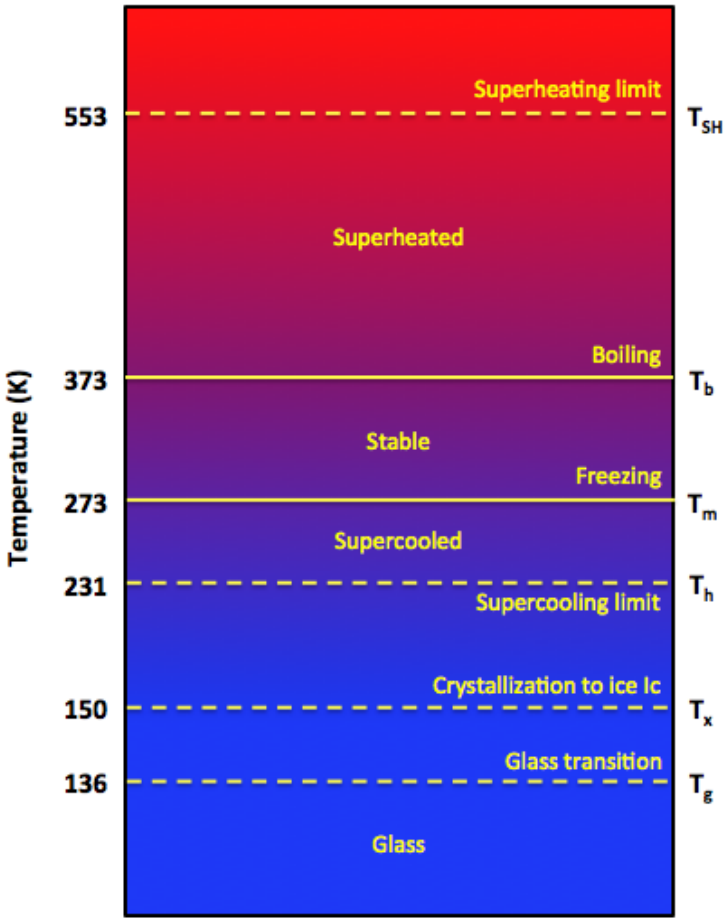

Figure 1.2: Temperature range of water at atmospheric pressure. The lines correspond to coexistence temperatures of the gaseous and liquid phases at T_b, and the solid and liquid phases at T_m. The dotted lines correspond to metastability limits for supercooling at T_h and superheating at T_{SH}. T_x corresponds to the temperature at which crystallization to cubic ice (Ic) occurs, while T_g is the glass transition temperature. Figure is adapted from Ref. [2]

1.2 Liquid-liquid phase transition

Water anomalies like the density maximum at 4°C, the minima in isothermal compressibility at 46°C and in isobaric heat capacity at 35°C, and the first-order-like transition between HDA and LDA inspired researchers to think of hypotheses to shed light on the source of water anomalies. The singularity-free hypothesis suggests that the transition between HDA and LDA is continuous [12, 13, 14]; see blue shaded area

in Fig. 1.3. The idea behind the hypothesis comes from the observation of a sharp increase in response functions at the transition, but the increase remains finite [15]. In this scenario, volume and entropy remain continuous and the fluctuations between HDA and LDA are finite. Consistent with this hypothesis, neutron and x-ray diffraction studies on the structural changes between HDA and LDA suggest the existence of multiple distinct amorphous forms of ice, which is interpreted as a result of a continuous transition [16]. However, the story did not end there.

The search for another explanation for water's anomalies continued to deepen. Another hypothesis came out to explain the first-order-like transition between HDA and LDA and its connection to metastable liquid. In 1992, Poole *et al*, studied water using computer simulations of the ST2 model [26, 24]. They observed that isothermal curves inflect at low T and high P. The inflection is similar to the one we see as we approach the region of a critical point. The authors explain the anomalies by the existence of a first order transition between two distinct metastable phases of water, high density liquid (HDL) and low density liquid (LDL), and that the coexistence line between these two phases terminates at a second liquid-liquid critical point (LLCP) in the metastable regime of water at low T and high P; see Fig. 1.3. The same line is believed to separate HDA and LDA. Harrington *et al.* [18] also observed inflections in the ST2 water EOS. They reported a 15% change in density at their lowest simulated temperature, $T = 235$ K, without any increase in pressure. Other computer simulation studies show that pressure-density isotherms using the TIP4P model [21], TIP4P/2005 [19, 23], and the TIP5P model [20, 22] show evidence of a LLCP at low temperatures.

A smart experiment on the melting of ice IV provided a strong observational evidence for the LLCP [25]. They found that ice IV- and V-liquid coexistence curves change slope abruptly when they intersect the proposed liquid-liquid coexistence line;

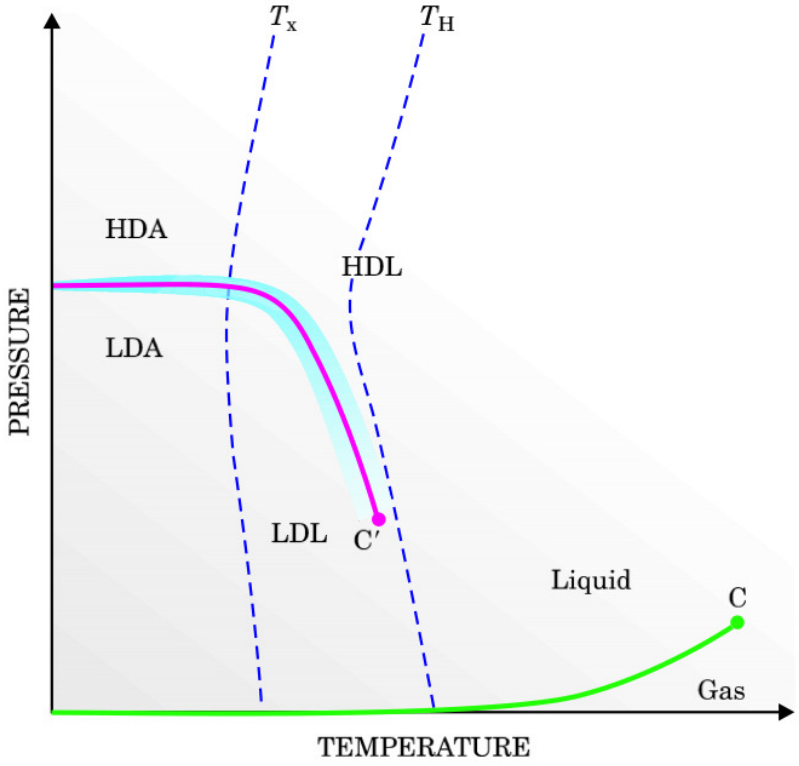

Figure 1.3: Liquid-liquid phase transition (LLPT) and liquid-liquid critical point (LLCP), C', locations on the phase diagram of water. The figure is taken from Ref. [2].

see Fig. 1.4. The smoothness of these melting curves except at the intersection is a sign that the abrupt change is related to the liquid phase of water rather than the solid.

Liu *et al.* conducted computer simulations of water using the ST2 model [27]. They calculated the free energy surface as a function of density and bond-orientational order under supercooled conditions. They found two distinct basins in the free energy surface related to HDL and LDL. They also observed flipping between the two phases. Moreover, studies on ST2 water done by Holten *et al.* [28] showed that the liquid-liquid transition is energy-driven, in contrast to the mW model of water [29], for which the transition is entropy-driven [30]. This implies that the two models should have

different behaviour at low T.

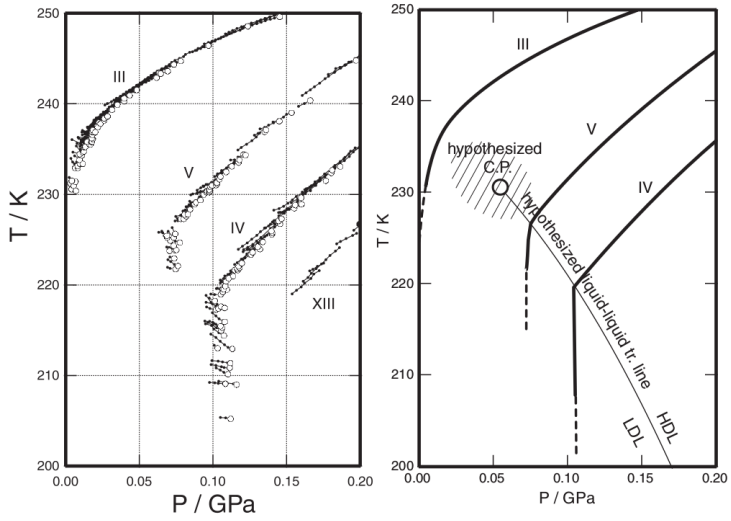

Figure 1.4: Melting curves of ices III, IV, V, and XIII. Left: experimental results. The empty circles are the onset of the change in the sample temperature. Right: schematic representation of the hypothesized first-order liquid-liquid transition line dividing the low- and high-density liquids (LDL and HDL) and the liquid-liquid critical point (LLCP). The LLCP is thought to exist in the hatched area. Used with permission from Ref. [26].

Several studies tried to locate the LLCP in the phase diagram of water in terms of critical temperature T_c, critical pressure P_c, and critical density ρ_c. Note that in this thesis, we use unprimed symbols to indicate the location of the second critical point of water, in contrast to the notation of Fig. 1.3.

Experimental results on high-pressure ices [43, 31] suggested that the location of the LLCP at the coordinates $T_c \simeq 220$ K, $P_c \simeq 100$ MPa, and $\rho_c \simeq 1\text{g/cm}^3$. Ni and Skinner [33] extrapolated the Kanno-Angell line from compressibility experiments and extrapolated the line of singularity temperatures from NMR relaxation experiments [34]. Their estimate of the of the LLCP is at $T_c \simeq 168$ K and $P_c \simeq 195$ MPa. This is similar to Kanno and Miyata's estimate of the LLCP using differential thermal analysis data of emulsified liquid water [35], where they find 145 K$< T_c \simeq 175$ K and $P_c \simeq 200$ MPa. Dougherty [36] found that the LLCP based on experimental data of

the homogeneous nucleation curve T_h and the temperature of maximum density curve T_{MD} is at $T_c \simeq 182$ K and $P_c \simeq 195$ MPa. Mishima in 2010 estimated the LLCP using water emulsions [37], and found that P_c is lower than other studies estimate, giving a new estimate of $T_c \simeq 223$ K and $P_c \simeq 50$ MPa.

The location of the LLCP is also explored using computer simulations. Tanaka found that the LLCP from molecular dynamics simulation for the TIP4P model of water is rather at negative pressure in the range between 0 and -200 MPa at $T_c \simeq 213$ K. However, using the ST2 model of water, Poole *et al.* estimated $T_c \simeq 235$ K and $P_c \simeq 200$ MPa. In 1998, Rosenfeld and Tarazona observed a transition between HDL and LDL at low temperatures using the SPC/E model of water, and estimated the LLCP at $T_c \simeq 130 \pm 5$ K and $P_c \simeq 290 \pm 30$ MPa. For a 5-site model of water, TIP5P, Yamada *et al.* locate the LLCP at $T_c \simeq 217 \pm 3$ K, $P_c \simeq 340 \pm 20$ MPa, and $\rho_c \simeq 1.13 \pm 0.04 \mathrm{g/cm^3}$. Ni and Skinner [33] carried out molecular dynamics simulations using the E3B3 model [33], and estimated the LLCP at $T_c \simeq 180$ K and $P_c \simeq 210$ MPa. Recently, the extensively studied water model, TIP4P/2005, assigned critical coordinates to the LLCP at $T_c \simeq 182$ K, $P_c \simeq 170$ MPa, and $\rho_c \simeq 1.13 \pm 0.04 \mathrm{g/cm^3}$ [44].

1.3 Water nanodroplets

As one can clearly see, the estimate of the LLCP varies widely for different experimental techniques and different simulation models of water. Also, the results of computer simulations differ from the extrapolation estimates of experimental data. Therefore, we propose the utilization of water nanodroplets to explore the behaviour of water in extreme conditions. Nanodroplets conveniently self-pressurize, and this pressure increases as the size of the nanodroplet N gets smaller. This eliminates the need to

subject water to high pressure via experimental apparatus to probe the LLCP. The small size of water nanodroplets reduces the freezing temperature and hence suppresses the nucleation. This helps study liquid water under low temperatures that are not accessible otherwise in bulk.

For their essential role in many systems, such as climate [45], interstellar space [46], and biomedical applications [47], water nanodoplets have been the focus of studies for quite some time. Maintaining water nanodroplets in the liquid state is essential to further probe bulk liquid properties and to determine to what extent they are expressed in nanodroplets. Galli *et al* [48] found, through computational studies, that crystal nucleation rates in nanodroplets are suppressed because of the Laplace pressure. The suppression of the melting temperature with decreasing nanodroplet radius was studied by Johnston *et al* [49] using the mW model. They also found that the crystallized nanodroplets comprised stacked Ih and Ic layers, similar to what is observed for small crystallites in bulk at the same low temperatures studied (150 to 200 K). The structure of quenched water nanodroplets was studied by Nandi *et al* [50] using molecular dynamics simulations. They found a dynamically arrested state that resembles the LDA form of glassy water, thus also finding evidence that nanodroplets are capable of behaviour associated with the bulk.

From the experimental side, Manka *et al* used small angle X-ray scattering to monitor the size distribution of nanodroplets formed in a supersonic nozzle and used Fourier Transform infrared spectroscopy to monitor crystallization occurring within the nanodroplets. This enabled them to determine nucleation rates for nanodroplets in a size range of 3.2 to 5.8 nm at T between 202 and 215 K, and thus they were able to push observation of the liquid state significantly below T_h. Further infrared spectroscopy studies showed that the onset of ice-like structure occurs in nanodroplets only at a size of 275 molecules [52], i.e., below this size, nanodroplets do not crystallize

at all. Thus, if the interiors of nanodroplets below this size have the properties of bulk water, then the liquid state can be studied with no interference from crystallization.

Utilizing water nanodroplets to study liquid water under high P and low T first requires establishing whether the Laplace pressure is high enough to probe the LLCP, and this depends on how the surface tension behaves with N and T. We also need to determine whether the interiors of nanodroplets reflect the properties of bulk water. For that, we carry out thorough investigations of water nanodroplet properties over a wide range of T and N.

1.4 Outline

In Ch. 2, we give an overview of the simulation techniques used in this thesis, where we use molecular dynamics and Monte Carlo simulations, and we modelled our water nanodroplets using the TIP4P/2005 potential. In Ch. 3 (*"Swarm relaxation": Equilibrating a large ensemble of computer simulations*) we detail our development of a method "swarm relaxation" that useful in getting an equilibrated data set in the shortest real time, when many processors are available, as in the case with high performance computing facilities. We present in Ch. 4 (*Evaluating the Laplace pressure of water nanodroplets from simulations*), details of how we modify a coarse-grained method for calculating the local pressure tensor in systems with spherical geometry in order to use it with the water model we employ. We present our main findings of thermodynamic and structural anomalies in nanodroplets in Ch. 5 (*Thermodynamic and structural anomalies of water nanodroplets*), where we show that the bulk anomalies manifest themselves in the nanodroplets, and that the Laplace pressure gets as high as 220 MPa at 180 K. We also see interesting density gradient in the interior of the nanodroplets for $T = 180$ and 200 K. In Ch. 6 (*Surface tension of deeply supercooled*

TIP4P/2005 *water nanodroplets using direct evaluation of the pressure tensor*) we investigate the behaviour of the surface tension of our strongly curved nanodroplets using two approaches, the thermodynamic and the mechanical routes. We also study one of the important issues with the surface tension of droplets, which is the sign and magnitude of the Tolman length, a length quantifying the variation of surface tension with the radius of the droplet. Interestingly, we observe a sudden increase in the surface tension at low T, which occurs on crossing the Widom line, the supercritical extension of the LLPT. Finally, we summarize our results and discuss future work in Ch. 7.

Bibliography

[1] F. Franks, *Water: A Matrix of Life.* (Royal Society of Chemistry, Cambridge, 2000)

[2] P. G. Debenedetti and H. E. Stanley, *Supercooled and Glassy Water.* Phys. Today, June 2003, page 40.

[3] H. Sato, K. Watanabe, J. M. H. Levelt Sengers, J. S. Gallagher, P. G. Hill, J. Straub, and W. Wagner, *Sixteen Thousand Evaluated Experimental Thermodynamic Property Data for Water and Steam.* J. Phys. Chem. **20**, 1023 (1991).

[4] L. G. M. Pettersson, R. H. Henchman, and A. Nilsson, *Water-The Most Anomalous Liquid.* Chem. Rev. **116**, 7459 (2016).

[5] H. E. Stanley, *Introduction to Phase Transition and Critical Phenomena* (Oxford University Press, New York and Oxford, 1971)

[6] V. F. Petrenko and R. W. Whitworth, *Physics of Ic* (Oxford University Press, Oxford, 1999)

[7] C. Lobban, J. L. Finney, and W. F. Kuhs, *The structure of a new phase of ice.* Nature **391**, 268 (1998).

[8] P. G. Debenedetti and H. E. Stanley, *The relationship between liquid, supercooled and glassy water.* Nature **396**, 329 (1998).

[9] A. N. Nevzorov, *Some Properties of Metastable States of Water.* Phys. Wave Phen. **14**, 45 (2006).

[10] F. Franks, *Water, a Comprehensive Treatise* (Plenum Press, New York, 1982)

[11] C. A. Angell, *Supercooled water.* Annu. Rev. Phys. Chem. **34**, 593 (1983).

[12] S. Sastry, P. G. Debenedetti, F. Sciortino, and H. E. Stanley, *Singularity-free interpretation of the thermodynamics of supercooled water.* Phys. Rev. E **53**, 6144 (1996).

[13] L. P. N. Rebelo, P. G. Debenedetti, and S. Sastry, *Singularity-free interpretation of the thermodynamics of supercooled water. II. Thermal and volumetric behavior.* J. Chem. Phys. **109**, 626 (1998).

[14] P. G. Debenedetti, *Supercooled and glassy water.* J. Phys. Condens. Matter **15**, 1669 (2003).

[15] Y. Xie, K. F. Ludwig, G. Morales, D. E. Hare, and C. M. Sorensen, *Noncritical behavior of density fluctuations in supercooled water.* Phys. Rev. Lett. **71**, 2050 (1993).

[16] C. A. Tulk, C. J. Benmore, J. Urquidi, D. D. Klug, J. Neuefeind, B. Tomberli, and P. A. Egelstaff, *Structural studies of several distinct metastable forms of amorphous ice.* Science **297**, 1320 (2002).

[17] P. H. Poole, F. Sciortino, U. Essmann, and H. E. Stanley, *Phase behaviour of metastable water.* Nature **360**, 324 (1992).

[18] S. Harrington, R. Zhang, P. H. Poole, F. Sciortino, and H. H. Stanley, *Liquid-Liquid Phase Transition: Evidence from Simulations.* Phys. Rev. Lett. **78**, 2409 (1997).

[19] C. Vega, *A general purpose model for the condensed phases of water:* TIP4P/2005. J. Phys. chem. **123**, 234505 (2005).

[20] M. W. Mahoney and W. L. Jorgensen, *A five-site model for liquid water and the reproduction of the density anomaly by rigid, nonpolarizable potential functions.* J. Phys. chem. **112**, 8910 (2000).

[21] W. L. Jorgensen, J. Chandrasekhar, and J. D. Madura, *Comparison of simple potential functions for simulating liquid water.* J. Phys. chem. **79**, 926 (1983).

[22] Y. Yamada, S. Mossa, H. E. Stanley, and F. Sciortino, *Interplay between time-temperature transformation and the liquid-liquid phase transition in water.* Phys. Rev. Lett. **88**, 195701 (2002).

[23] J. L. F. Abascala and C. Vega, *Widom line and the liquid–liquid critical point for the* TIP4P/2005 *water model.* J. Phys. chem. **133**, 234502 (2010).

[24] F. H. Stillinger, and A. Rahman, *Improved simulation of liquid water by molecular dynamics.* J. Phys. Phys. **60**, 1545 (1974).

[25] O. Mishima and H. E. Stanley, *Decompression-induced melting of ice IV and the liquid–liquid transition in water.* Nature **392**, 164 (1998).

[26] O. Mishima, *Liquid-Liquid Critical Point in Heavy Water.* Phys. Rev. Lett. **85**, 334 (2000).

[27] Y. Liu, J. C. Palmer, A. Z. Panagiotopoulos, and P. G. Debenedetti, *Liquid-liquid transition in* ST2 *water.* J. Chem. Phys. **137**, 214505 (2012).

[28] V. Holten, J. C. Palmer, P. H. Poole, P. G. Debenedetti, and M. A. Anisimov, *Two-state thermodynamics of the* ST2 *model for supercooled water.* J. Chem. Phys. **140**, 104502 (2014).

[29] E. B. Moore and V. Molinero, *Structural transformation in supercooled water controls the crystallization rate of ice.* Nature **479**, 506 (2011).

[30] V. Holten, D. T. Limmer, V. Molinero, and M. A. Anisimov, *Nature of the anomalies in the supercooled liquid state of the* mW *model of water.* J. Chem. Phys. **138**, 174501 (2013).

[31] P. W. Bridgman, *The Pressure-Volume-Temperature Relations of the Liquid, and the Phase Diagram of Heavy Water.* J. Chem. Phys. **3**, 597 (1935).

[32] O. Mishima and H. E. Stanley, *The relationship between liquid, supercooled and glassy water.* Nature **396**, 329 (1998).

[33] Y. Ni and J. L. Skinner, *Evidence for a liquid-liquid critical point in supercooled water within the* E3B3 *model and a possible interpretation of the kink in the homogeneous nucleation line.* J. Chem. Phys. **144**, 214501 (2016).

[34] E. W. Lang and H. -D. Lüdemann, *High Pressure O*-17 *Longitudinal Relaxation Time Studies in Supercooled* H_2O *and* D_2O. Ber. Bunsengesellschaft Phys. Chem. **85**, 603 (1981).

[35] H. Kanno and K. Miyata, *The location of the second critical point of water.* Chem. Phys. Lett. **422**, 507 (2006).

[36] R. C. Dougherty, *The PVT surface of water: critical phenomena near 0.195 GPa, 182 K.* Chem. Phys. **298**, 307 (2004).

[37] O. Mishima, *Volume of supercooled water under pressure and the liquid-liquid critical point.* J. Chem. Phys. **133**, 144503 (2010).

[38] V. Holten, C. E. Bertrand, M. A. Anisimov, and J. V. Sengers, *Thermodynamics of supercooled water.* J. Chem. Phys. **136**, 094507 (2012).

[39] P. G. Debenedetti, *Metastable Liquids: Concepts and Principles* (Princeton University Press, Princeton, 1996)

[40] H. Reiss, *Methods of Thermodynamics* (Blaisdell Publishing Company, New York 1965)

[41] S. P. Das, *Statistical Physics of Liquids at Freezing and Beyond* (Cambridge University Press, New York, 2011).

[42] F.F. Abraham, *Homogeneous nucleation theory; the pretransition theory of vapor condensation* (Acadmic Press, New York 1974))

[43] O. Mishima and H. E. Stanley, *The relationship between liquid, supercooled and glassy water.* Nature **396**, 329 (1998).

[44] M. A. González, C. Valeriani, F. Caupin, and J. L. F. Abascal, *A comprehensive scenario of the thermodynamic anomalies of water using the* TIP4P/2005 *model.* J. Chem. Phys. **145**, 054505 (2016).

[45] Ø. Wilhelmsen, T. T. Trinh, A. Lervik, V. K. Badam, S. Kjelstrup, and D. Bedeaux, *Coherent description of transport across the water interface: From nanodroplets to climate models.* Phys. Rev. E **93**, 032801 (2016)

[46] S. Tachibana, A. Kouchi, T. Hama, Y. Oba, L. Piani, I. Sugawara, Y. Endo, H. Hidaka, Y. Kimura, K. Murata, H. Yurimoto, and N. Watanabe, *Liquid-like behavior of UV-irradiated interstellar ice analog at low temperatures* Sci. Adv. **3**, eaao2538 (2017)

[47] H. Ohno, N. Nishimura, K. Yamada, Y. Shimizu, S. Iwase, J. Sugenoya, and M. Sato, *Effects of water nanodroplets on skin moisture andviscoelasticity during air-conditioning.* Skin Res. Technol. **19**, 375 (2013)

[48] T. Li, D. Donadio, and G. Galli, *Ice nucleation at the nanoscale probes no man's land of water.* Nat. Commun. **4**, 1887 (2013).

[49] Johnston, J.C. and Molinero V. *Crystallization, Melting, and Structure of Water Nanoparticles at Atmospherically Relevant Temperatures.* J. Am. Chem. Soc. **134**, 6650-6659 (2012).

[50] P. K. Nandi, C. J. Burnham, Z. Futera, and N. J. English, *Ice-Amorphization of Supercooled Water Nanodroplets in No Man's Land.* ACS Earth Space Chem. **1**, 187-196 (2017).

[51] A. Manka, H. Pathak, S. Tanimura, J. Wö lk, R. Strey, and B. E. Wyslouzil, *Freezing water in no-man's land.* Phys. Chem. Chem. Phys. **14**, 4505 (2012).

[52] C. C. Pradzynski, R. M. Forck, T. Zeuch, P. Slavicek, and U. Buck, *A fully size-resolved perspective on the crystallization of water clusters.* Science **337**, 1529-1532 (2012).

Chapter 2

Methodology

2.1 The TIP4P/2005 model of water

Intermolecular potential models of water have been developed for use in computer simulations. One of these models is called the TIP4P/2005 water model [1]. A water molecule consists of three atoms, two hydrogens H and one oxygen O. In this rigid model, the molecule has one more interaction site called the virtual (massless) site M; see Fig. 2.1. Charges are assigned to H and M, while O is left neutral. The M site is coplaner with O and H, and is located on the bisector of the H-O-H angle. The charged sites interact via the Coulomb potential,

$$u_{electrostatic}(r_{ab}) = \frac{e^2}{4\pi\varepsilon_0}\frac{q_a q_b}{r_{ab}} \tag{2.1}$$

where q_a and q_b stand for the charges on sites a and b, e is the charge of the electron, ε_0 is the permittivity of vacuum, and r_{ab} is the a-b distance.

The O sites interact via the Lennard-Jones (LJ) potential,

$$u_{LJ}(r_{\mathrm{OO}}) = 4\epsilon\left(\frac{\sigma^{12}}{r_{\mathrm{OO}}^{12}} - \frac{\sigma^{6}}{r_{\mathrm{OO}}^{6}}\right), \tag{2.2}$$

where r_{OO} is the O-O distance, and ϵ and σ are the LJ bond strength and distance parameters, respectively. The parameters are listed in Table 2.1.

Parameter	Value
σ (nm)	0.31589
ϵ (KJ/mol)	0.7749
r_{OM} (nm)	0.01546
r_{OH} (nm)	0.09572
$q_H(e)$	+0.5564
$q_O(e)$	0.0
$q_M(e)$	-1.1128
$\measuredangle$ HOH (°)	104.52

Table 2.1: Potential parameters of the TIP4P/2005. These values are taken from Ref. 79.

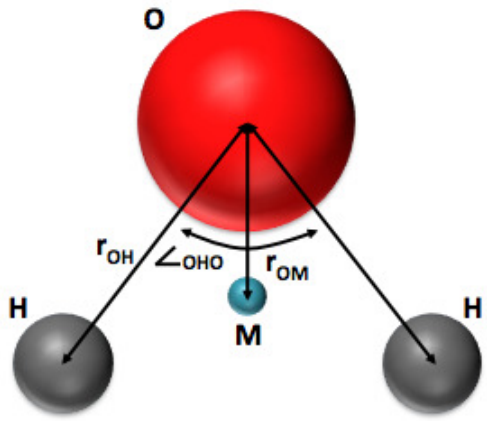

Figure 2.1: A sketch of the TIP4P/2005 water model.

A droplet of water can be simulated as a collection of these model molecules. Different microstates of the droplet can be sampled through molecular dynamics (MD) or Monte Carlo (MC) simulations. The bulk of this thesis uses MD because it provides the opportunity to study dynamics. MC yields thermodynamic quantities only. However, MC does provide the opportunity to study rare events, such as nucleation,

through biased sampling techniques.

2.2 Molecular Dynamics

In molecular dynamics (MD), we solve numerically the equations of motion of a system consisting of N_p atoms [2, 3]. For a given particle, the equation is,

$$\mathbf{f}_i = m_i \ddot{\mathbf{r}}_i, \tag{2.3}$$

where m_i is the mass of atom i, $\ddot{\mathbf{r}}_i$ is the acceleration of atom i given by the second derivative of the atom coordinate $\mathbf{r}_i$ with respect to time t, and $\mathbf{f}_i$ is the force on i due to all other atoms in the system. The force on i due to atom j is given by,

$$\mathbf{f}_{ij} = -u'(r_{ij}) \frac{\mathbf{r}_{ij}}{r_{ij}} \tag{2.4}$$

where $\mathbf{r}_{ij} = \mathbf{r}_i - \mathbf{r}_j$ is the displacement vector from i to j, and r_{ij} is the distance between i and j. The derivative of the potential $u(r_{ij})$ depends of the kinds of atoms, i.e., if the atoms are O, then the force between them is given by the derivative of Eq. 2.2 with respect to r_{OO}, while if the atoms are charges, then the force between them is given by the derivative of Eq. 2.1 with respect to r_{ab}. Therefore, the net force on i, required for Eq. 2.3, is given by the sum over all pairs of atoms,

$$\mathbf{f}_i = \sum_{j \neq i}^{N_p} \mathbf{f}_{ij}. \tag{2.5}$$

Solving Eq. 2.3, for all N_p atoms will determine positions $\mathbf{r}$ and velocities $\mathbf{v}$ of all atoms in the system as a function of t, given initial values for $\mathbf{r}$ and $\mathbf{v}$ for each particle.

In our simulations, we use the "leap-frog" algorithm that numerically solves for $\mathbf{r}$ and $\mathbf{v}$ in such a way that one quantity is half a time step from the other. The algorithm takes the form,

$$\mathbf{v}\left(t+\frac{\delta t}{2}\right) = \mathbf{v}\left(t-\frac{\delta t}{2}\right)+\delta t\,\mathbf{f}\left(t\right)/m \tag{2.6}$$

$$\mathbf{r}\left(t+\delta t\right) = \mathbf{r}\left(t\right)+\delta t\,\mathbf{v}\left(t+\frac{\delta t}{2}\right), \tag{2.7}$$

where δt is the time step. The current velocity is calculated by,

$$\mathbf{v}\left(t\right) = \frac{1}{2}\left(\mathbf{v}\left(t+\frac{\delta t}{2}\right)+\mathbf{v}\left(t-\frac{\delta t}{2}\right)\right). \tag{2.8}$$

One then can use Eq. 2.8 to find the system kinetic energy,

$$K=\frac{1}{2}\sum_{i=1}^{N_p} m_i v_i^2, \tag{2.9}$$

while the system potential energy is given by,

$$U=\sum_{i=1}^{N_p-1}\sum_{j>i}^{N_p} u(r_{ij}), \tag{2.10}$$

where $u(r_{ij})$ is given by Eq. 2.1 or Eq. 2.2, and interactions between atoms in the same molecule are ignored. $U(t)$ is required to find the total energy of the system,

$$E(t) = U(t)+K(t). \tag{2.11}$$

The energy is a conserved quantity for an isolated system in the microcanonical ensemble, and therefore the invariance of E with t is a test on the algorithm that provides a way of checking that the step size is sufficiently small.

As discussed in section 2.1, TIP4P/2005 treats the water molecule as a rigid molecule, and as such the water molecule is subject to bond and angular constraints. However, the leap-frog integrator calculates the motion of the atoms in the system assuming a complete absence of intermolecular rigid bond forces, and therefore, we use the SHAKE algorithm [4] to modify velocities and positions to satisfy the constraints.

For the canonical ensemble (constant number of molecules N, volume V, and temperature T), T is kept constant with the Nosé-Hoover thermostat algorithm [5, 6].

In summary, MD generates new microstates by computing forces to propagate the system in time. MD is widely used in situations where we need to study dynamic properties of the system.

2.3 Monte Carlo: Metropolis algorithm

In contrast with MD, the Monte Carlo (MC) method generates new microscopic states by randomly displacing and rotating molecules, usually one molecule at a time. These rototranslational moves are accepted or rejected according to criteria derived from the statistical ensemble we wish to simulate [2, 3].

Our MC simulations are based on the Metropolis algorithm [2, 3], where a random molecule is chosen and is translated by a random trial displacement **dr**, and rotated by a random angle θ about a randomly chosen axis; see Fig. 2.2. An upper limit dr_{max} to the magnitude of each component of **dr** is set in this algorithm to avoid a dramatic change in the system energy. Also the rotation angle θ of the chosen molecule is confined within $\pm\theta_{max}$, for the same reason. These limits are chosen to give an acceptance ratio around 40% [7].

The rototranslational move is accepted with a probability that depends on the

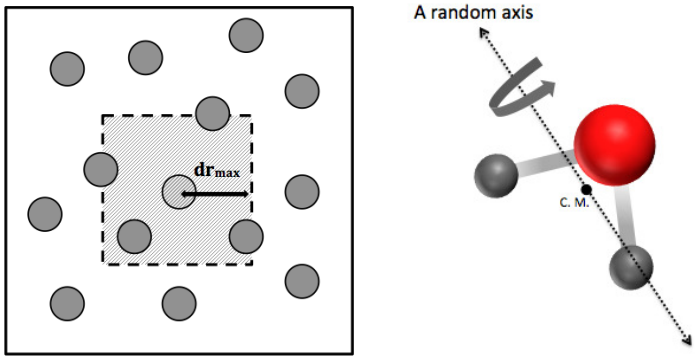

Figure 2.2: Trial move in MC. A sketch shows the chosen molecule (shaded sphere), which is moved anywhere in the shaded area and then rotated within a specified angular range.

change in the potential energy of the system resulting from the move,

$$P_{\text{accept}}(r_i^{\text{trial}}) = \left\{ \begin{array}{ll} 1 & \text{if } U_{\text{current}} \geq U_{\text{trial}} \\ \exp\left[-\beta(U_{\text{trial}} - U_{\text{current}})\right] & \text{if } U_{\text{current}} < U_{\text{trial}}. \end{array} \right\},$$

where $\beta = 1/k_B T$, k_B is the Boltzmann constant, $U_{current}$ refers to the potential energy before the rototranslational move, and U_{trial} referes to the potential energy after the rototranslational move. This definition of P_{accept} means that the the rototranslational move is accepted if it lowers U, and accepted with a non-zero probability if it increases U.

If the trial rototranslational move is rejected, then the current configuration is kept (i.e., its properties are counted again in any average being calculated), and is used as the starting point for the next trial rototranslational move. If the trial rototranslational move is accepted, the new configuration replaces the current one and its properties are used in determining any ensemble average.

Since dr_{max} and θ_{max} control the size of particle displacement and rotation, it is necessary to chose an optimal value for both. Otherwise, the simulation becomes

costly and inefficient. If dr_{max} is too small, most trial rototranslational moves will be accepted since the energy changes will be small, but the exploration of configurational space will be slow. If dr_{max} is too big, then trial rototranslational moves are likely to result in unfavourable interactions, leading to near certainty of rejection. Previous work has shown that an acceptance rate of 20-40% is optimal in most cases [7].

Bibliography

[1] J. L. F. Abascal and C. Vega, *A general purpose model for the condensed phases of water.* J. Chem. Phys. **123**, 234505 (2005).

[2] M. P. Allen and D. J. Tildesley, *Computer simulation of liquids* (Oxford University Press, New York, 1989).

[3] D. Frenkel and B. Smit, *Understanding Molecular Simulation: From Algorithms to Applications* (Academic, New York, 2002).

[4] J. P. Ryckaert, G. Ciccotti, H. J. C. Berendsen, *Numerical Integration of the Cartesian Equations of Motion of a System with Constraints: Molecular Dynamics of n-Alkanes.* J. Comput. Phys. **23**, 327 (1977).

[5] S. Nosé, *A unified formulation of the constant temperature molecular dynamics method.* J. Chem. Phys. **81**, 511 (1984).

[6] S. Nosé, *A molecular dynamics method for simulation in the canonical ensemble.* Mol. Phys. **52**, 255 (1984).

[7] C. R. C. Buhariwalla, R. K. Bowles, I. Saika-Voivod, F. Sciortino, and P. H. Poole, *Free energy of formation of small ice nuclei near the Widom line in simulations of supercooled water.* Eur. Phys. J. E **38**, 39 (2015).

Chapter 3

"Swarm relaxation": Equilibrating a large ensemble of computer simulations

3.1 Abstract

It is common practice in molecular dynamics and Monte Carlo computer simulations to run multiple, separately-initialized simulations in order to improve the sampling of independent microstates. Here we examine the utility of an extreme case of this strategy, in which we run a large ensemble of M independent simulations (a "swarm"), each of which is relaxed to equilibrium. We show that if M is of order 10^3, we can

monitor the swarm's relaxation to equilibrium, and confirm its attainment, within $\sim 10\bar{\tau}$, where $\bar{\tau}$ is the equilibrium relaxation time. As soon as a swarm of this size attains equilibrium, the ensemble of M final microstates from each run is sufficient for the evaluation of most equilibrium properties without further sampling. This approach dramatically reduces the wall-clock time required, compared to a single long simulation, by a factor of several hundred, at the cost of an increase in the total computational effort by a small factor. It is also well-suited to modern computing systems having thousands of processors, and is a viable strategy for simulation studies that need to produce high-precision results in a minimum of wall-clock time. We present results obtained by applying this approach to several test cases.

3.2 Introduction

When conducting a molecular dynamics or Monte Carlo computer simulation study of an equilibrium system, a key question is: "How long should we run?" First, equilibrium must be attained and verified, and then a sufficient number of independent microstates of the system must be sampled within equilibrium to allow for the accurate evaluation of equilibrium properties. In a traditional approach, all of this is achieved in a single long run (SLR). In this context, a run is "long" if it is many times (usually 100 times or more) longer than the equilibrium relaxation time $\bar{\tau}$ of the slowest relaxing, unconstrained observable of the system. When using a SLR, the evaluation of equilibrium properties relies on the ergodic hypothesis, i.e. that a sufficiently long time average of an observable is equal to the ensemble average taken over a set of independently generated microstates [1].

While perfectly sound in principle, a SLR can produce inaccurate results if $\bar{\tau}$ is underestimated. This can occur in simulations of supercooled liquids and glassy systems

exhibiting subtle and very slow structural relaxation [2], or in complex systems (such as proteins) where metastable basins of the free energy landscape trap the system for time scales that are long compared to the time required to explore the metastable basin itself [3]. In these cases, a SLR may appear to achieve equilibrium when in fact it has not.

As a consequence of these concerns, it is increasingly common to initiate multiple, independently initialized simulation runs to test for slow relaxation and trapping in metastable states [4, 3, 5, 6]. This strategy also takes advantage of the multi-processor structure of virtually all modern computing systems, since independent simulations can run concurrently on separate processors. Simulation studies of aging in glassy materials have long used this approach, in order to average over different realizations of the disorder in the initial configuration [7, 8].

When using multiple runs to study an equilibrium system, the final results are averaged both in time (within a single run) and over the ensemble of independent runs. Here we study the extreme case of an ensemble of runs in which the number of runs M is so large that no time averaging is required to obtain accurate results. Herein, we refer to such a large ensemble of runs as a "swarm". That is, we create a swarm of M independent runs, bring each to equilibrium, and use only the last microstate of each run to evaluate the equilibirum properties, which are computed purely as ensemble averages.

Our motivation to study this extreme case is to minimize the wall-clock time required to obtain the final results: The shortest possible run that produces an equilibrium microstate is a run that just reaches equilibrium and then stops. If a swarm of M such runs is carried out concurrently, and if M is large enough to produce an accurate ensemble average, then the wall-clock time to obtain results of a given precision will be substantially less than for a SLR. While it is apparent that this strategy

can produce accurate results if M is large enough, and if the runs are long enough, it is not obvious that the reduction in the wall-clock time will be worth the increase in the total computational cost, compared to a SLR. The efficiency of such a "swarm relaxation" strategy, relative to a SLR, will depend on the ability to stop the swarm runs just as they relax to equilibrium. However, we usually don't know the time scale to reach equilibrium in advance.

In the following, we study several test cases of the swarm relaxation approach, using Monte Carlo and molecular dynamics simulations of water. Simulations of water display a wealth of complex phenomena, carefully studied in many previous works, making this system an excellent choice for testing new computational strategies. We test the swarm relaxation approach by examining the time dependence of average properties, and their variance, during the evolution of the swarm to equilibrium, and also examine the properties of the autocorrelation functions and relaxation times of these observables. For several test cases, we show that when M is large enough (of order 10^3 or greater), the establishment of equilibrium can be detected from the time evolution of the average properties of the swarm on a time scale which is not much longer than the time scale separating independent equilibrium microstates in a single run. We also show that such values of M are sufficient to accurately evaluate equilibrium properties. For our test cases, when all M simulations in the swarm run concurrently, we show that a dramatic decrease of the wall-clock time is achieved (a factor of several hundred), in return for a much smaller increase in the total computational cost (a factor of not more than 3), relative to a SLR. Thus a swarm relaxation strategy is a viable approach for exploiting large-scale multi-processor computing systems to substantially reduce the wall-clock time required to evaluate equilibrium properties.

3.3 Definitions

Consider an ensemble of M independent runs in which an observable $x(i,t)$ is measured in run i of the ensemble as a function of time t. In the following we use $\langle \cdots \rangle$ to denote an ensemble average over the runs at fixed t. The ensemble average of x over all runs at a fixed t is defined as,

$$\Big\langle x(t) \Big\rangle = \frac{1}{M} \sum_{i=1}^{M} x(i,t). \tag{3.1}$$

The variance of x is,

$$\sigma_x^2(t) = \left\langle \Big[x(i,t) - \Big\langle x(t) \Big\rangle \Big]^2 \right\rangle, \tag{3.2}$$

where σ_x is the standard deviation of x at fixed t, which characterizes the average deviation of x from $\langle x \rangle$ at time t. Since $\langle x \rangle$ is an average of M completely independent values of x, the standard deviation of the mean $s_x = \sigma_x / \sqrt{M}$ characterizes the error in our estimate of $\langle x \rangle$.

Following standard practice, we define the autocorrelation function for x, as measured from a reference time t_0, as,

$$C_x(t_0,t) = \frac{\left\langle \Big[x(i,t_0) - \Big\langle x(t_0) \Big\rangle \Big] \Big[x(i,t) - \Big\langle x(t) \Big\rangle \Big] \right\rangle}{\sigma_x(t_0)\, \sigma_x(t)}. \tag{3.3}$$

As a function of the time difference $\Delta t = t - t_0$, C_x measures the decay of the correlations between the fluctuations of x from the ensemble average $\langle x \rangle$ occurring at t, and the fluctuations occurring at t_0. We emphasize that only ensemble averaging is used in the definition of C_x. Since our ensemble of runs is large, there is no need to average over different choices of the time origin t_0 in order to obtain an accurate value for C_x, as is commonly done when evaluating an autocorrelation function from a SLR.

This feature allows us to compute C_x for any value of t_0 both during the approach to equilibrium, as well as after equilibrium has been established.

As documented in the Appendix, it is straightforward to show that the standard deviation of fluctuations of C_x as $C_x \to 0$ is exactly $M^{-1/2}$. This result is important in the present context because it establishes how large M must be in order to effectively use C_x to monitor the relaxation of the ensemble of runs to equilibrium. If we choose $M = 1000$, then $1/\sqrt{M} = 0.032$, and so when C_x approaches zero, it will do so with fluctuations that remain within $\pm 2/\sqrt{M} = \pm 0.064$ of zero for 95% of the time. As we will see below, this error is sufficiently small to allow for the accurate evaluation of the relaxation time for the system, starting from any given t_0.

3.4 Test cases

3.4.1 Bulk ST2 water

Our first test case is a Monte Carlo simulation of bulk water, using the ST2 intermolecular potential. We employ the ST2 model of water in the original form proposed by Stillinger and Rahman [9], using the reaction field method to approximate the long-range contribution of the electrostatic interactions [10]. ST2 water has been extensively studied in previous work, mainly to investigate the liquid-liquid phase transition that occurs in the supercooled region of the phase diagram for this model. As a consequence, there is a rich literature of published work to which we can compare our results [13, 12, 13, 14, 15]. The ST2 simulations presented here are part of a larger study of ice nucleation in supercooled water, to be published separately [16].

Our Monte Carlo simulations of ST2 water are carried out in the constant-(N, P, T) ensemble, with $N = 1728$ molecules contained in a cubic simulation cell, with periodic boundary conditions. One Monte Carlo step (MCS) consists of (on av-

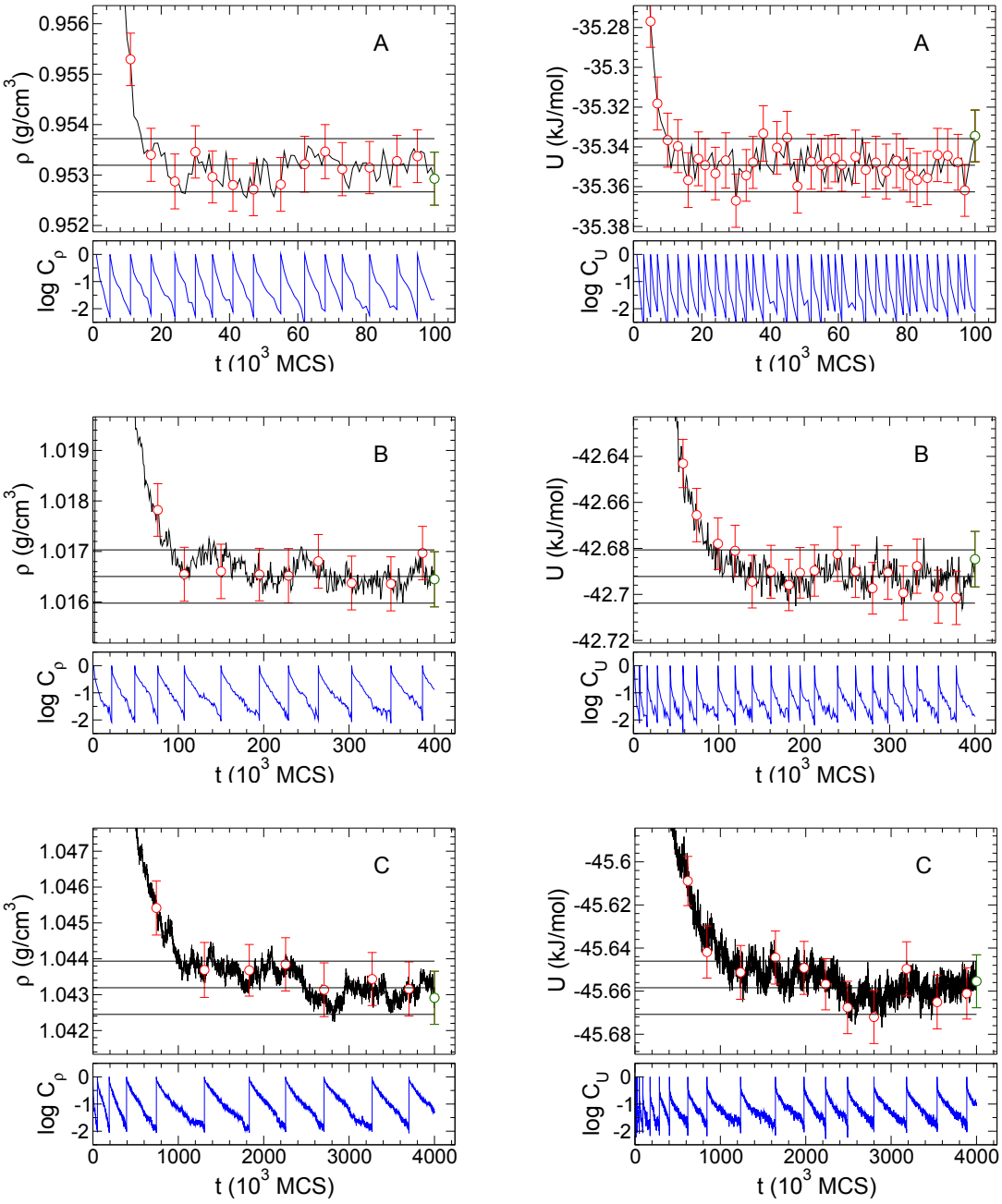

Figure 3.1: Black curves show the time dependence of $\langle\rho\rangle$ (left panels) and $\langle U\rangle$ (right panels) for ST2 runs A, B, and C (panels top to bottom). The black horizontal lines identify $\bar{\rho}$ and $\bar{\rho} \pm 2\bar{s}_\rho$ (left panels); and $\bar{U}$ and $\bar{\rho} \pm 2\bar{s}_U$ (right panels). The bottom section of each panel shows $\log C_\rho$ (left panels) and $\log C_U$ (right panels) over successive relaxation cycles, calculated as described in the text. The red circles in the left panels are values of $\langle\rho\rangle$ (with error $\pm 2s_\rho$) at the beginning of each relaxation cycle, and the green circle is $\langle\rho\rangle$ at $t = t_{\rm run}$. Similarly, the red circles in the right panels are values of $\langle U\rangle$ (with error $\pm 2s_U$) at the beginning of each relaxation cycle, and the green circle is $\langle U\rangle$ at $t = t_{\rm run}$.

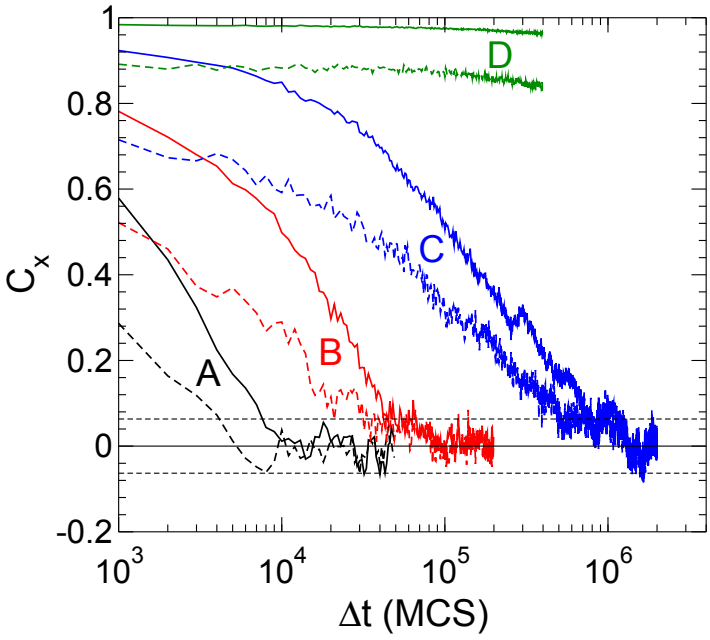

Figure 3.2: C_ρ (solid lines) and C_U (dashed lines) for ST2 runs A, B, C and D. The horizontal dotted lines identify $C_x = \pm 2M^{-1/2}$. Here $\Delta t = t - t_0$, with $t_0 = t_{\rm run}/2$.

erage) of $N-1$ attempted rototranslational moves, and one attempted change of the system volume. The maximum size of the attempted rototranslational and volume changes are chosen to give MC acceptance ratios in the range 30% to 40%.

To initialize a swarm of independent runs, we generate $M = 1000$ different configurations, each of which consists of N water molecules with their centers of mass arranged on a simple cubic lattice of density $\rho = 1.0$ g/cm^3, and with randomized molecular orientations. These configurations are used to initialize a swarm of runs at $T = 400$ K and $P = 100$ MPa (labelled run A in Table 3.1). Each run in this swarm is carried out for a run time of $t_{\rm run} = 10^5$ MCS.

As summarized in Table 3.1, the final configurations generated in run A are used to initialize two new swarm runs, B and C. Run B aims to characterize a state point on the ice-liquid coexistence line for ST2 water, and run C studies a state point close to the liquid-liquid critical point of ST2 water. The final configurations of run C are then used to initialize a swarm of runs D, which studies a low temperature state at

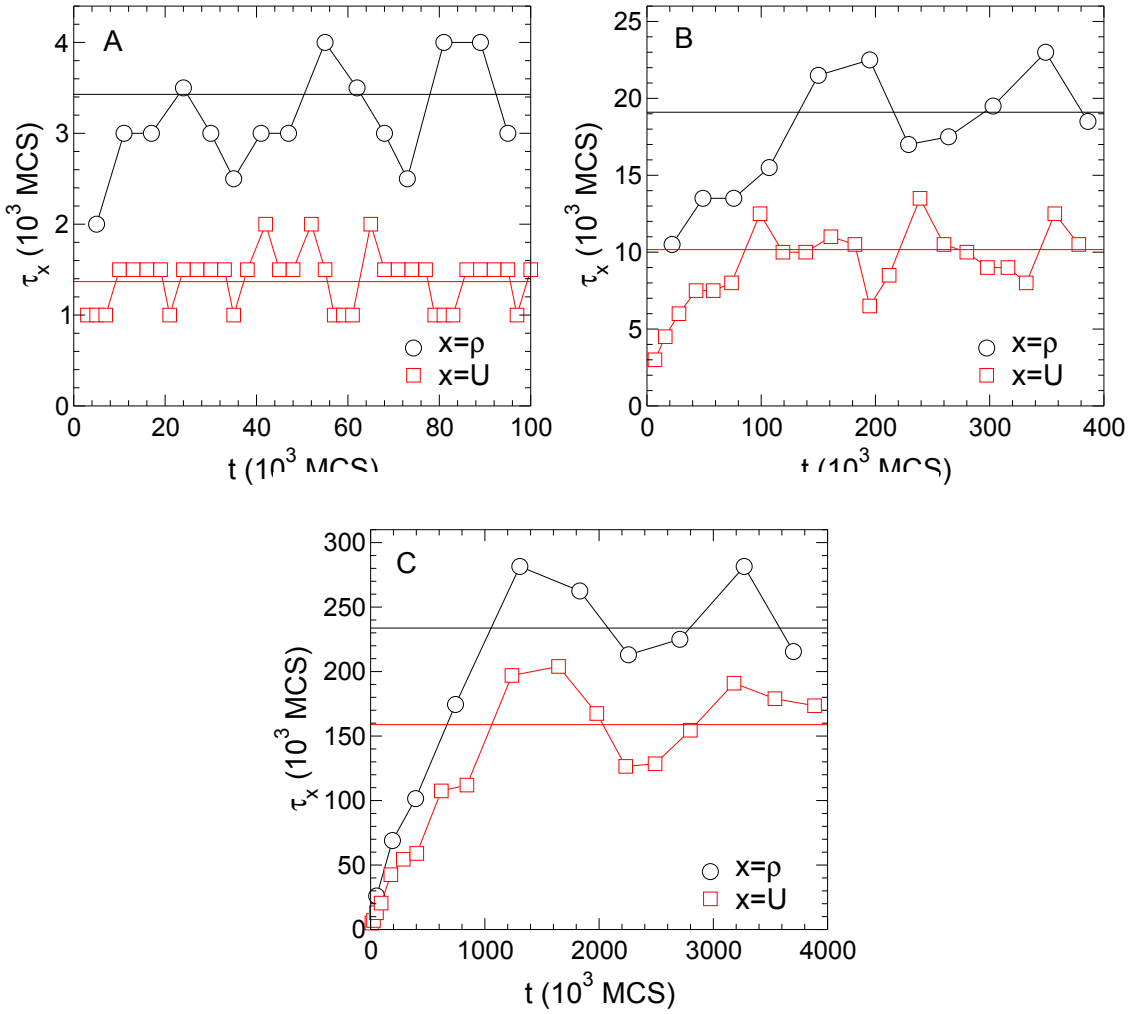

Figure 3.3: Relaxation times τ_ρ (black) and τ_U (red) for ST2 runs A, B, and C (panels top to bottom). Horizontal lines indicate the values of $\bar{\tau}_\rho$ (black) and $\bar{\tau}_U$ (red). Note that each value of τ_x is plotted at the value of t corresponding to t_0 at the end of the relaxation cycle from which τ_x is computed.

swarm run label	T (K)	P (MPa)	started from	$t_{\rm run}$ (10^3 MCS or ns)	$\bar{\tau}$ (10^3 MCS or ns)	$t_{\rm run}/\bar{\tau}$	$t_{\rm stop}$ (10^3 MCS or ns)	$t_{\rm stop}/\bar{\tau}$
A	400	100	random	100	3.4	29	41	12
B	290	120	A	400	19	21	229	12
C	250	190	A	4000	230	17	3270	14
D	100	190	C	800	$\gg 10^3$	$\ll 1$	$\gg 10^3$	-
E	180	-	SLR at 180 K	24	1.8	13	23	13
F	180	-	SLR at 220 K	24	1.9	13	23	12

Table 3.1: Run parameters and time scales for each of our swarm relaxation test cases. Symbols and abbreviations are as defined in the text. Time units are MCS for runs A, B, C and D, and are ns for E and F.

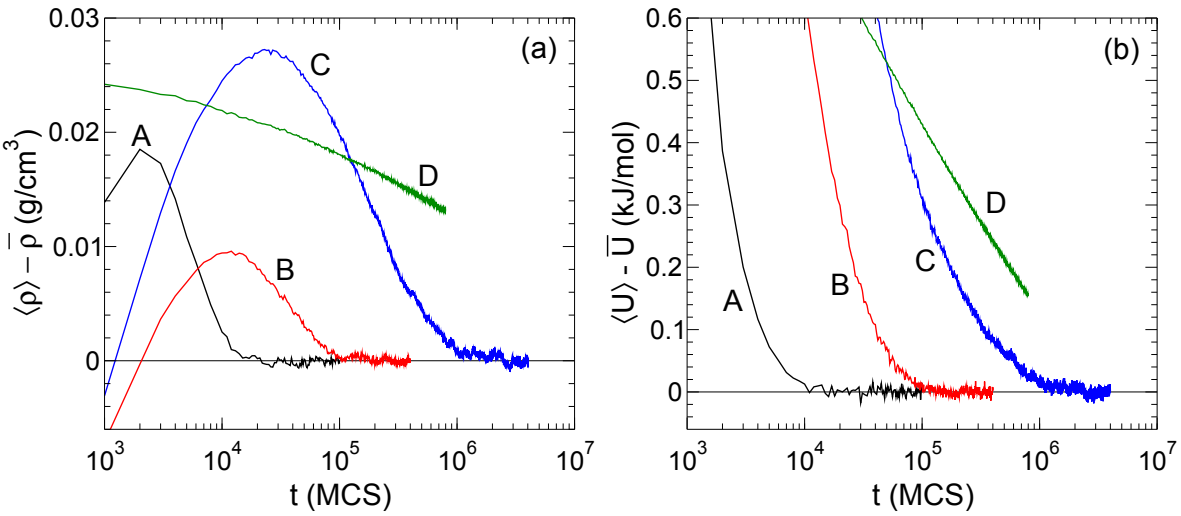

Figure 3.4: $\langle\rho\rangle$ (a) and $\langle U\rangle$ (b) as a function of t for ST2 runs A, B, C and D, plotted relative to the corresponding values of $\bar{\rho}$ or $\bar{U}$, and using a logarithmic time axis. In the case of run D, $\bar{\rho}$ and $\bar{U}$ are not known. To allow comparison with the other curves, for run D we arbitrarily set $\bar{\rho} = 1.04$ g/cm^3 in (a) and $\bar{U} = -51.8$ kJ/mol in (b).

which the system is quenched into a glass, and where (as we will see) the system is unable to achieve liquid-like equilibrium on the time scale currently accessible to simulations. Table 3.1 gives the values of T, P, and $t_{\rm run}$ for each of these ST2 swarm runs.

Fig. 3.1 shows the time dependence of the ensemble-averaged density $\langle\rho\rangle$ and the potential energy $\langle U\rangle$ for swarm runs A, B, and C. In each case, $t = 0$ corresponds to the set of microstates used to initialize the ensemble, as indicated in Table 3.1. For runs A, B, and C, $t_{\rm run}$ is sufficiently large that the time dependence of $\langle\rho\rangle$ and $\langle U\rangle$ in Fig. 3.1 suggests that an approximately steady state has been attained for $t > t_{\rm run}/2$, if not earlier. For each ensemble, we evaluate the time average of $\langle\rho\rangle$ and $\langle U\rangle$ for $t_{\rm run}/2 < t < t_{\rm run}$, respectively denoted $\bar{\rho}$ and $\bar{U}$. In each panel of Fig. 3.1, the horizontal solid line passing through the middle of the data at large t identifies the corresponding value of $\bar{\rho}$ or $\bar{U}$. The horizontal lines that bracket $\bar{\rho}$ and $\bar{U}$ identify values at $\bar{\rho} \pm 2\bar{s}_\rho$ and $\bar{U} \pm 2\bar{s}_U$ respectively, where $\bar{s}_\rho$ and $\bar{s}_U$ are time averages of s_ρ

and s_U for $t_{\rm run}/2 < t < t_{\rm run}$. We see in Fig. 3.1 that the fluctuations of $\langle\rho\rangle$ and $\langle U\rangle$ are largely confined to the ranges $\bar{\rho} \pm 2\bar{s}_\rho$ and $\bar{U} \pm 2\bar{s}_U$ in the second half of each run. This behavior is consistent with $\langle\rho\rangle$ and $\langle U\rangle$ having reached equilibrium, since in this case we would expect them to fluctuate within a range of $\pm 2\bar{s}_x$ for 95% of the time.

Fig. 3.2 shows C_ρ and C_U for runs A, B and C evaluated as a function of Δt for $t_0 = t_{\rm run}/2$, a time by which equilibrium has been established according to the results presented in Fig. 3.1. The time scale for the decay of C_ρ and C_U to zero therefore reflects the equilibrium relaxation time of each state point. We find in each case that C_ρ and C_U decay to zero in a time that is shorter than $t_{\rm run}/2$, confirming that our runs are able to relax completely within equilibrium. The dotted horizontal lines in Fig. 3.2 locate $\pm 2M^{-1/2}$. We find that the fluctuations of C_x as $C_x \to 0$ are largely confined within these bounds, as predicted in Section 3.3.

We also evaluate C_ρ and C_U for various values of t_0, shown as the blue "saw-tooth" curves in Fig. 3.1. These curves are calculated as follows: Starting at $t_0 = 10^3$ MCS, we evaluate the decay of C_x as a function of t, for both $x = \rho$ and $x = U$. At the next smallest time such that $C_x < e^{-2}$, we reset t_0 to the current time, and continue evaluating C_x. This process is repeated for the duration of the run, thus generating a saw-tooth curve that quantifies successive cycles of relaxation, both as the ensemble evolves towards equilibrium, and after equilibrium has been established.

As shown in Fig. 3.1, we find that the decay of C_x is approximately exponential (i.e. $\log C_x$ is linear in t), especially in the case of C_ρ. We therefore define the relaxation time τ_x as 1/2 of the time required for C_x to first reach e^{-2} during each relaxation cycle. Fig. 3.3 shows τ_ρ and τ_U as a function of t for runs A, B and C. Consistent with Fig. 3.1, Fig. 3.3 shows that τ_x is approximately constant in the 2nd half of our runs. We note that τ_x initially increases with t before reaching a steady state. This is to be expected for runs B and C in part because the initial

configurations come from runs at higher T, where the equilibrium relaxation time is shorter. Also, in all cases, the system is far out of equilibrium at the beginning of the runs, providing a strong initial driving force for change, demonstrated by the rapid decay of the autocorrelation functions at early times.

To characterize the average equilibrium relaxation time $\bar{\tau}$ for each state point, we first compute $\bar{\tau}_\rho$ and $\bar{\tau}_U$, the average values of τ_ρ and τ_U for $t_0 > t_{\rm run}/2$. We then define $\bar{\tau} = \max\{\bar{\tau}_\rho, \bar{\tau}_U\}$, to ensure that we use the most conservative choice of the relaxation time available. The values for $\bar{\tau}$ so obtained are given in Table 3.1. We note in all cases that $\bar{\tau}_\rho$ is greater than $\bar{\tau}_U$.

In each panel of Fig. 3.1, the open red symbols present values of $\langle\rho\rangle$ and $\langle U\rangle$ at the values of t_0 that mark the beginning of a new relaxation cycle in the saw-tooth curve for C_x. The error bars on each data point represent $\pm 2s_\rho$ and $\pm 2s_U$ respectively, the instantaneously calculated error in $\langle\rho\rangle$ and $\langle U\rangle$. These data demonstrate that the error in $\langle\rho\rangle$ and $\langle U\rangle$ does not vary significantly with t during the evolution of the swarm to equilibrium. These data also show that the instantaneous values of $\langle\rho\rangle$ and $\langle U\rangle$ attain values that are within error of $\bar{\rho}$ and $\bar{U}$ well before $t_{\rm run}/2$.

Fig. 3.4 shows $\langle\rho\rangle$ and $\langle U\rangle$ plotted with a logarithmic time axis. The time dependence of $\langle\rho\rangle$ exhibits a non-monotonic approach to the equilibrium value, possibly arising from the time separation between the vibrational and configurational degrees of freedom [17, 18]. Fig. 3.4 also confirms that a stable equilibrium has been attained at large t for runs A, B, and C. Fig. 3.5 shows the time dependence of $\langle\rho\rangle$ and $\langle U\rangle$, where the time has been scaled by $\bar{\tau}$. Fig. 3.6(a) shows a similar plot for the time dependence of τ_ρ. Figs. 3.5 and 3.6(a) demonstrate that in all cases, equilibrium thermodynamic properties and equilibrium relaxation times are established on a time scale of $10\bar{\tau}$ or less.

To test if the present results agree with previously reported results for ST2 water,

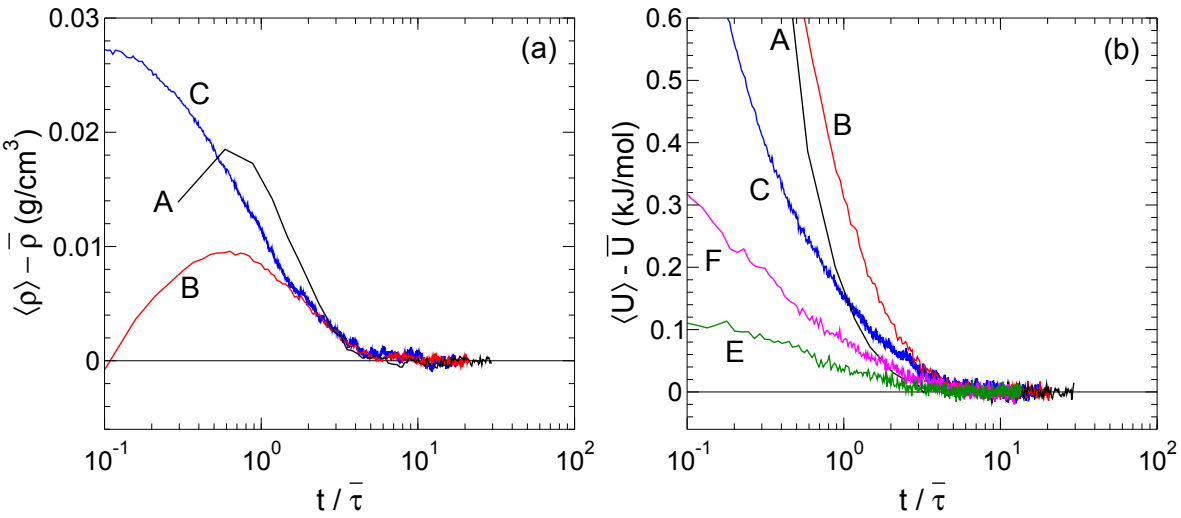

Figure 3.5: (a) $\langle\rho\rangle$ as a function of $t/\bar{\tau}$ for ST2 runs A, B and C, plotted relative to the corresponding value of $\bar{\rho}$. (b) Same as in (a) but for $\langle U\rangle$, and comparing both our ST2 runs (A, B and C) and TIP4P/2005 runs (E and F).

Fig. 3.7 compares our results for $\langle\rho\rangle$ and $\langle U\rangle$ from runs A, B, and C with results for ST2 water based on the data set generated for Ref. [12]. The data reported in Ref. [12] was obtained from constant-(N,V,T) molecular dynamics simulations with $N = 1728$. To conduct this comparison, we use the values of $\langle\rho\rangle$ and $\langle U\rangle$ evaluated at $t = t_{\rm run}$ (green open symbols in Fig. 3.1). The agreement between the two data sets is excellent, and again confirms that we have obtained equilibrium properties using our swarm relaxation strategy. Note in Fig. 3.7 that the error for our data points ($\pm 2s_x$) is much smaller than the symbol size. The scatter in the data points taken from Ref. [12] is larger, indicating that the estimates obtained here are of higher precision that those reported in Ref. [12].

In the case of run D, as expected, the swarm does not reach equilibrium on the time scale of our simulations. In Fig. 3.2 we see that both C_ρ and C_U remain very far from zero throughout the simulation time. Fig. 3.4 shows that both $\langle\rho\rangle$ and $\langle U\rangle$ continue to vary with t even at the largest t. It is apparent that a much longer simulation would be required to bring run D into equilibrium. Our results from run

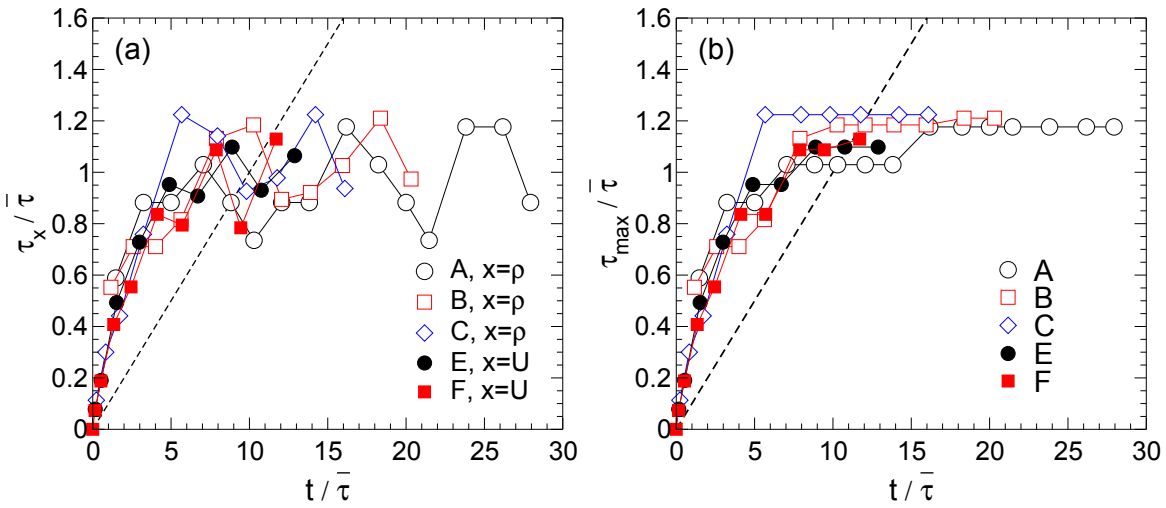

Figure 3.6: (a) $\tau_x/\bar{\tau}$ and (b) $\tau_{\max}/\bar{\tau}$ versus $t/\bar{\tau}$, for runs A, B, C, E and F. Note that each value of τ_x or $\tau_{\max}$ is plotted at the value of t corresponding to t_0 at the end of the relaxation cycle from which it is computed. The dashed line has slope 1/10.

D confirm that the swarm relaxation strategy used here is able to clearly distinguish between a liquid and a glassy state.

3.4.2 TIP4P/2005 water nanodroplet

As a second test case, we present molecular dynamics simulations of an isolated nanodroplet of $N = 360$ water molecules, surrounded by vacuum. In this case, the water interactions are modelled using the TIP4P/2005 potential [19]. These simulations are also used in a study of water nanodroplets over a wide range of N and T [20]. In the present simulations, we focus on $T = 180$ K, where T is controlled using a Nosé-Hoover thermostat [21, 22]. We use a cubic simulation cell of linear dimension L =10 nm, with periodic boundary conditions. The liquid nanodroplet occupies less than 2% of the total volume of the simulation cell. Since the diameter of the nanodroplet is significantly smaller than $L/2$, we directly evaluate all electrostatic interactions among molecules separated by a distance of less than $L/2$, and ignore interactions beyond this distance.

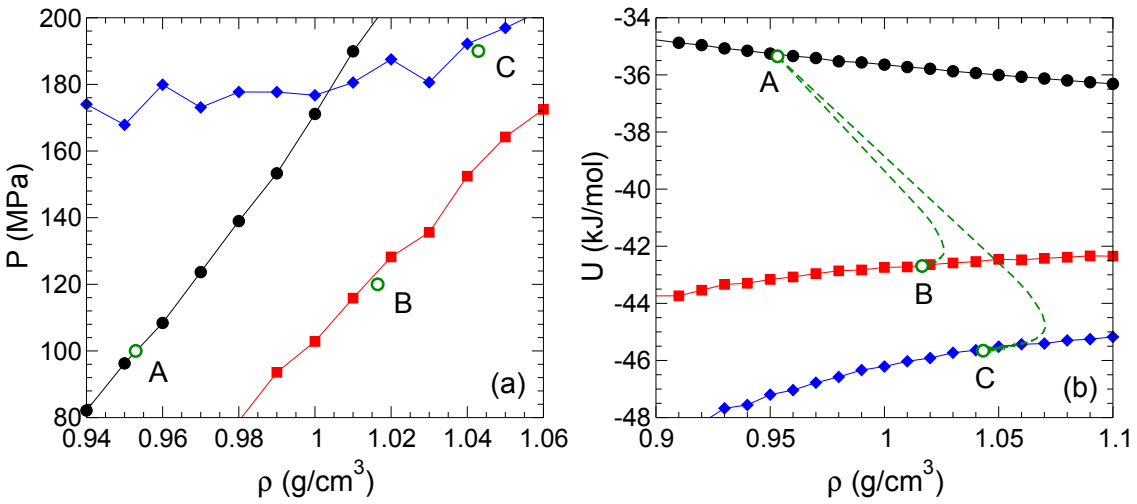

Figure 3.7: Comparison of our results for $\langle\rho\rangle$ and $\langle U\rangle$ for ST2 runs A, B and C (open green circles) with ST2 data taken from Ref. [12] (filled symbols). The error for the green circles is smaller than the symbol size in both plots. Panel (a) shows isotherms of P versus ρ from Ref. [12] for $T = 400$ K (black), 290 K (red), and 250 K (blue). Panel (b) shows isotherms of U versus ρ from Ref. [12] for the same T as in (a). In (b) we also show the parametric curves (green dashed lines) for $\langle\rho\rangle$ and $\langle U\rangle$ for runs B and C as they evolve from their starting values at A to their equilibrium values.

First we conduct a SLR of this 180 K nanodroplet lasting 2700 ns, to compare to our swarm runs. The initial configuration for this SLR is an equilibrium configuration taken from a single long nanodroplet simulation conducted at 250 K. The potential energy U is recorded every 40 ps during the SLR at 180 K. From the time series for U over the last 288 ns of the SLR, we evaluate the autocorrelation function using the definition in Eq. 3.3, but where the ensemble average is replaced by an average over the choice of time origin t_0. This autocorrelation function, plotted in Fig. 3.8, exhibits a fast initial decay, due to large fluctuations which occur on a time scale of less than 40 ps, followed by a slower relaxation to zero. Since it is the slower relaxation to zero that we wish to characterize, we coarse grain the time series by averaging our data for U over successive, non-overlapping time windows of 200 ps. The autocorrelation function for the coarse grained time series is also shown in Fig. 3.8. As desired, the coarse grained time series yields an autocorrelation function that better spans the full

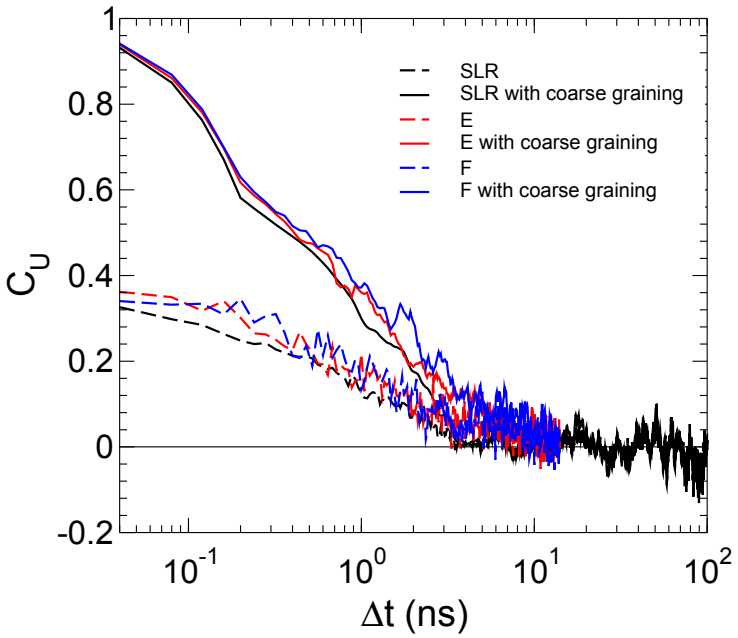

Figure 3.8: Comparison of C_U from our TIP4P/2005 nanocluster runs. Shown are C_U for the SLR (black), and the swarm runs E (red) and F (blue). Note that $\Delta t = t - t_0$. For runs E and F, we choose $t_0 = 10$ ns. Results for C_U both with (solid) and without (dashed) coarse graining are shown.

range of decay from 1 to 0 within the time domain studied here. Fig. 3.8 shows that the relaxation time $\bar{\tau}$ for our SLR is on the order of 1 ns, confirming that this run is long enough for measuring equilibrium properties.

We then conduct two swarm relaxation runs of the $N = 360$ TIP4P/2005 water nanocluster, labelled E and F in Table 3.1. To initialize run E, we select one equilibrium configuration from the SLR conducted at 180 K, and generate $M = 1000$ copies, where we use the same spatial coordinates for the molecules in the system, but select their velocities (both translational and rotational) randomly from a Maxwell-Boltzmann distribution appropriate for $T = 180$ K. To initialize run F, we proceed in the same way as for run E, except that the initial configuration is an equilibrium configuration obtained from a separate SLR conducted at $T = 220$ K. We choose this

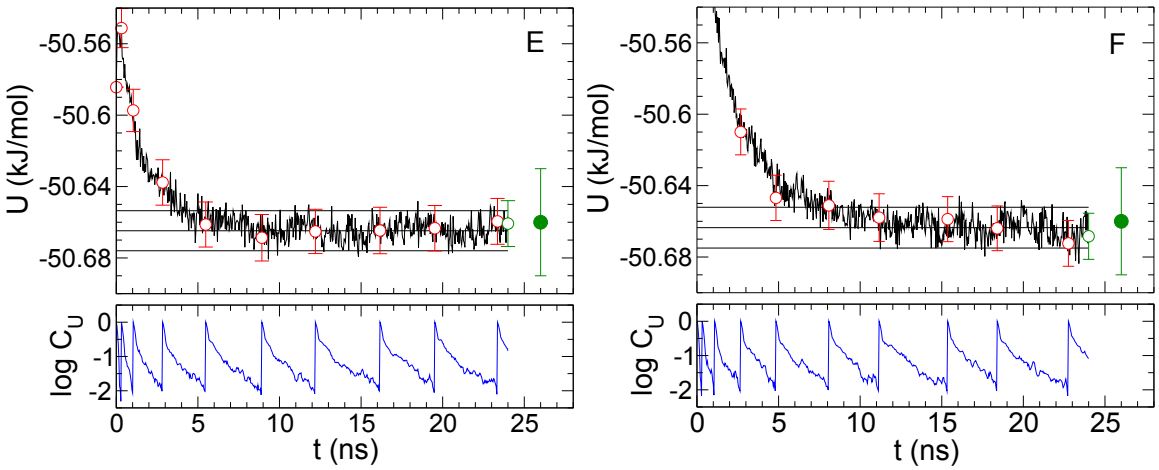

Figure 3.9: Time dependence of $\langle U \rangle$ (black curve) for TIP4P/2005 runs E and F (panels top to bottom). The black horizontal lines identify $\bar{U}$ and $\bar{U} \pm 2\bar{s}_U$. The lower section of each panel shows $\log C_U$ (evaluated from the coarse grained times series for $\langle U \rangle$) over successive relaxation cycles, as described in the text. The red circles are values of $\langle U \rangle$ (with error $\pm 2 s_U$) at the beginning of each relaxation cycle. The green open circle is $\langle U \rangle$ at $t = t_{\rm run}$. The green filled circle (displayed arbitrarily at $t = 26$ ns) is $\bar{U}$ from our SLR, evaluated with error as described in the text.

approach to test the use of an "isoconfigurational" [23] set of microstates to initialize a swarm relaxation run. We anticipate that there may be many situations where a single configuration of a complex system is available, either near or away from the state we wish to equilibrate. In this case, an isoconfigurational set is a convenient way to initialize a swarm relaxation run, compared to generating M independent configurations from scratch. Also, runs E and F will allow us to compare the time to recover the ensemble-average properties at $T = 180$ K when starting from a single equilibrium microstate (E), versus an out-of-equilibrium microstate (F).

For runs E and F, our swarm relaxation simulations run for $t_{\rm run} = 24$ ns. Fig. 3.9 shows the time dependence of $\langle U \rangle$ obtained for E and F, as well as the successive relaxation cycles of C_U. Fig. 3.9 demonstrates that $\langle U \rangle$ for both E and F is in a steady state when $t > t_{\rm run}/2$. We note that despite the fact that the initial configuration used

for run E is from the equilibrium portion of a SLR at the same conditions, its value of U is well outside, and above, the error estimate for $\bar{U}$. This occurs because σ_U is much greater than s_U, and so it is likely that a randomly chosen single configuration from equilibrium will fall outside of $\bar{U} \pm 2\bar{s}_U$. We also note that when calculating C_U from our swarm runs, we coarse grain the time series of U values for each run in the same way as described above for the SLR. The values of τ obtained from the successive relaxation cycles are shown as the solid symbols in Fig. 3.6(a), where we have used $\bar{\tau} = 1.8$ ns for run E, and $\bar{\tau} = 1.9$ ns for run F, evaluated by averaging the values of τ from runs E and F for $t_{\rm run}/2 < t < t_{\rm run}$.

In Fig. 3.8 we plot C_U as obtained from runs E and F, when $t_0 = 10$ ns, and using both the original and coarse grained time series for U. We find that the autocorrelation functions obtained from the SLR for $T = 180$ K and from the swarm runs E and F agree within error, confirming that the equilibrium relaxation time $\bar{\tau}$ is the same in all cases.

By time averaging over the last 288 ns of the SLR at $T = 180$ K, we obtain $\bar{U} = -50.66 \pm 0.03$. Here the error has been evaluated as $2\sigma/\sqrt{N_\tau}$, where σ is the standard deviation of the time series for U, and $N_\tau = (288\,\text{ns})/\bar{\tau}$, with $\bar{\tau} = 1.8$ ns. That is, we have made the (optimistic) assumption that successive independent configurations are separated by $\bar{\tau}$ in the SLR. This value of $\bar{U}$ is plotted as the solid green circle in both panels of Fig. 3.9, which demonstrates that the equilibrium value of U obtained from the swarm runs E and F, and the SLR, all agree within error. Our results also show that the equilibrium values of τ (Fig. 3.6) and $\langle U \rangle$ [Fig. 3.5(b)] in runs E and F are established within a run time of $10\bar{\tau}$, regardless of whether our swarm runs are initiated from an equilibrium or out-of-equilibrium configuration.

3.5 Computational efficiency

The above results indicate that all investigated test cases attain equilibrium within a time less than $10\bar{\tau}$. This time scale is physically reasonable: When the equilibrium we seek to attain is more slowly relaxing than the state point from which our swarms are launched, it is not surprising that the time scale to reach equilibrium is dominated by the time scale for relaxation within equilibrium. We define $\bar{\tau}$ as the time to relax an equilibrium autocorrelation function to $1/e$, and so full decorrelation requires several $\bar{\tau}$; e.g. $5\bar{\tau}$ is required for an exponential autocorrelation function to decay to less than 0.01, and longer would be required for a stretched exponential. Hence our test swarms reach equilibrium in less than two full decorrelation times of the equilibrium system.

For our swarm relaxation strategy to be both accurate and efficient, the runs need to be stopped at a time t_{stop} that is longer than the time required for the system to attain equilibrium, but not much longer. That is, if each run only contributes one microstate to the ensemble averages, then continuing the runs in the equilibrium time regime is a waste of computing resources. Based on the results shown above, $t_{\text{stop}} = 10\bar{\tau}$ would be a good choice, but $\bar{\tau}$ is not known in *a priori*. However, a reliable estimate for t_{stop} can still be made due to the fact that we can monitor τ as a function of t during the simulations. In the present context, by τ we mean the time-dependent relaxation time for the most slowly relaxing observable of interest.

In particular, it is reasonable to assume that the approach of τ to $\bar{\tau}$ (from below) is approximately exponential in t. If we also assume that $\tau = \bar{\tau}$ for $t > 10\bar{\tau}$, then the function $\tau(t)$ will lie above the linear curve $t/10$ from $t = 0$ to some time $t \leq 10\bar{\tau}$, and will lie below $t/10$ for $t > 10\bar{\tau}$. The time at which the curves for $\tau(t)$ and $t/10$ cross thus provides a way to estimate (an upper bound on) $\bar{\tau}$. We see in Fig. 3.6(a) that such a crossing is observed in each case studied here.

We therefore propose the following procedure to determine t_{stop}: Let $\tau_{\max}(t)$ be

the largest value of τ observed so far in a swarm run of length t. We define $t_{\rm stop}$ as the smallest t satisfying $t > 10\tau_{\rm max}(t)$. This procedure allows $t_{\rm stop}$ to be identified using only information that is available at time t. We use $\tau_{\rm max}(t)$ instead of $\tau(t)$ in order to make the estimate of $t_{\rm stop}$ a conservative one. In Fig. 3.6(b) we plot $\tau_{\rm max}(t)$ for each state point, from which we obtain estimates for $t_{\rm stop}$ from the crossing time of the curves for $\tau_{\rm max}(t)$ and $t/10$. These values of $t_{\rm stop}$ are tabulated in Table 3.1. In all cases, we find $t_{\rm stop}$ is larger than $10\bar{\tau}$, but not too much larger; $t_{\rm stop}/\bar{\tau}$ ranges between 12 and 14.

Next, we compare the efficiency of our swarm relaxation strategy relative to a SLR. Let us denote the time separation between independent microstates during a run as $n\bar{\tau}$, leaving open for the moment what a good choice of n should be. A SLR that generates K independent microstates will run for a wall-clock time of $t_{\rm SLR} = n\bar{\tau}K$. Here we ignore the equilibration time of a SLR, by assuming that this is a small fraction of the total run length. Using the swarm relaxation approach, and the procedure described above to determine $t_{\rm stop}$, each run will terminate after approximately $13\bar{\tau}$. Using M processors concurrently, subject to the constraint $M \leq K$, the swarm approach will generate K independent microstates in a wall-clock time of $t_{\rm swarm} = 13\bar{\tau}K/M$. The swarm strategy is thus faster, in terms of wall-clock time, than a SLR by a speedup factor of $f_{\rm speedup} = t_{\rm SLR}/t_{\rm swarm} = nM/13$. The total computational cost for a swarm run relative to a SLR increases by a factor of $f_{\rm cost} = Mt_{\rm swarm}/t_{\rm SLR} = 13/n$.

As for the choice of n, many simulation studies consider microstates to be independent if they are separated by as little as $\bar{\tau}$; see e.g. Ref. [24]. However, this choice almost certainly underestimates the error in a SLR, relative to the error evaluated in a swarm run. As discussed above, complete decorrelation requires several $\bar{\tau}$, e.g. $n = 5$. Since the swarm approach produces completely independent microstates, for a direct comparison we should consider a SLR from which only completely indepen-

dent microstates have been harvested. Hence, for comparing the two approaches, we choose $n = 5$. As shown above, a practical value for both K and M is 1000. With these choices, the swarm approach is faster than a SLR by a factor of $f_{\text{speedup}} = 385$, in exchange for a total computational cost that increases by a factor of $f_{\text{cost}} = 2.6$.

The above estimates for f_{speedup} and f_{cost} are approximate, and can be expected to vary substantially for different systems, different parameter choices (such as for n), and as the strategy for implementing a swarm approach is varied to best suit a particular physical system and/or computing facility. Although our results are thus difficult to generalize, they do show for a few practical, real-world cases that a swarm relaxation strategy can shorten the time to obtain results by a factor of several hundred, in return for an increased computational cost of about a factor of 3.

3.6 Discussion

In addition to a dramatic decrease in the time required to obtain results, another significant advantage of the swarm relaxation approach is the quality of the results, including their error estimates, and the ease with which they are evaluated. All the microstates that contribute to the final results in a swarm approach are, by construction, completely independent. The quality of the estimates for equilibrium properties is thus very high, since they are formed as pure ensemble averages. While we have focussed here on bulk average properties such as ρ and U, all observables available from a SLR can be readily computed from a swarm ensemble, including structural measures such as radial distribution functions, and quantities such as the specific heat that are based on fluctuations occurring within the ensemble. Also, since there is no need to estimate the time separation between independent microstates, as in a SLR, the evaluation of statistical error is straightforward and robust. A swarm approach

is therefore a good choice for studies requiring high-precision results, with rigorously defined error.

We emphasize that the swarm relaxation strategy does not resolve the fundamental physical challenges associated with the equilibration of complex systems. Users of the present approach must still be watchful for the effects of metastable states, and of slowly relaxing collective degrees of freedom. The approach does provide opportunities for checking for these effects, for example, testing for the presence of distinct metastable states by looking for divergent behavior in subsets of the swarm trajectories. If the presence of a slow degree of freedom is suspected, it would be best to check swarm results against a test case using a SLR, especially if the system under study is new.

Regarding the definition of the autocorrelation functions used here, there are of course other choices that may serve just as well, or even better, for assessing the relaxation of the system to equilibrium. In particular, the time decay of the intermediate scattering function has long been used as a benchmark for quantifying relaxation in bulk liquids and glasses [2]. When available, such additional measures of decorrelation can be used in a swarm approach to check for subtle, slowly relaxing degrees of freedom. Here, we have focussed on the autocorrelation functions obtained from the time series for the same observables (e.g. ρ and U) used to compare the swarm results to a SLR. We do so for simplicity, and to show that when M is large enough, any observable can be used to monitor the time evolution of τ as the system approaches equilibrium.

We have shown that $M = 10^3$ is sufficient to make our strategy both efficient and straightforward to implement. Smaller values of M may also be used, at the cost of decreased precision in the estimates for equilibrium properties and for characteristic time scales such as τ. In particular, if the behavior of τ as a function of t [see

Fig. 3.6(a)] is too noisy, then reliable estimates for $t_{\rm stop}$ become difficult to obtain. Tests using sub-ensembles of our swarm runs suggest that $M = 250$ is an approximate lower bound for obtaining accurate equilibrium properties, while simultaneously ensuring that a useful estimate for $t_{\rm stop}$ can be made from the behavior of $\tau(t)$.

In situations where $M \sim 10^3$ computing processors are not available for concurrent use, the swarm strategy can still be implemented, since the individual runs are independent and can run asynchronously. Furthermore, the computational workload in a swarm approach takes the form of a large number of short runs. Our experience when running asynchronously on a shared facility is that excellent throughput is achieved, since the runs fill usage gaps between larger and longer computing jobs.

We also note that the swarm approach can be modified by extending each run so as to produce a sequence of independent configurations, appropriately separated in time. In this case, observables are evaluated from a combination of ensemble and time averaging. The balance between the two kinds of averaging can be tuned to best fit the available computing resources, bearing in mind that such a hybrid approach does not minimize the wall-clock time, and complicates the error analysis, relative to a pure swarm strategy.

Finally, we point out the conceptual connections between our work and studies of physical aging in glassy systems. The swarm procedure used here is the same as that commonly used in simulations to study the aging of material properties in a glass subjected (e.g.) to a jump in T. The only difference is that here the destination equilibrium state can be reached, and that the characteristic time scales are much shorter than those normally studied in aging. In particular, we draw the reader's attention to Dyre's recent analysis of the Narayanaswamy theory for physical aging, in which the "material time" is unambiguously related to the system's mean-square-displacement in configuration space [25]. The variation of τ with t shown in Fig. 3.6 is

a proxy measure of the material time in our test systems as they approach equilibrium. It would be interesting for future work to assess the swarm relaxation strategy within the framework of Dyre's analysis.

To summarize, the practicality of the swarm relaxation strategy rests on two observations: (i) The time required to generate independent microstates during a single long run is comparable to the time required to bring a single short run into equilibrium. (ii) When the swarm is large enough, the attainment of equilibrium can be confirmed within a time that is not much longer than the equilibration process itself. So long as these two observations hold, the present strategy is an effective way to "trade processors for time". When computational facilities having 10^3 or more processors are available, and when time is of the essense, the swarm relaxation strategy is an effective way to rapidly generate high-quality results with robustly defined statistical error.

3.7 Acknowledgements

RKB, ISV and PHP thank NSERC for support. Computational resources were provided by ACEnet.

3.8 Author Contributions

All authors contributed to the development of this study and the interpretation of the results. FS provided the Monte Carlo code for the bulk liquid ST2 simulations, which were carried out by PHP. SMAM carried out the TIP4P/2005 nanodroplet simulations. PHP drafted the manuscript, with input from all authors.

Bibliography

[1] D. Frenkel and B. Smit, *Understanding Molecular Simulations: from Algorithms to Applications*, 2nd ed., Academic Press, San Diego (2002).

[2] L. Berthier and G. Biroli, Rev. Mod. Phys. **83**, 587 (2011).

[3] L.S.D. Caves, J.D. Evanseck and M. Karplus, Protein Sci. **7**, 649 (1998).

[4] A. Elofsson and L. Nilsson, J. Mol. Biol. **233**, 766 (1993).

[5] P.V. Coveney and S. Wan, Phys. Chem. Chem. Phys. **18**, 30236 (2016).

[6] A.P. Bhati, S. Wan, D.W. Wright and P.V. Coveney, J. Chem. Theory Comput. **13**, 210 (2017).

[7] W. Kob and J.-L. Barrat, Phys. Rev. Lett. **78**, 4581 (1997).

[8] E. La Nave, S. Sastry and F. Sciortino, Phys. Rev. E **74**, 050501, (2006).

[9] F.H. Stillinger and A. Rahman, J. Chem. Phys. **60**, 1545 (1974).

[10] O. Steinhauser, Mol. Phys. **45**, 335 (1982).

[11] P.H. Poole, F. Sciortino, U. Essmann and H.E. Stanley, Nature **360**, 324 (1992).

[12] P.H. Poole, I. Saika-Voivod and F. Sciortino, J. Phys.: Condens. Matter **17**, L431 (2005).

[13] P.H. Poole, S. R. Becker, F. Sciortino and F.W. Starr, J. Phys. Chem. B **115**, 14176 (2011).

[14] V. Holten, J.C. Palmer, P.H. Poole, P.G. Debenedetti and M.A. Anisimov, J. Chem. Phys. **140**, 104502 (2014).

[15] J.C. Palmer, F. Martelli, Y. Liu, R. Car, A.Z. Panagiotopoulos and P.G. Debenedetti, Nature **510**, 385 (2014).

[16] S.K. Morris, O. Zavalov, R.K. Bowles, I. Saika-Voivod, F. Sciortino and P.H. Poole, preprint (2017).

[17] A.J. Kovacs, Fortschr. Hochpolym. Forsch. **3**, 394 (1963).

[18] S. Mossa and F. Sciortino, Phys. Rev. Lett. **92**, 045504 (2004).

[19] J.L.F. Abascal and C. Vega, J. Chem. Phys. **123**, 234505 (2005).

[20] S.M.A. Malek, P.H. Poole and I. Saika-Voivod, preprint (2017).

[21] S. Nose, Mol. Phys. **52**, 255 (1984).

[22] W.G. Hoover, Phys. Rev. A **31**, 1695 (1985).

[23] A. Widmer-Cooper and P. Harrowell, J. Chem. Phys. **126**, 154503 (2007).

[24] P.H. Poole, R.K. Bowles, I. Saika-Voivod and F. Sciortino, J. Chem. Phys. **138**, 034505 (2013).

[25] J.C. Dyre, J. Chem. Phys. **143**, 114507 (2015).

3.9 Appendix: Fluctuations of the autocorrelation function

Here we show that the fluctuations of the autocorrelation function $C_x(t_0, t)$ have a standard deviation $\sigma_C = M^{-1/2}$, when C_x approaches zero.

Let $X(t)$ represent the discrete set of M random variables $\{x(i,t)\}$ for various i at fixed t. Similarly, let $\delta X(t)$ represent the discrete set of M random variables $\{x(i,t) - \langle x(t)\rangle\}$. The variance of $X(t)$ can be written in a number of ways:

$$\begin{aligned} \mathrm{Var}[X(t)] &= \sigma^2(t) \\ &= \left\langle \Big[x(i,t) - \big\langle x(t) \big\rangle \Big]^2 \right\rangle \\ &= \left\langle \Big[\delta X(t) \Big]^2 \right\rangle \\ &= \left\langle \Big[X(t) \Big]^2 \right\rangle - \big\langle X(t) \big\rangle^2 . \end{aligned} \tag{3.4}$$

In this notation,

$$C_x(t_0, t) = \frac{\big\langle \delta X(t_0)\ \delta X(t) \big\rangle}{\sigma(t_0)\,\sigma(t)} . \tag{3.5}$$

The fluctuations of C_x are quantified by $\mathrm{Var}[C_x(t_0,t)] = \sigma_C^2$. Using standard identities for the variance, we have,

$$\begin{aligned} \mathrm{Var}[C_x(t_0,t)] &= \mathrm{Var}\left[\frac{\big\langle \delta X(t_0)\ \delta X(t) \big\rangle}{\sigma(t_0)\,\sigma(t)} \right] \\ &= \frac{\mathrm{Var}\Big[\big\langle \delta X(t_0)\ \delta X(t) \big\rangle \Big]}{\sigma^2(t_0)\,\sigma^2(t)} \\ &= \frac{\mathrm{Var}\Big[\delta X(t_0)\ \delta X(t) \Big]}{M\,\sigma^2(t_0)\,\sigma^2(t)} . \end{aligned} \tag{3.6}$$

Using the last equality of Eq. 3.4 we can write,

$$\begin{aligned} \mathrm{Var}\Big[\delta X(t_0)\ \delta X(t)\Big] &= \Big\langle \Big[\delta X(t_0)\Big]^2 \Big[\delta X(t)\Big]^2 \Big\rangle \\ &\quad -\Big\langle \delta X(t_0)\ \delta X(t) \Big\rangle^2 \end{aligned} \tag{3.7}$$

For sufficiently large Δt, $\delta X(t_0)$ and $\delta X(t)$ become independent, and $C_x \to 0$. In this case, the first term on the right-hand side of Eq. 3.7 reduces to,

$$\begin{aligned} \Big\langle \Big[\delta X(t_0)\Big]^2 \Big[\delta X(t)\Big]^2 \Big\rangle &= \Big\langle \Big[\delta X(t_0)\Big]^2 \Big\rangle \Big\langle \Big[\delta X(t)\Big]^2 \Big\rangle \\ &= \sigma^2(t_0)\, \sigma^2(t), \end{aligned} \tag{3.8}$$

and the second term vanishes,

$$\Big\langle \delta X(t_0)\ \delta X(t) \Big\rangle^2 = \Big\langle \delta X(t_0) \Big\rangle^2 \Big\langle \delta X(t) \Big\rangle^2 = 0, \tag{3.9}$$

because by definition $\langle \delta X(t_0) \rangle = \langle \delta X(t) \rangle = 0$. Combining Eqs. 3.6-3.9, we obtain,

$$\mathrm{Var}[C_x(t_0, t)] = M^{-1}. \tag{3.10}$$

Therefore, the standard deviation σ_C of fluctuations of C_x as $C_x \to 0$ is,

$$\sigma_C = M^{-1/2}. \tag{3.11}$$

Chapter 4

Evaluating the Laplace pressure of water nanodroplets from simulations

4.1 Abstract

We calculate the components of the microscopic pressure tensor as a function of radial distance r from the centre of a spherical water droplet, modelled using the TIP4P/2005 potential. To do so, we modify a coarse-graining method for calculating the microscopic pressure [T. Ikeshoji, B. Hafskjold, and H. Furuholt, Mol. Simul. **29**, 101 (2003)] in order to apply it to a rigid molecular model of water. As test cases, we study nanodroplets ranging in size from 776 to 2880 molecules at 220 K. Beneath

a surface region comprising approximately two molecular layers, the pressure tensor becomes approximately isotropic and constant with r. We find that the dependence of the pressure on droplet radius is the one expected from the Young-Laplace equation, despite the small size of the droplets.

4.2 Introduction

Small droplets of liquid water are important to atmospheric science and technological applications, and understanding the properties and role of the surface is increasingly important as droplets become nanoscopic. Surface effects can profoundly influence the mechanism and rate of crystallization in general. In water, the role of surface freezing is still unresolved [1].

Significant to much of the discussion is the Laplace pressure, the pressure difference between the interior and exterior of a droplet of radius R arising from the liquid-vapour surface tension γ, as quantified by the Young-Laplace equation for droplets,

$$\Delta P = \frac{2\gamma}{R}. \tag{4.1}$$

Galli and coworkers modelled the effect within nanodroplets of the Laplace pressure on nucleation rates [2]. They argued that since the interior of the nanodroplet is at a higher pressure, the liquid there is less supercooled on account of the decreasing melting temperature of ice Ih with increasing pressure. Hence nucleation rates should be greatly diminished in the interior. Espinosa et al [3] went on to show that the liquid-Ih surface tension also increases with increasing pressure, further suppressing nucleation. By contrast, the nanodroplet surface, though prone to disorder, experiences a negative pressure, and should thus be more supercooled and therefore enhance nucleation rates. The simulations of Ref. [2] showed that nucleation rates for mW [4] water nan-

odroplets are progressively and greatly suppressed as nanodroplet size decreases, and that the rates are the same within error for $R \geq 3.1$ nm when compared to the bulk at the same density. For smaller nanodroplets, the difference in rates between droplets and bulk at the same density is significant. The authors argue, however, that for real water, for which the density difference between liquid and crystal at melting is larger than in mW water, surface nucleation should be favoured in microdroplets. We note that while the authors estimated the Laplace pressure through Eq. 4.1 and provided a check of the equation by determining the pressure of the bulk at the same density as inside the nanodroplets, they did not explicitly calculate the pressure inside the droplets. Nor is it clear to what extent Eq. 4.1 should hold for more realistic models of water, such as the TIP4P model [5] and related potentials [6].

The insights of Ref. [2] have been enriched by the work of Haji-Akbari and Debenedetti [7] on water nanofilms. They found that nucleation rates obtained using the TIP4P/ice [8] model of water are enhanced by a factor of 10^7 within the nanofilm in comparison to the bulk. The enhancement stems not from the interface, where crystal-like ordering is reduced, but rather from a relative abundance of "double-diamond cages" over hexagonal cages in the interior of the film compared to bulk. The latter cage type is less favourable for nucleation. Their work therefore indicates the importance of subtle changes in structure arising from the finite extent of the system, and diminishes the importance of the negative pressure near the interface. However, this study was conducted on films, where the internal pressure is no different from the ambient, and therefore did not address the role of the Laplace pressure on the interior.

Recent experiments on microdroplets, for which the Laplace pressure is likely negligible, have pushed the limits of observing liquid water below the bulk homogeneous nucleation limit of 235 K by determining nucleation rates down to 227 K [9].

Nucleation rates at significantly lower temperatures have been measured for nanodroplets with radii of just a few nanometers [10, 11], for which the Laplace pressure is likely significant. An experimental study of water clusters in the range of 100-1000 molecules showed that crystallization may be entirely suppressed below roughly 275 molecules [12], at which point surface effects may dominate and the Laplace pressure would be quite high. Given that experiments probe ever smaller systems, it is crucial to develop a better understanding of the basic physical properties of nanodroplets, including the pressure.

The theoretical and experimental developments described above all point to the need for a detailed analysis of the microscopic pressure tensor within water nanodroplets and its connection to the Laplace pressure. This is the subject of this paper. The work on ST2 water clusters of Brodskaya et al. [13, 14] found significantly elevated pressures within nanodroplet interiors. Thompson et al. [15] provided a detailed description of the methodology for calculating the pressure tensor in droplets in the context of Lennard-Jones particles. We base our calculations on the work by Ikeshoji et al. [16], who developed a coarse-grained scheme for calculating the molecular-scale pressure for simple particles interacting with radial potentials. The advantages of their method include improved statistics over non-coarse-grained methods (e.g. [15]), as well as the ability to directly calculate both the normal and transverse components of the pressure tensor. The method was applied to a molecular model of water, SPC/E [17], in a study of methane hydrate droplets embedded in ice [18], but no details on how the method was modified for molecules were given. The method of Ref. [16] was later generalized to molecules in a way that considered multibody intramolecular interactions, and applied to non-rigid chain-like organic molecules interacting with a coarse grained-model for water [19]. However, for rigid multi-site water models such as TIP4P/2005, it is more straightforward to modify Ref. [16] in a way that does not

require the consideration of intramolecular interactions, i.e., forces of constraint. It is this latter approach that we present here. That is, we adapt the method of Ref. [16] to TIP4P/2005 water nanodroplets, and give details of the calculation.

This paper is organized as follows. Section 4.3 describes our molecular dynamics simulations of TIP4P/2005 water nanodroplets. In Section 4.4 we show in detail how we adapt and apply the method introduced in Ref. [16] to water, comment on the utility of the method in terms of independently calculating the normal and transverse components of the local pressure tensor, and introduce an energy-based approximate method of calculating the local isotropic pressure and use it as a check of our results. We present the pressure components as functions of radial distance from the centre of mass of a nanodroplet and validate the form of Eq. 4.1 in Section 4.5, before concluding in Section 4.6.

4.3 Simulations

We simulate nanodroplets of $N = 776$, 1100, 1440 and 2880 water molecules interacting through the TIP4P/2005 water model [20]. All simulations are done at temperature $T = 220$ K, where the vapour pressure is negligible. For $N = 1440$ and 2880, we initially prepare a droplet system of a given size by placing N water molecules randomly in a rather large cubic simulation box and simulating at constant volume. The molecules naturally condense into a droplet surrounded by a very low density vapour. The equilibrated configuration is then run for many relaxation times to get equilibrium properties of the droplets. We produce two spherical droplets of size $N = 776$ and 1100 by removing molecules beyond an appropriate radial distance from the centre of an equilibrated $N = 1440$ droplet. For the $N = 776$ system, the simulation box length $L = 15$ nm. For the larger droplets $L = 20$ nm. We use a potential cutoff

of $L/2$, and employ periodic boundary conditions to ensure that vapour molecules can return to the droplet in order to avoid eventual evaporation. The box is large enough to avoid any direct interaction between the water droplet and its periodic images. With this setup, molecules within the droplet interact through the full, untruncated potential, including electrostatic interactions. We use Gromacs v4.6.1 [20] to carry out the molecular dynamics simulations. We hold T constant with the Nosé-Hoover thermostat. The equations of motion are integrated with the leap-frog algorithm with a time step of 2 fs. The total simulation times for the four droplet sizes, in order of increasing N, are 862, 633, 593 and 182 ns.

To determine equilibration and relaxation times, we monitor the decay of the bond autocorrelation function $\phi(t)$, which gives the probability that a bond present at time $t = 0$ remains unbroken until time t [22]. Two molecules i and j are considered bonded if the distance between their O atoms is less than 0.32 nm, the location of the first minimum in the oxygen-oxygen radial distribution function of bulk water at ambient conditions. The calculation of $\phi(t)$ is sensitive to the sampling interval, which in our case falls between 0.2 and 0.8 ns. We can not discriminate between persistent and reformed bonds on times shorter than our sampling time, and so our $\phi(t)$ provides an upper bound on the true value.

Error bars for various quantities are calculated by taking the standard deviation in a quantity over all sampled equilibrium configurations, and dividing by $\sqrt{n_{\mathrm{ind}}}$, where $n_{\mathrm{ind}} = t_{\mathrm{eq}}/\tau_\phi$ is the estimated number of independent configurations sampled, t_{eq} is the duration of the equilibrated time series used for averaging, and τ_ϕ is the time at which $\phi(t) \leq e^{-1} \approx 0.368$. For example, for the $N = 1100$ droplet, the simulation is carried out for a total of 633 ns, the first 129 ns of which are discarded, leaving $t_{\mathrm{eq}} = 504$ ns. Our determination of $\phi(t)$ is not very well resolved in time, but we determine that $\phi(0.8\text{ ns}) = 0.08$ and so we set $\tau_\phi = 0.8$ ns and hence $n_{\mathrm{ind}} \approx 500/0.8 = 625$. Our

estimates for the number of independent configurations sampled in equilibrium for the other sizes are 1917 ($N = 776$), 1588 ($N = 1440$) and 48 ($N = 2880$).

4.4 Microscopic pressure

4.4.1 Pressure profiles

To calculate the normal $P_N(r)$ and tangential $P_T(r)$ components of the pressure tensor as a function of radial distance r from the centre of mass of the water nanodroplet, we follow the prescription of Ikeshoji *et al.* [16] for a spherical geometry. Below we reproduce their approach, which uses a coarse graining wherein the pressure components at r are calculated as averages over a thin spherical shell of finite thickness in order to improve statistics and to avoid divergences in $P_T(r)$.

Their method was presented for particles interacting through central forces. We introduce adaptations required since the pair force between water molecules is not central (although the site-site interactions are). The generalization is straightforward since only the intermolecular forces need to be considered and they need not be central [13, 14, 23]. In order to present the reader with a self-contained explanation of the method, we have reproduced relevant portions of Ref. [16] here. To be more explicit, Eqs. 4.2 to 4.14 and their development are adapted from Ref. [16], albeit with slightly different notation, while Eqs. 4.15 to 4.24 have been modified because of the non-central force between molecules. Fig. 4.1 is adapted from [16] to explicitly include all types of molecular pair contributions. We introduce Table 4.1 to provide mathematical details that complement Fig. 4.1.

Schofield and Henderson [24] showed that the pressure tensor at a point $\mathbf{R}$ in

space is given by [24, 15],

$$P'_{\alpha\beta}(\mathbf{R}) = \left\langle P'_{c,\alpha\beta}(\mathbf{R}) \right\rangle + \left\langle P'_{k,\alpha\beta}(\mathbf{R}) \right\rangle, \tag{4.2}$$

where

$$\left\langle P'_{k,\alpha\beta}(\mathbf{R}) \right\rangle = k_B T \rho(\mathbf{R}) \delta_{\alpha\beta}, \tag{4.3}$$

is the kinetic part, and follows directly from the local equilibrium density $\rho(\mathbf{R})$. The brackets $\langle \dots \rangle$ indicate an ensemble average, i.e., an average over a set of equilibrated configurations, and $\delta_{\alpha\beta}$ is the Kronecker delta. Pressures annotated with a prime indicate that the pressure is calculated at a single point in space. Pressures without primes refer to quantities that are coarse-grained (averaged) over a small volume.

The configurational contribution is obtained from intermolecular pair forces, and is given by,

$$P'_{c,\alpha\beta}(\mathbf{R}) = \frac{1}{2} \sum_i \sum_{j \neq i} P'_{ij,\alpha\beta}(\mathbf{R}), \tag{4.4}$$

where the molecular pair-wise contribution to the pressure is given by,

$$P'_{ij,\alpha\beta}(\mathbf{R}) = \int_{C_{ij}} f_{ij,\alpha}\, \delta(\mathbf{R} - \mathbf{l}\,) dl_\beta, \tag{4.5}$$

where $f_{ij,\alpha}$ is the α component of the force on molecule j due to molecule i, $\mathbf{f}_{ij}$, $\delta(\mathbf{R}-\mathbf{l})$ is the Dirac delta function, C_{ij} is a contour from i to j, $\mathbf{l}$ is a vector indicating a point on C_{ij}, and dl_β is the β component of an infinitesimal portion of the path along C_{ij}. We stress that $\mathbf{f}_{ij}$ is the force between two molecules, i.e., the quantity that is responsible for the acceleration of the centres of mass of the molecules. We consider neither torques nor forces between atoms on the same molecule nor forces of contstraint [23]. For TIP4P/2005, $\mathbf{f}_{ij}$ is obtained by summing over all of the interactions between charge and Lennard-Jones sites on molecule i and those on molecule j. The freedom

in choosing C_{ij} renders the definition of the microscopic pressure non-unique. Ikeshoji et al [16] follows the convention of defining C_{ij} to be a straight line segment connecting the centres of mass of molecules i and j, consistent with the Irving-Kirkwood definition of the pressure tensor [25]. As we comment below, this simple and intuitive choice of C_{ij} leads to divergences in $P_T(r)$ that coarse-graining eliminates.

The coarse-graining procedure amounts to carrying out an integration of Eq. 4.2 over $\mathbf{R}$ within a spherical shell of radius r, thickness Δr and volume $\tilde{V} = 4\pi[R_{\rm out}^3 - R_{\rm in}^3]/3$, with $R_{\rm out} = r + \Delta r/2$ and $R_{\rm in} = r - \Delta r/2$. We set $\Delta r = 0.05$ nm. The coarse-grained pressure $P_{\alpha\beta}(r)$ is given by,

$$P_{\alpha\beta}(r) = \frac{1}{\tilde{V}} \int_{\tilde{V}} P'_{\alpha\beta}(\mathbf{R}) d\mathbf{R} = \langle P_{c,\alpha\beta} \rangle + \langle P_{k,\alpha\beta} \rangle \,. \tag{4.6}$$

The kinetic part is still calculated from the density, but now averaged over $\tilde{V}$. The configurational part maintains the same form as before,

$$P_{c,\alpha\beta} \;=\; \frac{1}{2} \sum_i \sum_{j \neq i} P_{ij,\alpha\beta}, \tag{4.7}$$

but now the coarse-grained contribution to the pressure from an interaction between a pair of molecules is given by,

$$\begin{aligned} P_{ij,\alpha\beta} &= \frac{1}{\tilde{V}} \int_{\tilde{V}} \int_{C_{ij}} f_{ij,\alpha}\, \delta(\mathbf{R} - \mathbf{l}) dl_\beta d\mathbf{R}, \\ &= \frac{1}{\tilde{V}} \int_{C_{ij}} f_{ij,\alpha} \left[\int_{\tilde{V}} \delta(\mathbf{R} - \mathbf{l}) d\mathbf{R} \right] dl_\beta, \\ &= \frac{1}{\tilde{V}} \int_{C_{ij} \in \tilde{V}} f_{ij,\alpha} dl_\beta, \end{aligned} \tag{4.8}$$

where the force between molecules i and j contributes to the pressure in $\tilde{V}$ only along the parts of C_{ij} that are in $\tilde{V}$. Regardless of the location of i and j, i.e., whether they

are in $\tilde{V}$ or not, as long as the line between them passes through $\tilde{V}$, their interaction contributes to the pressure.

To determine the part of C_{ij} that contributes to the pressure in $\tilde{V}$, one first uses a parametric expression for $\mathbf{l}(\lambda)$ that defines points located on C_{ij},

$$\mathbf{l}(\lambda) = \mathbf{r}_i + \lambda \mathbf{r}_{ij}, \tag{4.9}$$

where $\mathbf{r}_{ij} = \mathbf{r}_j - \mathbf{r}_i$, i.e. the vector pointing from i to j. (For repulsion, $\mathbf{f}_{ij}$ points approximately along $\mathbf{r}_{ij}$.) Points on $C_{\rm ij}$ correspond to $\lambda \in [0, 1]$.

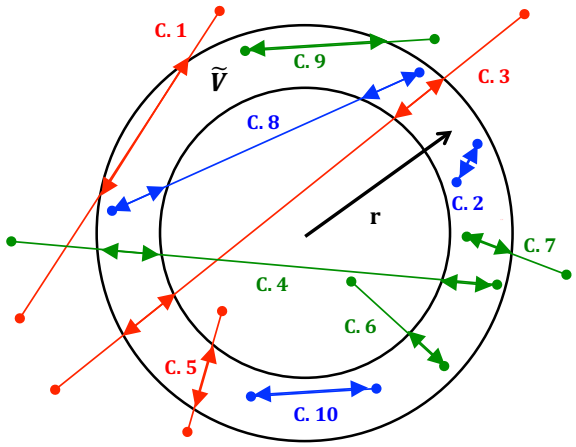

Figure 4.1: A sketch of all possible contributions to P in $\tilde{V}$ from the coarse-graining method of Ikeshoji *et al.* [16]. See Table 4.1 for details. The contours C_{ij} are line segments between molecules i and j (filled circles). The portions of C_{ij} between arrows contribute to the pressure. $\tilde{V}$ is a spherical shell of inner radius $R_{\rm in} = r - \Delta R/2$ and outer radius $R_{\rm out} = r + \Delta R/2$.

Fig. 4.1 shows a sketch of all possible contributions from molecular pair interactions to $\tilde{V}$ in the coarse-grained method. The contributions from C_{ij} that contribute to the pressure in $\tilde{V}$ are portions of lines between arrows, while the line between small filled circles is the line segment connecting particles i and j. For a given line, the portion between arrows corresponds to $\lambda_a \leq \lambda \leq \lambda_b$, with a and b labelling entry and exit points. If the line intersects $\tilde{V}$ over two segments (yielding two contributions

to the pressure), there is a second set of entry and exit points that define the segment $\lambda'_a \leq \lambda \leq \lambda'_b$. If $\mathbf{r}_i \in \tilde{V}$ then $\lambda_a = 0$, while if $\mathbf{r}_j \in \tilde{V}$ then λ_b (or λ'_b if it exists) $= 1$.

A precise determination of relevant intersections between the line $\mathbf{l}(\lambda)$ and the spheres bounding $\tilde{V}$ requires solving the equation,

$$\mathbf{l}(\lambda) \cdot \mathbf{l}(\lambda) \;\; = \;\; r_i^2 + \lambda\, 2\mathbf{r}_i \cdot \mathbf{r}_{ij} + \lambda^2 r_{ij}^2 = R_{\text{out}}^2, \tag{4.10}$$

and a similar one for R_{in}. The magnitudes of $\mathbf{r}_i$ and $\mathbf{r}_{ij}$ are r_i and r_{ij}, respectively. The solutions to these quadratic equations are,

$$\lambda_{\pm}^{\text{in/out}} = -\frac{\mathbf{r}_i \cdot \mathbf{r}_{ij}}{r_{ij}^2} \pm \frac{1}{r_{ij}^2}\sqrt{D_{\text{in/out}}}, \tag{4.11}$$

where the discriminants are given by,

$$D_{\text{in/out}} = (\mathbf{r}_i \cdot \mathbf{r}_{ij})^2 - r_{ij}^2 \left(r_i^2 - R_{\text{in/out}}^2\right). \tag{4.12}$$

If $D_{\text{out}} < 0$, there are no intersections and the pair interaction gives no contribution to the pressure in $\tilde{V}$. All of the possible cases for solution sets yielding pressure contributions and the resulting limits of integration are given in Table 4.1.

Having determined all intersections and limits on our integration variable λ, Eq. 4.8 becomes,

$$\begin{aligned} P_{ij,\alpha\beta} = \frac{1}{\tilde{V}} \Bigg[& \int_{\lambda_a}^{\lambda_b} (\mathbf{f}_{ij} \cdot \mathbf{e}_\alpha)(\mathbf{r}_{ij} \cdot \mathbf{e}_\beta) d\lambda \\ & + \int_{\lambda'_a}^{\lambda'_b} (\mathbf{f}_{ij} \cdot \mathbf{e}_\alpha)(\mathbf{r}_{ij} \cdot \mathbf{e}_\beta) d\lambda \Bigg], \end{aligned} \tag{4.13}$$

where the integrand is expressed in terms of the unit vectors $\mathbf{e}_r$, $\mathbf{e}_\theta$, and $\mathbf{e}_\phi$. Note that if there is only one portion of C_{ij} intersecting $\tilde{V}$, then the second integral in Eq. 4.13

$D_{\rm in}$	$\lambda_-^{\rm in}$	$\lambda_+^{\rm in}$	$\lambda_-^{\rm out}$	$\lambda_+^{\rm out}$	λ_a	λ_b	λ'_a	λ'_b	Case
<0			[0,1]	[0,1]	$\lambda_-^{\rm out}$	$\lambda_+^{\rm out}$			C.1
>0	<0	<0	<0	>1	0	1			C.2
>0	>1	>1	<0	>1	0	1			C.2
>0	[0,1]	[0,1]	[0,1]	[0,1]	$\lambda_-^{\rm out}$	$\lambda_-^{\rm in}$	$\lambda_+^{\rm in}$	$\lambda_+^{\rm out}$	C.3
>0	[0,1]	[0,1]	<0	[0,1]	0	$\lambda_-^{\rm in}$	$\lambda_+^{\rm in}$	$\lambda_+^{\rm out}$	C.4
>0	[0,1]	[0,1]	[0,1]	>1	$\lambda_-^{\rm out}$	$\lambda_-^{\rm in}$	$\lambda_+^{\rm in}$	1	C.4
>0	<0	[0,1]	<0	[0,1]	$\lambda_+^{\rm in}$	$\lambda_+^{\rm out}$			C.5
>0	[0,1]	>1	[0,1]	>1	$\lambda_-^{\rm out}$	$\lambda_-^{\rm in}$			C.5
>0	<0	[0,1]	<0	>1	$\lambda_+^{\rm in}$	1			C.6
>0	[0,1]	>1	<0	>1	0	$\lambda_-^{\rm in}$			C.6
>0	<0	<0	<0	[0,1]	0	$\lambda_+^{\rm out}$			C.7
>0	>1	>1	[0,1]	>1	$\lambda_-^{\rm out}$	1			C.7
>0	[0,1]	[0,1]	<0	>1	0	$\lambda_-^{\rm in}$	$\lambda_+^{\rm in}$	1	C.8
<0			<0	[0,1]	0	$\lambda_+^{\rm out}$			C.9
<0			[0,1]	>1	$\lambda_-^{\rm out}$	1			C.9
<0			<0	>1	0	1			C.10

Table 4.1: List of all 16 solution sets of Eq. 4.11 that contribute to Eq. 4.13 and the resulting limits of integration. In all cases $D_{\rm out} > 0$. Entries in the rightmost column refer to curve labels in Fig. 4.1.

(with limits λ'_a and λ'_b) is absent. These unit vectors are not constant as $\mathbf{l}(\lambda)$ moves along C_{ij}, and the unit vectors in Cartesian coordinates are,

$$\begin{aligned}
\mathbf{e}_r &= \left\{ \frac{l_x}{l}, \frac{l_y}{l}, \frac{l_z}{l} \right\}, \\
\mathbf{e}_\theta &= \left\{ \frac{l_x l_z}{l(l_x^2+l_y^2)^{1/2}}, \frac{l_y l_z}{l(l_x^2+l_y^2)^{1/2}}, \frac{-(l_x^2+l_y^2)^{1/2}}{l} \right\}, \\
\mathbf{e}_\phi &= \left\{ \frac{-l_y}{(l_x^2+l_y^2)^{1/2}}, \frac{l_x}{(l_x^2+l_y^2)^{1/2}}, 0 \right\},
\end{aligned} \tag{4.14}$$

where ϕ is the azimuth angle in the xy-plane, θ is the angle between $\mathbf{l}$ and the z-axis, $l = |\,\mathbf{l}\,|$, and l_α is the α component of $\mathbf{l}$.

The P_{ij} tensor can be written in terms of two components, normal and tangential. These components are obtained from Eq. 4.13 using Eqs. 4.9 and 4.14. The contribution from the interaction between molecules i and j to the normal component is

given by,

$$P_{ij,N} \equiv P_{ij,rr} = \frac{1}{\tilde{V}} \int_{\lambda_a}^{\lambda_b} (\mathbf{f}_{ij} \cdot \mathbf{e}_r)(\mathbf{r}_{ij} \cdot \mathbf{e}_r) d\lambda \tag{4.15}$$

$$= \frac{1}{\tilde{V}} \int_{\lambda_a}^{\lambda_b} \frac{a_n + b_n\lambda + c_n\lambda^2}{d_n + e_n\lambda + f_n\lambda^2} d\lambda \tag{4.16}$$

$$= \frac{1}{\tilde{V}} \left\{ \Sigma_N(\lambda) \Big|_{\lambda_a}^{\lambda_b} + \Sigma_N(\lambda) \Big|_{\lambda'_a}^{\lambda'_b} \right\}, \tag{4.17}$$

where we omit in Eqs. 4.15 and 4.16 the second integral simply for brevity, and,

$$a_n = (\mathbf{r}_i \cdot \mathbf{f}_{ij})\,(\mathbf{r}_i \cdot \mathbf{r}_{ij}) \tag{4.18}$$

$$b_n = (\mathbf{r}_{ij} \cdot \mathbf{f}_{ij})\,(\mathbf{r}_i \cdot \mathbf{r}_{ij}) + (\mathbf{r}_i \cdot \mathbf{f}_{ij})\,(\mathbf{r}_{ij} \cdot \mathbf{r}_{ij})$$

$$c_n = (\mathbf{r}_{ij} \cdot \mathbf{f}_{ij})\,(\mathbf{r}_{ij} \cdot \mathbf{r}_{ij})$$

$$d_n = \mathbf{r}_i \cdot \mathbf{r}_i$$

$$e_n = 2\,\mathbf{r}_i \cdot \mathbf{r}_{ij}$$

$$f_n = \mathbf{r}_{ij} \cdot \mathbf{r}_{ij}$$

$$\begin{aligned} \Sigma_N(\lambda) &= \frac{1}{2f_n^2} \{2c_n f_n \lambda + (b_n f_n - c_n e_n) \\ &\times \ln\left[d_n + e_n\lambda + f_n\lambda^2\right] \\ &+ \frac{2}{\sqrt{4d_n f_n - e_n^2}} \arctan\left[\frac{e_n + 2f_n\lambda}{\sqrt{4d_n f_n - e_n^2}}\right] \\ &\times \left(f_n(2a_n f_n - b_n e_n) + c_n(e_n^2 - 2d_n f_n)\right)\Big\}, \end{aligned} \tag{4.19}$$

while the tangential component is given by,

$$P_{ij,T} \equiv P_{ij,\phi\phi} = \frac{1}{\tilde{V}} \int_{\lambda_a}^{\lambda_b} (\mathbf{f}_{ij} \cdot \mathbf{e}_\phi)(\mathbf{r}_{ij} \cdot \mathbf{e}_\phi) d\lambda \tag{4.20}$$

$$= \frac{c_t}{\tilde{V}} \int_{\lambda_a}^{\lambda_b} \frac{a_t + b_t\lambda}{d_t + e_t\lambda + f_t\lambda^2} d\lambda \tag{4.21}$$

$$= \frac{c_t}{\tilde{V}} \left\{ \Sigma_T(\lambda) \Big|_{\lambda_a}^{\lambda_b} + \Sigma_T(\lambda) \Big|_{\lambda'_a}^{\lambda'_b} \right\}, \tag{4.22}$$

where we omit in Eqs. 4.20 and 4.21 the second integral for brevity, and,

$$
\begin{aligned}
a_t &= r_{i,x}\, f_{ij,y} - r_{i,y}\, f_{ij,x} && (4.23)\\
b_t &= r_{ij,x}\, f_{ij,y} - r_{ij,y}\, f_{ij,x} \\
c_t &= r_{i,x}\, r_{ij,y} - r_{i,y}\, r_{ij,x} \\
d_t &= r_{i,x}^2 + r_{i,y}^2 \\
e_t &= 2\,\left(r_{i,x}\, r_{ij,x} + r_{i,y}\, r_{ij,y}\right) \\
f_t &= r_{ij,x}^2 + r_{ij,y}^2 \\
\Sigma_T(\lambda) &= \frac{b_t \ln\left[d_t + e_t\lambda + f_t\lambda^2\right]}{2f_t} && (4.24)\\
&+ \arctan\left[\frac{e_t + 2f_t\lambda}{\sqrt{4d_tf_t - e_t^2}}\right]\frac{(2a_tf_t - b_te_t)}{f_t\sqrt{4d_tf_t - e_t^2}}
\end{aligned}
$$

Having assembled all the pieces required to calculate the coarse-grained pressure tensor components, we now report on the following radial quantities related to the pressure (see Eq. 4.6):

$$
\begin{aligned}
P_N(r) &= \langle P_{c,rr}\rangle + k_BT\rho(r) && (4.25)\\
\bar{P}_{c,N}(r) &= \langle P_{c,rr}\rangle && (4.26)\\
P_T(r) &= \langle P_{c,\phi\phi}\rangle + k_BT\rho(r) && (4.27)\\
\bar{P}_{c,T}(r) &= \langle P_{c,\phi\phi}\rangle && (4.28)\\
P(r) &\equiv \frac{1}{3}P_N(r) + \frac{2}{3}P_T(r) && (4.29)
\end{aligned}
$$

where $\rho(r)$ is the average number density of molecules in $\tilde{V}$ as determined from molecular centres of mass and $P(r)$, the mean (or isotropic) pressure, is one third the trace of the pressure tensor. As noted in Ref. [16], the tangential component may be calculated from $P_{ij,\theta\theta}$. However, the analytic expression for the resulting antiderivative

is very cumbersome.

4.4.2 Comment on calculating $P_T(r)$

Without coarse-graining, the transverse component of the pressure tensor is calculated from the first of two equivalent equations relating pressure components derived from the condition of mechanical stability [15, 16],

$$P_T(r) = P_N(r) + \frac{r}{2}\frac{dP_N(r)}{dr} \tag{4.30}$$

$$P_N(r) = \frac{2}{r^2}\int_0^r P_T(r')r'dr', \tag{4.31}$$

rather than directly from configurations on account of divergences occurring in Eq. 4.5. (We note that Eqs. 4.30 and 4.31 are valid regardless of whether the quantities are coarse-grained or not.) To illustrate this, let us use Eq. 4.5 in the context of calculating the transverse pressure component over a sphere (not a spherical shell) of radius r and assume for simplicity, for the purposes of this illustration only, that $\mathbf{f}_{ij} = f_{ij}\hat{r}_{ij}$, with f_{ij} a scalar and the unit vector is the one derived from $\mathbf{r}_{ij}$, i.e. that the force is central - acting along the line joing the particles. Our setup for this illustration is shown in Fig. 4.2, where we take the transverse direction to be in the plane of $\mathbf{r}_{ij}$ and $\hat{r}$, the radial unit vector at the point of intersection of C_{ij} with the sphere, at which point $\lambda = \lambda_0$. As we are now considering the contribution to the pressure over the

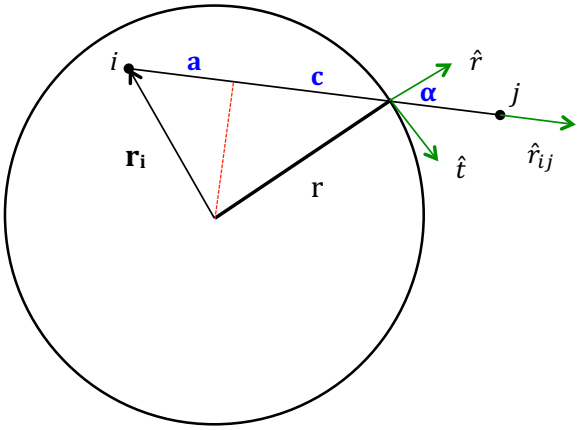

Figure 4.2: A sketch of the geometry for a sample calculation of the transverse pressure component at a radius r. The straight line contour intersects the sphere when $\lambda = \lambda_0$ (see Eq. 4.9), at which point $a + c = \lambda_0 r_{ij}$. Here, the force between i and j is taken to be radial, and forms an angle α with $\hat{r}$, with $\cos\alpha = c/r$ and $a = -\mathbf{r}_i \cdot \hat{r}_{ij}$.

spherical surface, Eq. 4.5 becomes,

$$
\begin{aligned}
P'_{ij,T}(r) &= \frac{1}{2}\frac{1}{4\pi r^2}\int_{C_{ij}} \Big(\mathbf{f}_{ij}\cdot\hat{t}\Big)\Big(d\mathbf{l}\cdot\hat{t}\Big)\,\delta(r-l\,) && (4.32)\\
&= \frac{1}{8\pi r^2}\, f_{ij}\, r_{ij}\sin^2\alpha \int_0^1 d\lambda\,\delta\Big(r - l(\lambda)\Big) && (4.33)\\
&= \frac{1}{8\pi r^2}\, f_{ij}\, r_{ij}\sin^2\alpha \int_0^1 d\lambda\,\frac{\delta(\lambda-\lambda_0)}{|l'(\lambda_0)|} && (4.34)\\
&= \frac{1}{8\pi r^2}\, f_{ij}\,\frac{\sin^2\alpha}{\cos\alpha}, && (4.35)
\end{aligned}
$$

where the extra factor of $\frac{1}{2}$ comes from $\hat{t}$ having both θ and ϕ components and, with the help of Eq. 4.10 and the geometrical arrangement shown in Fig. 4.2, it can be shown that $l'(\lambda_0) = r_{ij}\cos\alpha$. Eq. 4.35 appears in Ref. [16] as Eq. 12, which is itself referenced from [26]. The cosine in the denominator causes a divergence when $\cos\alpha = 0$, i.e., when the C_{ij} becomes tangent to the sphere. Attempts to use Eq. 4.35 to calculate the transverse pressure illustrate the problem, which is formally absent in the coarse-graining method because of the order in which the integration is carried out in obtaining Eq. 4.8.

4.4.3 Obtaining the local pressure from the potential energy

Ikeshoji et al [16] also discusses the method of determining the pressure tensor in $\tilde{V}$ by using the virial expression for the bulk pressure, but only considering particle interactions for which at least one of the particles is in $\tilde{V}$. While this intuitive approach is only a low-order approximation [27], the authors demonstrate for a planar geometry that it fails to respect mechanical equilibrium (Eqs. 4.30 and 4.31) only at the interface.

In the same spirit, we define an expression inspired by the thermodynamic meaning of pressure in the bulk,

$$P_U(r) \equiv \rho(r) k_B T - \left\langle \frac{dU(r)}{d\tilde{V}} \right\rangle_{T,N}, \tag{4.36}$$

where the derivative is calculated in the following way (see Fig. 4.3). For a given nanodroplet configuration, all molecular centres of mass are isotropically expanded according to $\mathbf{r}^{+}_{CM,i} \rightarrow (1+\alpha_+)\mathbf{r}_{CM,i}$, and in this rescaled system we calculate the binding energy $u_i^+ = \sum_{j \neq i} u_{ij}$ for each molecule i originally in $\tilde{V}$, where u_{ij} is the interaction energy between molecules i and j. The rescaled shell volume is $\tilde{V}_+ = (1+\alpha_+)^3\tilde{V}$, and the potential energy associated with the rescaled shell is $U_+ = \frac{1}{2}\sum_{i\in\tilde{V}_+} u_i^+$. To use the centred difference scheme to approximate the derivative,

$$\frac{dU(r)}{d\tilde{V}} \approx \frac{U_+ - U_-}{\tilde{V}_+ - \tilde{V}_-}, \tag{4.37}$$

we similarly rescale the molecular centres of mass according to $\mathbf{r}^{-}_{CM,i} \rightarrow (1+\alpha_-)\mathbf{r}_{CM,i}$ to obtain U_- and $\tilde{V}_-$. We use $\alpha_+ = 10^{-4}$, and then to ensure that $\tilde{V}_+ - \tilde{V} = \tilde{V} - \tilde{V}_-$, we use $\alpha_- = \left[2 - (1+\alpha_+)^3\right]^{1/3} - 1$ (approximately equal to $-\alpha_+$). Note that the same particles are in $\tilde{V}$, $\tilde{V}_+$ and $\tilde{V}_-$ and that the same molecular pairs are used to calculate

U_+ and U_-. This derivative is then averaged over nanodroplet configurations.

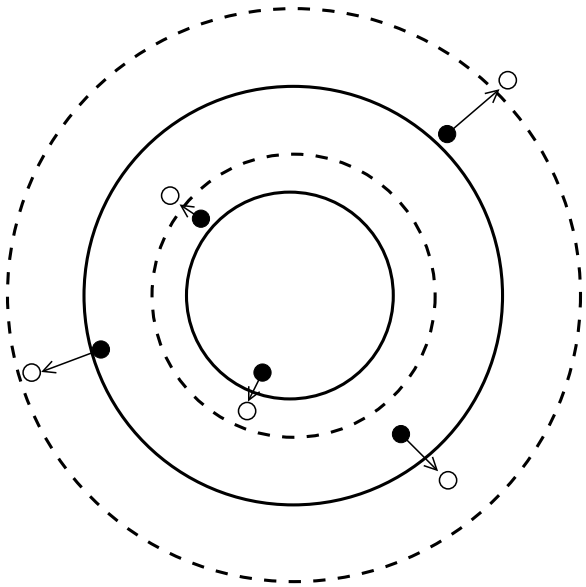

Figure 4.3: A sketch for the calculation of the derivative of the local potential energy $U(r)$ with respect to volume. All particles coordinates are rescaled isotropically according to $\mathbf{r} \to (1+\alpha)\mathbf{r}$ (filled to open circles), resulting in a commensurate change in spherical shell volume $\tilde{V}$ (solid lines) to $(1+\alpha)^3\tilde{V}$ (dashed lines).

4.5 Results

4.5.1 Radial pressure profiles

In Fig. 4.4 we plot various pressure contributions for a nanodroplet of size $N = 1100$. The radial density is proportional to the ideal gas term (black circles), which for this state point accounts for most of the roughly 100 MPa of pressure in the interior of the nanodroplet. There is a small maximum in the density at or near the surface (at $r \approx 1.75$ nm,) where the configurational contributions to the normal [$\bar{P}_{c,N}(r)$ - blue diamonds] and tangential [$\bar{P}_{c,T}(r)$ - red squares] components of the pressure are maximally negative. Despite the large negative values near the surface, $\bar{P}_{c,N}(r)$ and $\bar{P}_{c,T}(r)$ become indistinguishable from each other within the precision of our

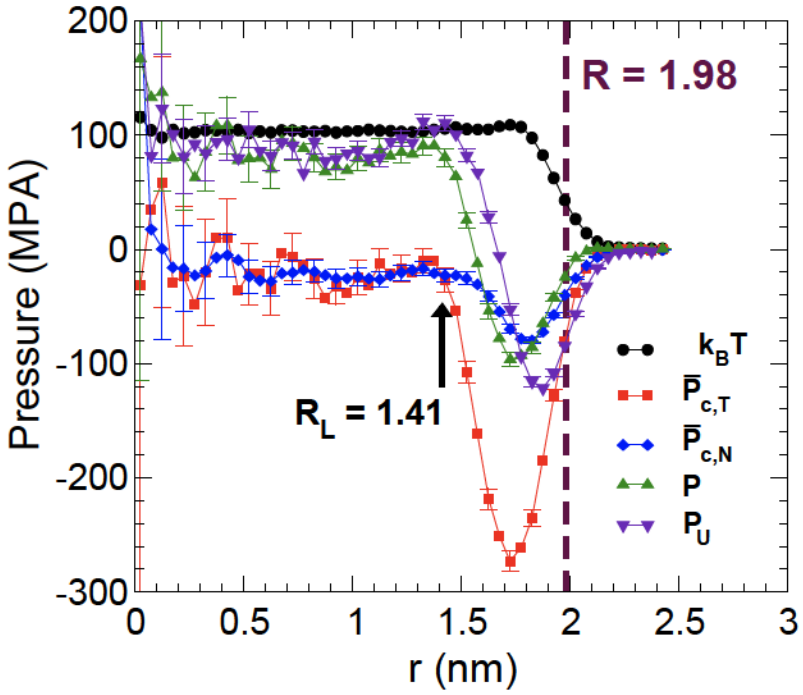

Figure 4.4: Pressure as a function of radial distance from the centre of a nanodroplet of size $N = 1100$ at $T = 220$ K. The radial extent of the droplet is estimated by $R = \sqrt{5/3}R_g = 1.98$ nm, while the configurational contributions to the tangential and radial pressures are approximately equal below the point of crossing at $R_L = 1.41$ nm.

simulations below $R_L \approx 1.41$ nm, indicating that the pressure tensor is isotropic within this radius.

We note that an accurate determination of the centre of mass of the cluster is vital for determining all the radial quantities. It is thus important to exclude gas-like molecules when calculating the centre of mass. When calculating the pressure all particles in the system are used. However, the vapour pressure at $T = 220$ K is nearly zero. For example, a search of the $N = 1100$ configurations sampled, using the definition that a gas-like molecule has two or fewer neighbours within $r_n = 0.63$ nm, found no such molecules. A cluster search employing the definition that two molecules

within $r_n = 0.35$ belong to the same cluster yields the same result [28].

Notwithstanding the progressively larger error bars as $r \to 0$, there appear to be oscillations within both $\bar{P}_{c,N}(r)$ and $\bar{P}_{c,T}(r)$ that may correlate with small oscillations in $\rho(r)$. However, given the precision of our calculations, we can do no better than to assume that $\bar{P}_{c,N}(r)$ and $\bar{P}_{c,T}(r)$ are both equal to the same constant below R_L.

As a consistency check on our results, we verify that our calculated pressure components satisfy mechanical equilibrium by using Eq. 4.31 to recover $P_N(r)$ from $P_T(r)$. We use Eq. 4.31 instead of Eq. 4.30 since numerical integration reduces noise. In Fig. 4.5 we plot both $P_N(r)$ calculated directly from the droplets and as calculated from Eq. 4.31. We see that the two curves are the same within error, even though Eq. 4.31 yields a curve with less pronounced oscillatory behaviour. A global estimate of the numerical integration error can be taken to be the difference between Eq. 4.31 and $P_N(r)$ where the latter decays to zero.

$P_U(r)$ for the same state point is shown in Fig. 4.4, where it agrees, to within error, with $P(r)$ in the interior of the droplet where the pressure is constant with r. At the interface, there is a significant difference, in which $P_U(r)$ exaggerates the extremal values of $P(r)$, and shows a positive pressure peak near the surface. Despite this exaggeration near the surface, $P_U(r)$ shows none of the apparent oscillations seen in $P(r)$.

As this method only relies on the potential energy, it is comparatively a rather straightforward calculation, and so may be of use when interactions are complex and precise determination of the properties near the interface is not required. Furthermore, that the two methods agree within the interior provides a useful check on the results for $P(r)$.

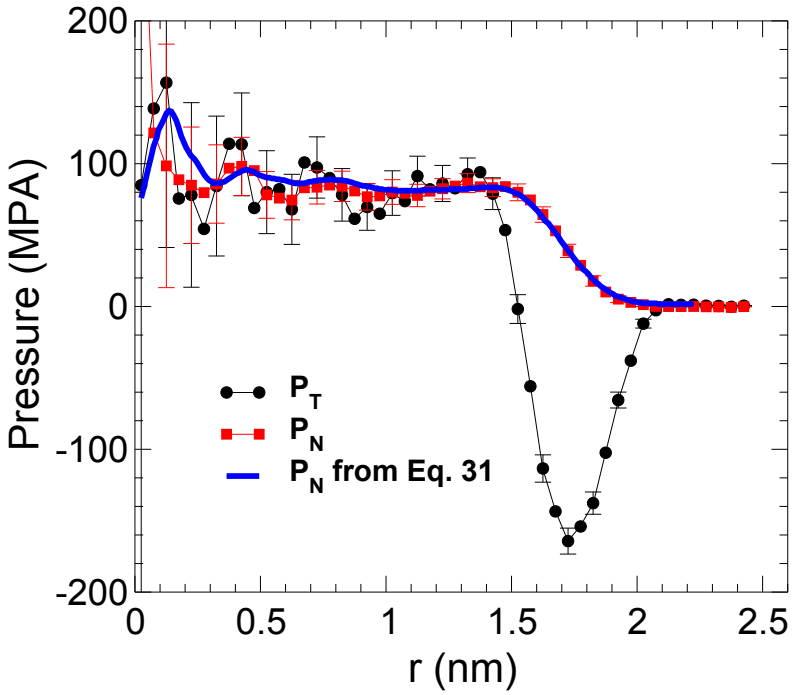

Figure 4.5: Consistency check on the calculation of $P_N(r)$ and $P_T(r)$ for $N = 1100$ and $T = 220$ K.

4.5.2 Laplace pressure relation

To test Eq. 4.1, and noting that the vapour pressure is so small compared to the interior pressure of the nanodroplets, we simply define P_L to be the average of $P(r)$ from $r_{\min} = 0.025$ (our first data point) to R_L, the radial distance to which the pressure tensor is isotropic, i.e., below which point $P_T(r)$ and $P_N(r)$ are indistinguishable:

$$P_L \equiv \frac{3}{4\pi \left(R_L^3 - r_{\min}^3\right)} \int_{r_{\min}}^{R_L} 4\pi r^2 P(r) dr. \tag{4.38}$$

Operationally, we take R_L to be the first crossing of $P_{c,T}(r)$ and $P_{c,N}(r)$ as r decreases below the location of the minimum in $P_{c,T}(r)$. As a measure of the radius of the droplet, treating the nandroplets as spheres of uniform density, we choose

$R = \sqrt{5/3}R_g$, where R_g is the radius of gyration.

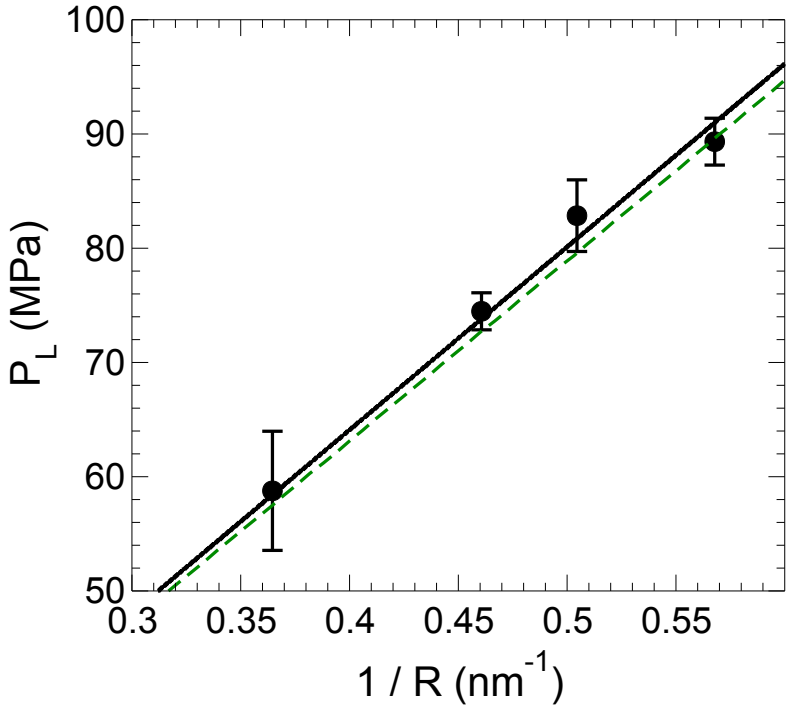

Figure 4.6: Test of the Laplace pressure relation. Plotted is the average isotropic pressure from the interior of nanodroplets as a function of $1/R$, where $R = \sqrt{5/3}R_g$. Solid line is the result of a one-parameter least-squares fit, $P_L = 2(80.1)/R$. The dashed line uses an estimate of $\gamma = 78.9$ mN/m for a planar interface at 220 K [24].

In Fig. 4.6 we plot P_L as a function of $1/R$. We fit the data to $2\gamma_{\rm fit}/R$ and find $\gamma_{\rm fit} = 80.1$. This estimate of γ agrees well with the value $\gamma = 78.9$ mN/m obtained using Eq. 6 in Ref. [24]; the dashed line in Fig. 4.6 shows $2\gamma/R$ using this value of γ.

4.6 Discussion and conclusions

Calculating the local pressure is a non-trivial task and requires good averaging because of significant statistical fluctuations, particularly at small radial distances. We note the discrepancy between our results and the early work on ST2 water clusters of

Brodskaya et al. [13, 14]. They reported a significant drop in the pressure, even to significantly negative values, towards the centre of the droplet. While the droplet sizes they investigated were smaller and at higher T, we speculate that this unexpected result may have arisen from an imprecise determination of the centre of mass or even from sample bias since these early simulations had much shorter run times. A given configuration may have an extremely large (positive or negative) value of $P(r \to 0)$, depending on whether there is a high or low density fluctuation at the centre, which can be considerable given the small number of particles there. As a general remark, statistics for larger r are not only better because of the greater volume over which the average is determined, but because mobility is likely greater the closer a layer is to the surface. However, in the present study we have not excluded the possibility that for smaller droplets, such as those studied in Refs. [13, 14], there exists an effect that reduces the pressure at the centre.

It is important to directly calculate the pressure instead of relying only on the local density and the known bulk equation of state, even when done as elegantly as in a recent test of the Young-Laplace equation for the SPC/E model by pressuring water through a nanopore [30]. We already see a dense region near the surface of the nanodroplet, where the pressure is negative. Clearly, the water in this layer does not follow the bulk equation of state. Further, subtle finite size effects on structure, as noted already in regard to nucleation [7], may affect local pressure more than local density. Thus, water in sufficiently small nanodroplets may not follow the bulk equation of state.

Whether or not droplet interiors represent bulk water also depends on how deeply surface effects propagate inside. At $T = 220$ K, we see, coming in from large r, that the density rises from zero to a local maximum [where $P(r)$ is most negative] in about 0.3 nm (see black curve with circles in Fig. 4.4). Another 0.4 nm further

inside and $P_N(r)$ and $P_T(r)$ become indistinguishable within uncertainty. This non-bulk-like region is 0.7 nm thick and encompasses approximately two molecular layers. This estimate of the size of non-bulk-like region is somewhat smaller than pointed out in Ref. [7], for which there is also observed a local maximum in the stress before quickly tending to a constant at smaller r. However, in our case the interior is at a high pressure and the definition of the local stress used in [7] differs from that of the pressure. We note that $P_U(r)$ also produces a peak near R_L, and would thus also produce a larger estimate of the extent of the non-bulk-like region. This should not be an issue if one is in search of a conservative estimate of what is perhaps bulk-like.

Eq. 4.1 formally models a droplet with a sharp interface at $R = R_s$, at the so-called surface of tension, that separates interior and exterior fluids with isotropic and homogeneous pressures, and ΔP refers to the difference between these fluid pressures. For our droplets, the pressure tensor components become equal and constant with r near the centre (and hence bulk-like), and so we identify ΔP with P_L obtained from the pressure tensor. In using Eq. 4.1 we approximate R_s with $\sqrt{5/3}R_g$. In a more systematic study aiming to quantify the curvature corrections to γ (through the Tolman length δ), the choice of dividing surface should be carefully considered. Nonetheless, our use of $R = \sqrt{5/3}R_g$ yields a γ remarkably consistent with the expected planar value. This may indicate that curvature corrections to γ, and hence δ itself, are small. Calculations for both Lennard-Jones [31] and TIP4P/2005 [32] yield small negative values of δ, around -0.1σ and -0.05 nm respectively, with the magnitude of δ decreasing with decreasing T for TIP4P/2005 [33]. For a future study of smaller droplets, for which curvature effects may become more apparent, the pressure calculation presented here provides the means of directly determining δ from simulation data, as has been done for Lennard-Jones droplets [11]. In addition, density functional theory suggests that δ becomes positive for very small droplets, as implied by a decreasing

γ with R_s [35], and hence in the present study we may be in a droplet size regime where $\delta \approx 0$.

While working with forces between molecules and their centres of mass is more convenient compared to treating molecules as collections of atoms held rigidly by forces of constraint, there is another important advantage of our approach. As recently pointed out by Sega et al. [36], when constraints are used and the kinetic energy tensor is calculated from atomic velocities, the kinetic energy tensor may become anisotropic at a liquid-vapour interface. Failure to consider these anisotropies may, for example, lead to underestimates of γ by approximately 15% for a planar interface. It is thus insufficient, when working with constraints, to only calculate the configuration contribution to the virial and assume an isotropic ideal gas contribution. Velocities are thus required for the pressure calculation. In contrast, we work with the velocities of the molecular centres of mass and intermolecular forces, thus avoiding these difficulties [23]. The molecular approach works essentially because the calculation of pressure stems from the calculation of the force, i.e., the rate of change of the linear momentum with time [24]. The validity of the molecular approach used here, where we assume an isotropic ideal gas contribution, is confirmed in Fig. 4.5, where $P_N(r)$ and $P_T(r)$ are shown to be consistent with mechanical stability. If our ideal gas contribution were incorrect, mechanical stability would appear to be violated. Regardless of the concerns raised by Sega et al. [36], our estimates for P_L are made solely based on the behaviour of the pressure tensor in the interior of the droplets. As a result, anisotropy arising in the region of the surface does not affect our results for P_L.

In summary, we have provided a detailed description of the calculation of the microscopic pressure for spherical droplets of molecular liquids, and checked the results by introducing an approximate energy-based method of calculating the microscopic

isotropic pressure. Our calculation paves the way for a detailed analysis of effects of the local pressure on nucleation, and for direct checks on whether the bulk equation of state remains valid in nanodroplet interiors. For the size range studied, and at fairly deeply supercooled T, we find that γ determined from a flat interface predicts the pressure in the interior of the nanodroplet quite well, despite significant surface features in the radial dependence of the pressure.

Acknowledgments

We thank Richard K. Bowles for enlightening discussions. We thank Natural Sciences and Engineering Research Council (Canada) for funding. Computational facilities are provided by ACENET, a member of Compute Canada and the regional high performance computing consortium for universities in Atlantic Canada. ACENET is funded by the Canada Foundation for Innovation (CFI), the Atlantic Canada Opportunities Agency (ACOA), and the provinces of Newfoundland and Labrador, Nova Scotia, and New Brunswick.

Bibliography

[1] A. Haji-Akbari and P. G. Debenedetti, *Perspective: Surface freezing in water: A nexus of experiments and simulations,* J. Chem. Phys. **147**, 060901 (2017).

[2] T. Li, D. Donadio, and G. Galli, *Ice nucleation at the nanoscale probes no man's land of water,* Nat. Commun. **4**, 1887 (2013).

[3] J. R. Espinosa, A. Zaragoza, P. Rosales-Pelaez, C. Navarro, C. Valeriani, and C. Vega, *Interfacial free energy as the key to the pressure-induced deceleration of ice nucleation,* Phys. Rev. Lett. **117**, 135702 (2016).

[4] V. Molinero and E. B. Moore, *Water Modeled As an Intermediate Element between Carbon and Silicon,* J. Phys. Chem. B **113**, 4008 (2009).

[5] W. L. Jorgensen, J. Chandrasekhar, and J. D. Madura, *Comparison of simple potential functions for simulating liquid water,* J. Chem. Phys. **79**, 926 (1983).

[6] R. G. Fernández, J. L. F. Abascal, and C. Vega, *The melting point of ice I_h for common water models calculated from direct coexistence of the solid-liquid interface,* J. Chem. Phys. **124**, 144506 (2006).

[7] A. Haji-Akbari and P. G. Debenedetti, *Computational investigation of surface freezing in a molecular model of water,* PNAS **114**, 3316 (2017).

[8] W. L. Jorgensen, J. Chandrasekhar, and J. D. Madura, *A potential model for the study of ices and amorphous water:* TIP4P*/Ice,* J. Chem. Phys. **122**, 234511 (2005).

[9] J. A. Sellberg, C. Huang, T. A. McQueen, N. D. Loh, H. Laksmono, D. Schlesinger, R. Sierra, D. Nordlund, C. Y. Hampton, D. Starodub, D. P. DePonte, M. Beye, C. Chen, A. V. Martin, A. Barty, K. T. Wikfeldt, T. M. Weiss, C. Caronna, J. Feldkamp, L. B. Skinner, M. M. Seibert, M. Messerschmidt, G. J. Williams, S. Boutet, L. G. M. Pettersson, M. J. Bogan, and A. Nilsson, *Ultrafast X-ray probing of water structure below the homogeneous ice nucleation temperature,* Nature **510**, 381 (2014).

[10] J. F. Huang and L. S. Bartell , *Kinetics of homogeneous nucleation in the freezing of large water clusters.* J. Phys. Chem. **12**, 3924 (1995).

[11] A. Manka, H. Pathak, S. Tanimura, J. Wölk, R. Strey, and B. E. Wyslouzil, *Freezing water in no-man's land.* Phys. Chem. Chem. Phys. **14**, 4505 (2012).

[12] C. C. Pradzynski, R. M. Forck, T. Zeuch, P. Slavicek, and U. Buck, *A fully size-resolved perspective on the crystallization of water clusters,* Science **337**, 1529 (2012).

[13] E. N. Brodskaya and A. I. Rusanov, *The molecular dynamics simulation of water clusters,* Mol. Phys. **62**, 251 (1987).

[14] E. N. Brodskaya, J. C. Eriksson, A. Laaksonen, and A. I. Rusanov, *The pressure tensor and local density profiles of computer-simulated water clusters,* Mendeleev Commun. **3**, 136 (1993).

[15] S. M. Thompson, K. E. Gubbins, J. P. R. B. Walton, R. A. R. Chantry, and J. S. Rowlinson, *A molecular dynamics study of liquid drops,* J. Chem. Phys. **81**, 530 (1984).

[16] T. Ikeshoji, B. Hafskjold, and H. Furuholt, *Molecular-level calculation scheme for pressure in inhomogeneous systems of flat and spherical layers,* Mol. Simul. **29**, 101 (2003).

[17] H. J. C. Berendsen, J. R. Grigera, and T. P. Straatsma, *The missing term in effective pair potentials,* J. Chem. Phys. **91**, 6269 (1987).

[18] O. S. Subbotin, V. R. Belosludov, T. Ikeshoji, E. N. Brodskaya, E. M. Piotrovskaya, V. V. Sizov, R. V. Belosludov, and Y. Kawazoe, *Modeling the Self-Preservation Effect in Gas Hydrate/Ice Systems,* Mater. Trans. **48**, 2114 (2007).

[19] T. Nakamura, W. Shinoda, and T. Ikeshoji, *Novel numerical method for calculating the pressure tensor in spherical coordinates for molecular systems,* J. Chem. Phys. **135**, 094106 (2011).

[20] J. L. F. Abascal and C. Vega, *A general purpose model for the condensed phases of water*: TIP4P/2005, J. Chem. Phys. **123**, 234505 (2005).

[21] H. J. C. Berendsen, D. van der Spoel, and R. van Druren, *GROMACS: A message-passing parallel molecular dyanmics implemmentation,* Comput. Phys. Commun. **91**, 43 (1995); E. Lindahl, B. Hess, and D. van der Spoel, *GROMACS 3.0: A package for molecular simulation and trajectory analysis,* J. Mol. Model. **7**, 306 (2001); D. van der Spoel, E. Lindahl, B. Hess, G. Groenhof, A. E. Mark, and H. J. C. Berendsen, *GROMACS: Fast, Flexible and Free,* J. Comput. Chem. **26**, 1701 (2005); B. Hess, C. Kutzner, D. van der Spoel, and

E. Lindahl, *GROMACS 4: Algorithms for highly efficient, load balanced, and scalable molecular simulation,* J. Chem. Theory Comput. **4**, 435 (2008).

[22] F. Sciortino, P. Tartaglia, and E. Zaccarelli, *One-Dimensional Cluster Growth and Branching Gels in Colloidal Systems with Short-Range Depletion Attraction and Screened Electrostatic Repulsion,* J. Phys. Chem. B **109**, 21942 (2005).

[23] J. Alejandre, D.J. Tildesley, and G.A. Chapela, *Molecular dynamics simulation of the orthobaric densities and surface tension of water,* J. Chem. Phys. **102**, 4574 (1995).

[24] P. Schofield and J. R. Henderson *Statistical Mechanics of inhomogeneous fluids,* Proc. R. Soc. Lond. **A379**, 231 (1982).

[25] A.J.H. Irving and J.G. Kirkwood, *The statistical mechanical theory of transport processes. IV. The equations of hydrodynamics,* J. Chem. Phys. **18**, 817 (1950).

[26] B. Hafskjold and T. Ikeshoji, *Microscopic pressure tensor for hard-sphere fluids,* Phys. Rev. E **66**, 011203 (2002).

[27] B. D. Todd, D. J. Evans, and P. J. Daivis, *Pressure tensor for inhomogeneous fluids,* Phys. Rev. E **52** 1627 (1995).

[28] E. M. Sevick, P. A. Monson, and J. M. Ottino, *Monte Carlo calculations of cluster statistics in continuum models of composite morphology,* J. Chem. Phys. **88**, 1198 (1988).

[29] C. Vega and E. de Miguel, *Surface tension of the most popular models of water by using the test-area simulation method,* J. Chem. Phys. **126**, 154707 (2007).

[30] H. Liu and G. Cao, *Effectiveness of the Young-Laplace equation at nanoscale,* Sci. Rep. **6**, 23936 (2016).

[31] E. M. Blokhuis and A. E. van Giessen, *Density functional theory of a curved liquid-vapour interface: evaluation of the rigidity constants,* J. Phys.: Condens. Matter **25**, 225003 (2013).

[32] M. N. Joswiak, N. Duff, M. F. Doherty, and B. Peters, *Size-dependent surface free energy and Tolman-corrected droplet nucleation of TIP4P/2005 water,* J. Phys. Chem. Lett. P**4**, 4267 (2013).

[33] O. Wilhelmsen, D. Bedeaux, and D. Reguera, *Communication: Tolman length and rigidity constants of water and their role in nucleation,* J. Chem. Phys. **142**, 171103 (2015).

[34] A. E. van Giessen and E. M. Blokhuis, *Direct determination of the Tolman length from the bulk pressures of liquid drops via molecular dynamics simulations,* J. Chem. Phys. **131**, 164705 (2009).

[35] S. Ghosh and S. K. Ghosh, *Density functional theory of size-dependent surface tension of Lennard-Jones fluid droplets using a double well type Helmholtz free energy functional,* J. Chem. Phys. **135**, 124710 (2011).

[36] M. Sega, B. Fabian, and P. Jedlovszky, *Nonzero ideal gas contribution to the surface tension of water,* J. Phys. Chem. Lett. **8**, 2608 (2017).

Chapter 5

Thermodynamic and structural anomalies of water nanodroplets

Reproduced with permission from Shahrazad M.A. Malek, Peter H. Poole, and Ivan Saika-Voivod, Nat. Commun. (2018) 10.1038/s41467-018-04816-2.

5.1 Abstract

Liquid water nanodroplets are important in earth's climate, and are valuable for studying supercooled water because they resist crystallization well below the bulk freezing temperature. Bulk liquid water has well-known thermodynamic anomalies, such as a density maximum, and when supercooled is hypothesized to exhibit a liquid-liquid phase transition (LLPT) at elevated pressure. However, it is not known how these bulk anomalies might manifest themselves in nanodroplets. Here we show, using simulations of the TIP4P/2005 water model, that bulk anomalies occur in nanodroplets as small as 360 molecules. We also show that the Laplace pressure inside small droplets reaches 220 MPa at 180 K, conditions close to the LLPT of TIP4P/2005. While the

density and pressure inside nanodroplets coincide with bulk values at moderate supercooling, we show that deviations emerge at lower temperature, as well as significant radial density gradients, which arise from and signal the approach to the LLPT.

5.2 Introduction

Nanoscale particles of water are a key component of important processes in the earth's atmosphere, planetary and interstellar space, and numerous technology applications [1, 6, 5, 4, 2]. For example, nanometer-sized aqueous aerosol droplets are common in earth's lower atmosphere, and understanding their role in cloud formation is critical for climate prediction [6]. The crystallization of pure water nanodroplets has attracted particular interest because the temperature at which freezing is observed, relative to bulk water, decreases dramatically with size, reaching 202 K for nanodroplets of radius 3.2 nm [7]. This effect arises from a combination of influences: Surface effects normally lower the melting temperature of a small system relative to the bulk [8]; a smaller system volume yields fewer nucleation events [9]; and, importantly for experiments, the large surface-to-volume ratio of a small droplet makes rapid cooling rates possible, allowing the establishment of low-temperature conditions on a time scale shorter than the nucleation time [11, 10].

On cooling, bulk liquid water exhibits well-known thermodynamic anomalies, such as the density maximum at 277 K [12]. As the temperature T decreases into the supercooled regime, these anomalies become progressively more dramatic. For example, both the specific heat and the isothermal compressibility of the liquid increase strongly as T decreases. To account for these anomalies, several thermodynamic scenarios have been proposed, including the hypothesis that a liquid-liquid phase transition (LLPT) occurs in deeply supercooled water [13, 14]. However, bulk samples of liquid wa-

ter crystallize at a homogeneous nucleation temperature T_{H} (encountered at ambient pressure in the range 227-232 K, where the precise value depends on the experimental protocol [15, 10, 16, 17, 18]), which to date has prevented the direct observation of the LLPT predicted to occur at lower T. The ability of water nanodroplets to remain liquid below T_{H} presents a promising opportunity to clarify the properties of deeply supercooled water, provided that the bulk anomalies are not suppressed as the number of molecules N in a nanodroplet decreases [11, 7, 19, 16].

In addition, as the size of water nanodroplets decreases, they access a range of pressure P above ambient, due to the Laplace pressure P_{L} that arises inside a liquid droplet. As pointed out in Ref. [19], the increase of P_{L} in small water nanodroplets also contributes significantly to the decrease of their freezing temperature. From the Young-Laplace equation $P_{\mathrm{L}} = 2\gamma/R$, where R is the droplet radius and γ is the surface tension, P_{L} inside a 1 nm droplet should exceed 10^2 MPa [19, 23]. This is high enough to approach the range of P in which the critical point of the proposed LLPT is estimated to occur in bulk water [14, 21]. Water nanodroplets thus permit exploration of a significant range of both T and P relevant to understanding deeply supercooled water.

Despite the importance of liquid water nanodroplets, and their potential to help clarify the behaviour of bulk water, relatively little is known of their fundamental thermophysical properties. This is due to the significant experimental challenges associated with studying liquid nanodroplets that are not in contact with a supporting or confining surface. To date, experimental and simulation studies of pure liquid water nanodroplets have focussed largely on freezing and melting behaviour [8, 7, 19, 22, 23, 24, 25, 26, 27, 28], as well as the formation of amorphous solid nanoparticles [29]. However, a systematic description is lacking for how basic nanodroplet properties, such as R, P_{L}, or the droplet density profile, vary with both N and T. Knowledge

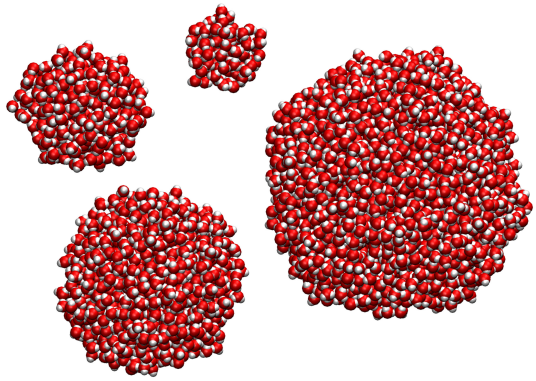

Figure 5.1: Snapshots of simulated liquid water nanodroplets. Equilibrium nanodroplets at $T = 200$ K for various sizes $N = 100$, 360, 1100 and 2880.

of this variation is necessary to determine the regime in which bulk liquid properties, including the anomalies of bulk water, first emerge as nanodroplets grow in size. Also lacking is an understanding of how a liquid nanodroplet will behave under T-P conditions at which the corresponding bulk liquid exhibits a LLPT.

Here we seek to address these knowledge gaps through computer simulations of water nanodroplets, modelled using the TIP4P/2005 interaction potential [19]. The TIP4P/2005 model is known to reproduce the phase behaviour and thermodynamic anomalies of bulk water over a wide range of T and P, and also predicts the occurrence of a LLPT with a critical point located at $T_c = 182$ K and $P_c = 170$ MPa [21]. As we will show, by comparing nanodroplet and bulk behaviour for the same water model, we self-consistently estimate the range of N for which bulk properties emerge, and also identify novel nanodroplet behaviour that occurs when approaching the conditions of the bulk LLPT observed in the model.

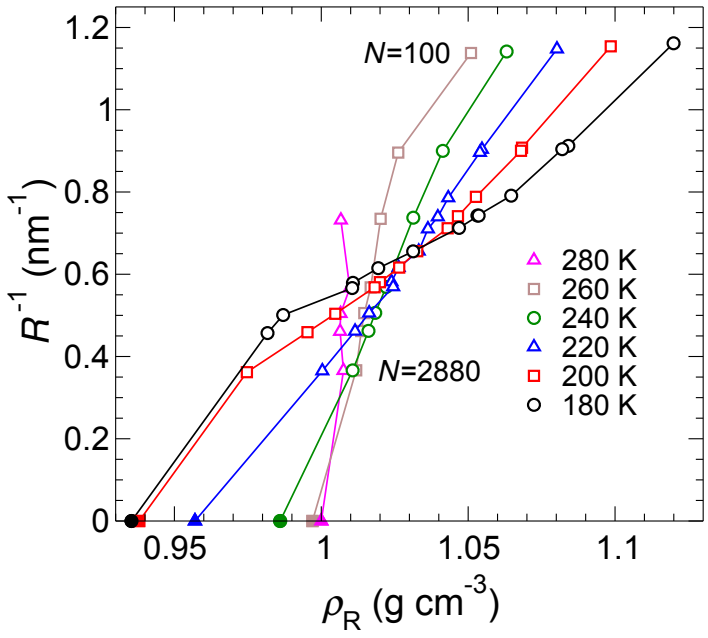

Figure 5.2: Variation of nanodroplet radius R with temperature T and number of molecules N. Isotherms of R^{-1} versus the effective droplet density $\rho_R = 3mN/4\pi R^3$. The statistical error for both R^{-1} and ρ_R is smaller than the symbol size. N decreases with increasing R^{-1} along each isotherm. The filled symbols locate the bulk behaviour expected for droplets as $R \to \infty$ and $N \to \infty$.

5.3 Results

5.3.1 Anomalous variation of the nanodroplet radius

We study isolated equilibrium nanodroplets consisting of N molecules, where N ranges from 100 to 2880, for T from 180 to 300 K; see Methods for details of our simulations. Example nanodroplets from our simulations are shown in Fig. 5.1.

We characterize the nanodroplet size as a function of N and T by evaluating the average radius R, as described in Methods. If the density of droplets is constant, then R^3 will be proportional to N. In order to reveal more subtle variations in $R(N,T)$, we first define an effective droplet density as determined by R as $\rho_R = 3mN/4\pi R^3$, where m is the mass of a water molecule, in order to scale out the approximate proportionality of R^3 and N. Next, we note from the Young-Laplace

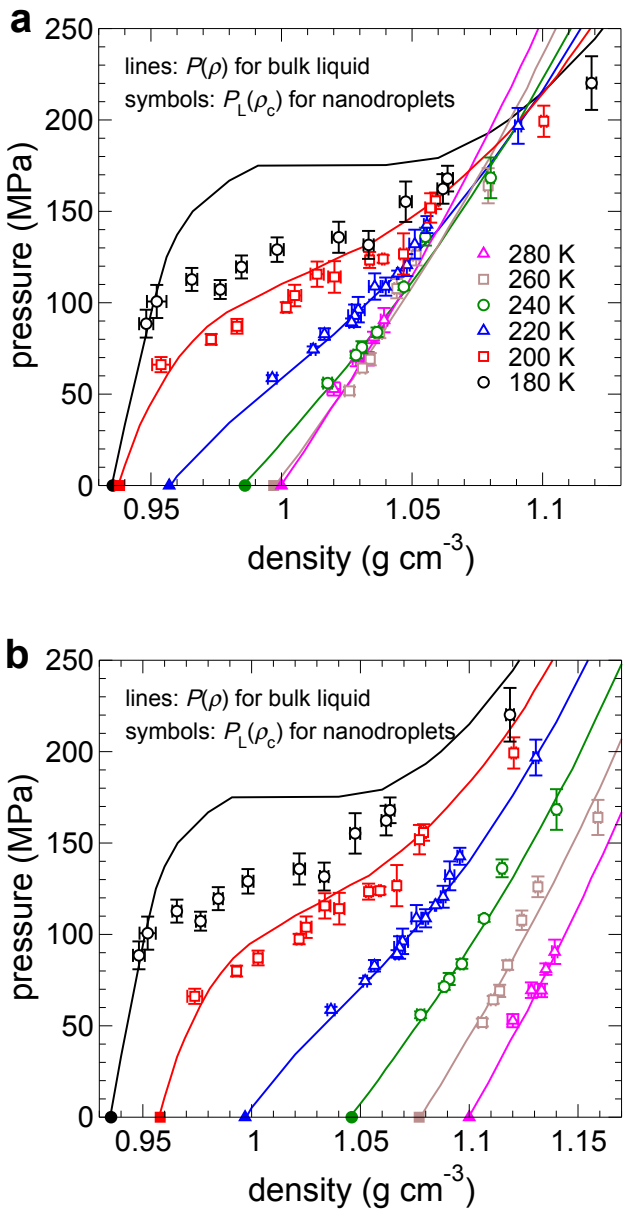

Figure 5.3: Equations of state for bulk liquid and nanodroplets of TIP4P/2005. **a** Isotherms of $P(\rho)$ for the bulk liquid (solid lines), taken from the EOS presented in Ref. [21]; and $P_{\mathrm{L}}(\rho_{\mathrm{c}})$ for water nanodroplets (open symbols). N decreases with increasing density along each isotherm. The filled symbols locate the bulk behaviour expected for droplets as $R \to \infty$ and $N \to \infty$. Lines and symbols of the same colour correspond to the same T. **b** Same as in **a**, but to permit easier examination of each isotherm, all data for $T = 200$ K have been shifted horizontally by 0.02 g cm^{-3}; for 220 K by 0.04 g cm^{-3}; for 240 K by 0.06 g cm^{-3}; for 260 K by 0.08 g cm^{-3}; and for 280 K by 0.10 g cm^{-3}. Legend is the same as in **a**. In both panels, error bars represent one standard deviation of the mean.

equation that γ/R should be proportional to P_{L}. As we will see below, we find that γ is approximately constant at fixed T over the range of R studied here. Hence R^{-1} should be proportional to P_{L} along isotherms, and so R^{-1} can serve as a proxy for the pressure inside a nanodroplet. We therefore present in Fig. 5.2 our data for $R(N,T)$ plotted as isotherms of R^{-1} versus ρ_R, a form analogous to the equation of state (EOS) of a bulk liquid when plotted as isotherms of P versus the bulk liquid density ρ.

The EOS of the TIP4P/2005 bulk liquid is shown in Fig. 5.3a, and displays several important anomalies of water [12, 21]. When an EOS is presented as isotherms of P versus ρ, as in Fig. 5.3a, the occurrence of a density maximum along isobars is indicated by the crossing of isotherms. That is, if two isotherms intersect in the ρ-P plane, then the density is equal at two different T at the same P, a condition that occurs on either side of a density maximum. A maximum in the isothermal compressibility $K_T = \rho^{-1}(\partial\rho/\partial P)_T$ as a function of P at fixed T corresponds to the emergence of an inflection in the isotherms at the lowest T. Increasing K_T on cooling is reflected in the decreasing slope of the isotherms as a function of T at fixed P, and is a precursor of the divergence of K_T at the critical point of the proposed LLPT.

Each of the anomalous features enumerated above for the bulk EOS is also observed in the nanodroplet isotherms derived from $R(N,T)$ and plotted in Fig. 5.2. That is, the nanodroplet isotherms for R^{-1} versus ρ_R also cross; inflect at low T; and exhibit a range of R^{-1} in which the slope decreases as T decreases. We thus find that the variation of R with N and T exhibits the signatures of water's bulk anomalies as observed over a wide range of ρ and P. The occurrence of this qualitative correspondence is remarkable, given that these nanodroplets are extremely small relative to a bulk system, and have no external pressure applied to them.

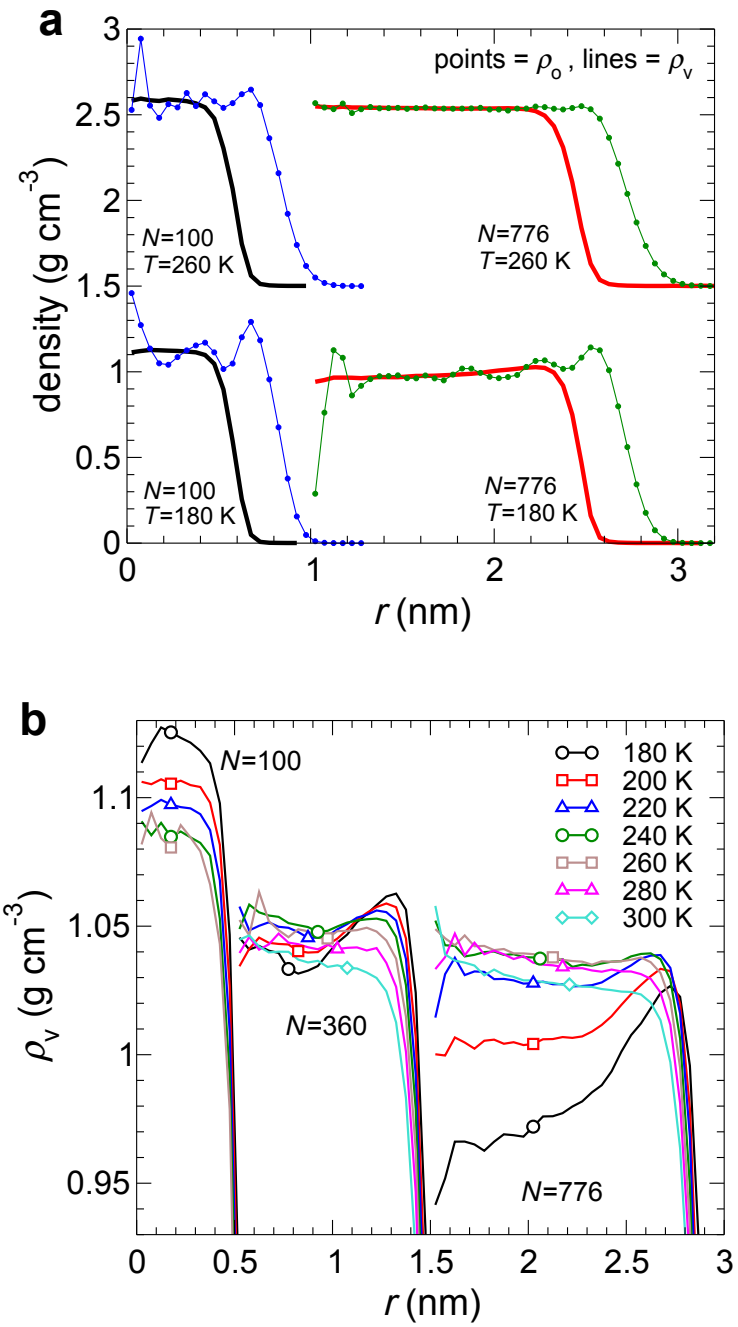

Figure 5.4: Nanodroplet density profiles. **a** Density profiles $\rho_o(r)$ (symbols) and $\rho_v(r)$ (lines) for water nanodroplets at various N and T. For $T = 260$ K, the curves have been shifted vertically by 1.5 g cm^{-3}. For $N = 776$, the curves have been shifted horizontally by 1 nm. **b** $\rho_v(r)$ at various N and T. For $N = 360$, the curves have been shifted horizontally by 0.5 nm; and for $N = 776$ by 1.5 nm. In **a** and **b**, note that the error increases as $r \to 0$; see Supplementary Figs. 5.10 and 5.11.

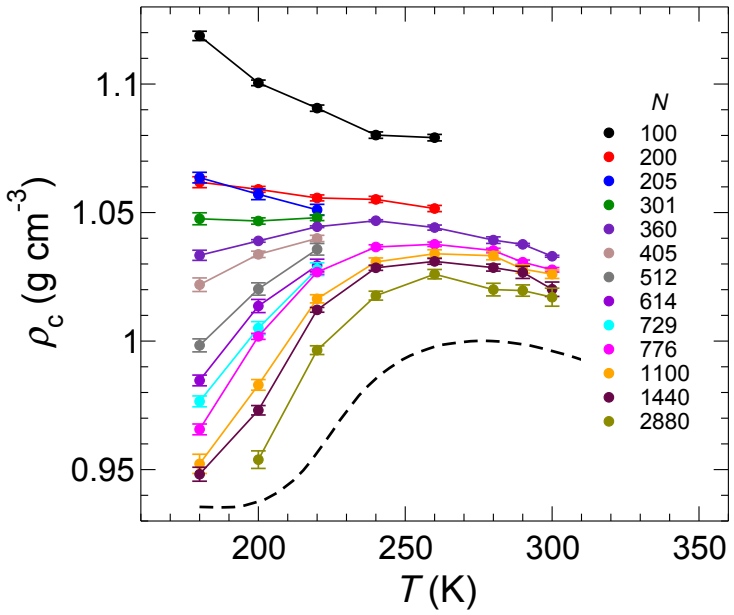

Figure 5.5: Density maximum of liquid nanodroplets. Plot of ρ_c versus T for water nanodroplets of fixed N (symbols). The dashed line is the $P = 0$ isobar of ρ for bulk TIP4P/2005 water taken from Ref. [21], which corresponds to the expected behaviour of ρ_c for droplets as $N \to \infty$. Error bars represent one standard deviation of the mean.

5.3.2 Density profile of nanodroplets

To quantify the internal structure of our nanodroplets, we study the density as a function of the distance r from the droplet centre of mass. We first compute $\rho_o(r)$, the density of molecules that have their centres of mass in a shell of radius r, shown in Fig. 5.4a. As noted in previous simulations of water nanodroplets [19, 27, 29], we observe oscillations in $\rho_o(r)$ that are especially prominent near the surface, indicating that the interface with the vacuum is a well-defined molecular layer, the influence of which propagates inward as a succession of concentric shells. The amplitude of these oscillations is larger at lower T and for smaller N.

Although the oscillations of $\rho_o(r)$ reveal the shell-like structure of nanodroplets, their large amplitude makes it difficult to define an average density for the droplet interior. As an alternative measure of the density profile, we compute the Voronoi

cells for all O atoms, ignoring the H atoms. Within each shell of radius r, we compute the total volume $\mathcal{V}(r)$ of the Voronoi cells for O atoms, as well as $\mathcal{N}(r)$, the number of O atoms. We define the average density as determined by the Voronoi cell volumes as $\rho_{\rm v}(r) = m\langle \mathcal{N}(r)/\mathcal{V}(r)\rangle$, where $\langle \cdots \rangle$ indicates an average over the configurations sampled in our simulations. As shown in Fig. 5.4a and Supplementary Fig. 5.10, the oscillations observed in $\rho_{\rm o}(r)$ are absent in $\rho_{\rm v}(r)$, allowing more precise tracking of the density variation in the droplet interior. Note that the Voronoi cells for molecules at the droplet surface have a divergent volume, and so $\rho_{\rm v}(r)$ vanishes for the outer-most molecular layer.

Fig. 5.4b and Supplementary Fig. 5.11 show $\rho_{\rm v}(r)$ for a wide range of N and T, and reveal complex changes in internal structure. In particular, we observe the emergence of a density maximum as N increases. The density at all r for our smallest droplets ($N = 100$) increases monotonically as T decreases. For $N = 360$, the density near the centre passes through a maximum as T decreases, although the surface density still increases monotonically. For larger droplets (e.g. $N = 776$), the density at almost all r passes through a maximum as T decreases.

We define the droplet core density as $\rho_{\rm c} = m\langle \mathcal{N}_{\rm c}/\mathcal{V}_{\rm c}\rangle$, where $\mathcal{N}_{\rm c}$ is the number of O atoms within $r_c = 0.5$ nm of the droplet centre, and $\mathcal{V}_{\rm c}$ is the total volume of the Voronoi cells for these atoms. (For $N \leq 205$ we use $r_c = 0.25$ nm, since for our smallest droplets the effect of the surface extends closer to the centre.) Fig. 5.5 shows $\rho_{\rm c}$ as a function of T for fixed N, and confirms that a density maximum occurs in the core of water nanodroplets as small as $N = 360$.

The density maximum of bulk water occurs as its random tetrahedral network (RTN) structure becomes more prominent as T decreases [12]. At low T, we find that $\rho_{\rm c}$ tends towards the density of the bulk RTN (~ 0.94 g cm^{-3}) for our larger nanodroplets. Despite the disruption of bulk-like structure occurring at the nanodroplet

surface, the evolution of our density profiles as T decreases is thus driven by the formation of a low-density RTN in the droplet core. A similar low density core was observed in recent simulations of glassy water nanoparticles [29]. Notably, the onset of ice crystallization in nanodroplets is observed experimentally also when N reaches 250-300 [24], consistent with our finding that this is the range of N in which a density maximum and a RTN structure emerge with decreasing T.

Our results also show that, as a consequence of RTN formation in the droplet core, the density profile of a nanoscale water droplet undergoes a dramatic "density inversion" as T decreases: As shown in Fig. 5.4b and Supplementary Fig. 5.11, high-T droplets have a denser core and a slightly less dense surface, as expected for a simple liquid droplet, while low-T droplets have a less dense core and a distinctly denser surface. In Methods, we describe a procedure to define the maximum density $\rho_{\rm s}$ in the surface region of $\rho_{\rm v}(r)$. In Fig. 5.6a we plot the difference $\rho_{\rm s} - \rho_{\rm c}$ as a function of T. We find for all $N \geq 200$ that $\rho_{\rm s} - \rho_{\rm c}$ is slightly negative at high T and is positive and rapidly increasing at low T. Despite the emergence of the RTN in the droplet core as T decreases, the equilibrium droplet structure at low T always exhibits a higher density liquid layer at the interface with the vapour.

5.3.3 Laplace pressure and equation of state for nanodroplets

At low T, $\rho_{\rm c}$ varies by more than 15%, suggesting that $P_{\rm L}$ inside our droplets changes considerably with N. To measure $P_{\rm L}$ directly, rather than relying on the Young-Laplace equation, we evaluate the configurational contributions to the tangential and normal components of the pressure, $P_{\rm T}$ and $P_{\rm N}$, as functions of r, shown in Fig. 5.7a and Supplementary Fig. 5.12 [31, 23]. We find that there is a region within each droplet where $P_{\rm T} \simeq P_{\rm N}$, as occurs in a bulk liquid, and we define $P_{\rm L}$ as the average of the total pressure $P_{\rm tot}$ in this region (see Methods). In Fig. 5.7b we see that isotherms

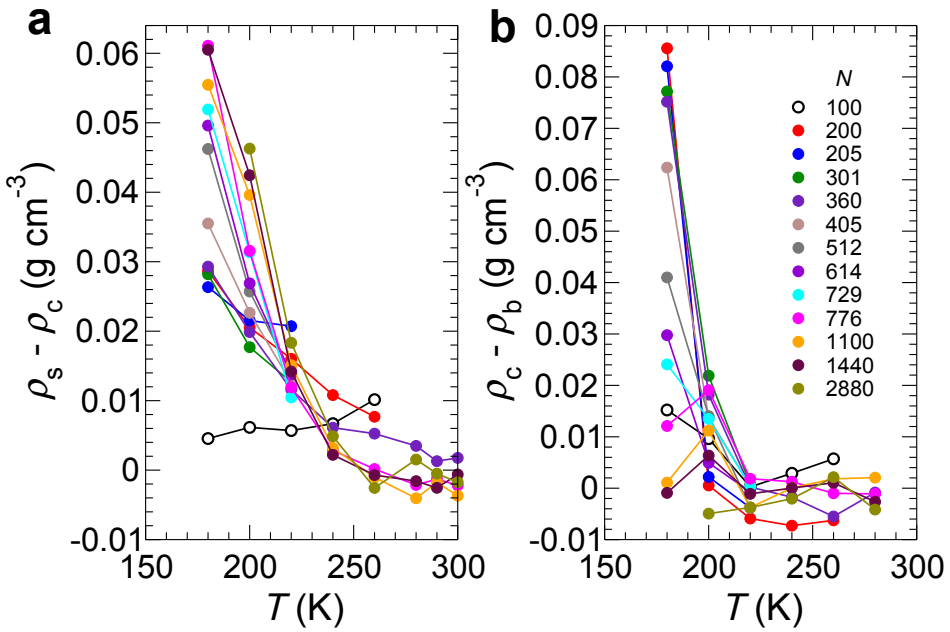

Figure 5.6: Emergence of density differences within nanodroplets with decreasing temperature. **a** $\rho_s - \rho_c$ versus T, and **b** $\rho_c - \rho_b$ versus T, for nanodroplets of various N, as indicated in the legend.

of P_L are proportional to R^{-1}, consistent with the prediction of the Young-Laplace equation. Fig. 5.7b confirms that the variation of P_L with N is large, reaching more than 200 MPa for our smallest nanodroplets at low T.

We estimate γ from the slopes of the isotherms in Fig. 5.7b. In Supplementary Fig. 5.13 we compare our γ values to results obtained previously using TIP4P/2005 for the surface tension γ_p of a planar liquid-vapour interface [32]. Although the T ranges of the two data sets do not overlap, our result at 280 K is quantitatively consistent with the value of γ_p at 300 K. This agreement, and the linearity of the isotherms in Fig. 5.7b, suggests that γ for a strongly curved interface (our results) and a flat one (γ_p from Ref. [32]) differ little, i.e. that the Tolman length may be close to zero [33]. On the other hand, our results for γ increase more rapidly with decreasing T than indicated by the low-T extrapolation of γ_p given in Ref. [32]. This difference may arise due to the emergence at low T of the complex and inverted density profiles shown in

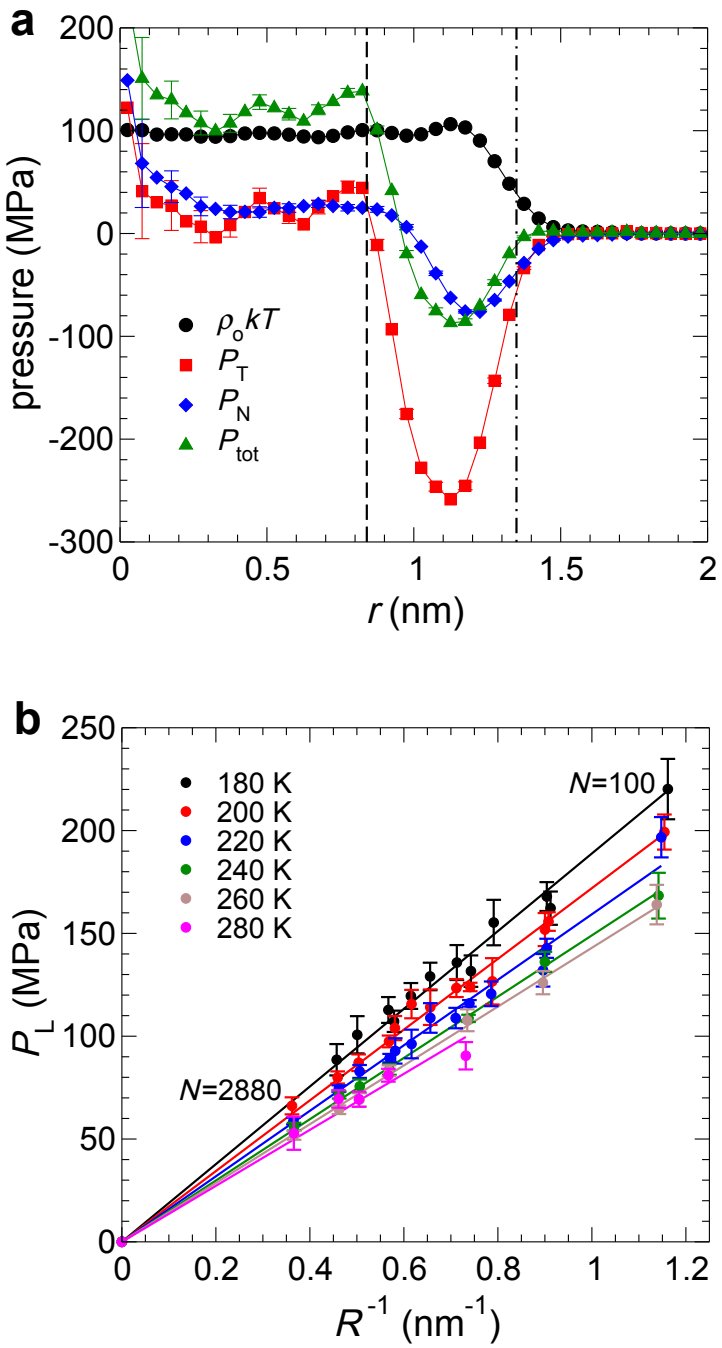

Figure 5.7: Laplace pressure inside nanodroplets. **a** Contributions to the pressure inside a water nanodroplet as a function of r, for $N = 360$ and $T = 200$ K. Vertical lines identify $r = R_L$ (dashed) and $r = R$ (dot-dashed). **b** Isotherms of P_{L} as a function of R^{-1}. Note that N decreases with R^{-1} along each isotherm. The point at the origin is the expected value of P_{L} for droplets as $R \to \infty$. The straight lines are fits of the Young-Laplace equation $P_{\mathrm{L}} = 2\gamma/R$ to the data along each isotherm. The error for R^{-1} is smaller than the symbol size; the error in P_{L} represents one standard deviation of the mean.

Fig. 5.4b, or of curvature effects, or both. Further work is required to clarify these influences.

We compare in Fig. 5.3 the correspondence between the EOS of the bulk liquid, and the variation of P_{L} with ρ_{c} along isotherms in our nanodroplets. For $T \geq 220$ K, we find that the bulk and nanodroplet EOS isotherms agree within statistical error for all N. Our results thus show that the density maximum observed in Fig. 5.5, which occurs in the range 240-260 K, is a consequence of the ability of nanodroplets to follow the bulk EOS for $T \geq 220$ K, where the bulk density maximum also occurs. Interestingly, we also find that the absence of a density maximum at small N in Fig. 5.5 is not due to deviations from the bulk EOS. Instead, the density maximum disappears because the path followed by a nanodroplet of fixed N in the EOS deviates strongly from an isobar for small N, as shown in Fig. 5.8a.

5.3.4 Nanodroplet behaviour approaching the LLPT

Despite the good correspondence in Fig. 5.3 between the nanodroplet and bulk EOS for $T \geq 220$ K, we find that the agreement breaks down for $T \leq 200$ K. Specifically, the data points on the nanodroplet isotherms for 200 and 180 K lie at higher density than the bulk for all but our largest droplets. We quantify this deviation in Fig. 5.6b, where we plot the difference between ρ_{c} for a given droplet, and ρ_{b}, the density of a bulk liquid having the same T and $P = P_{\mathrm{L}}$ as the droplet. Not surprisingly, the largest droplets maintain their bulk-like properties at all T, as they must in the limit $N \to \infty$. However, for $N \leq 776$, we observe a dramatic loss of bulk-like character at low T. An interesting exception to this trend occurs for our smallest droplet ($N = 100$), which shows only a modest deviation compared e.g. to $N = 200$.

This complex behaviour can be understood by considering the influence of the LLPT that occurs in TIP4P/2005 on the shape of the bulk EOS (Fig. 5.3), in concert

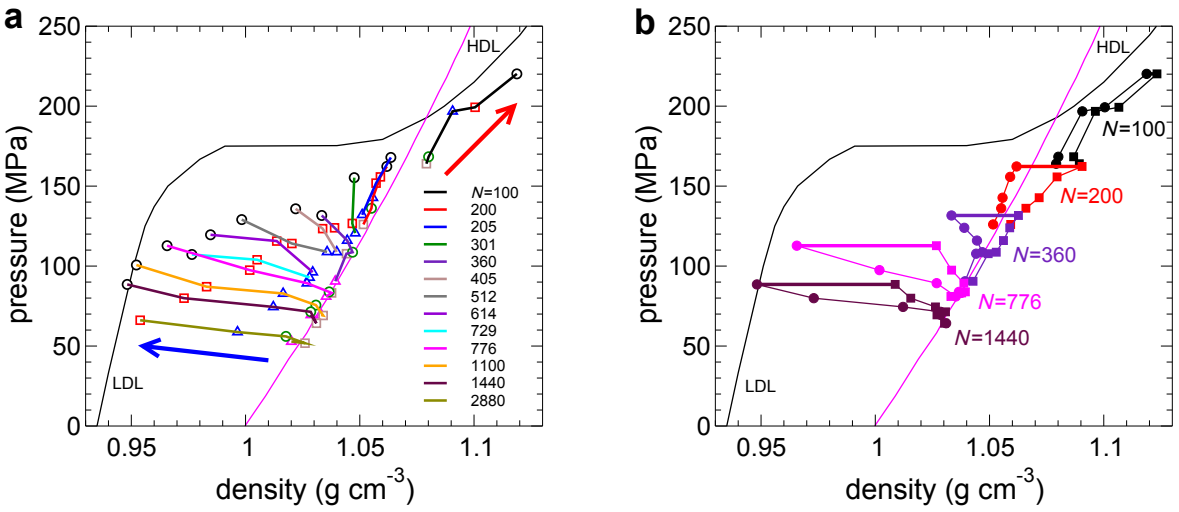

Figure 5.8: Variation of density and pressure with temperature inside nanodroplets of various sizes. **a** Same data as in Fig. 5.3a for P_{L} versus ρ_{c}, except here data points with the same N are connected by coloured lines as indicated in the legend. Symbol types have the same meaning as in Fig. 5.3a. Error bars are omitted for clarity. The blue and red arrows indicate the direction of decreasing T along a curve of constant N. Note that for large N, lines of constant N are nearly isobaric, whereas as N becomes small, strong deviations from isobaric behaviour are observed. **b** P_{L} versus ρ_{c} (circles), and P_{L} versus ρ_{s} (squares) for droplets of various N. Note that T varies along each curve, from 280 to 180 K (for $N = 360$, 776 and 1440) and from 260 to 180 K (for $N = 200$ and 100). Data points for ρ_{c} and ρ_{s} at 180 K with the same N are joined by a thick horizontal line, to highlight their difference at low T. In both **a** and **b**, isotherms of P versus ρ for the bulk liquid are shown for $T = 180$ K (thin black line) and 280 K (thin magenta line). The branches of the 180 K bulk isotherm corresponding to LDL and HDL are indicated.

with the unusual density profiles observed in our droplets (Fig. 5.4). Fig. 5.8a shows our nanodroplet EOS data plotted so as to highlight the path in the ρ_c-P_L plane followed by a droplet of fixed N as T decreases. For all droplets with $N \geq 200$, we find that P_L is less than P_c for the LLPT of TIP4P/2005. On cooling, ρ_c for these droplets tends towards the low density liquid (LDL) branch of the bulk EOS. These droplets also develop inverted density profiles as shown in Fig. 5.4, in which ρ_c separates from ρ_s at low T; this growing separation is illustrated in the density-pressure plane in Fig. 5.8b. Since the surface remains dense, a large density gradient must occur in order for ρ_c to reach ρ_b at low T. Although our largest droplets are big enough to accommodate the required gradient, for $N \leq 776$ we find that the droplets are too small for ρ_c to reach ρ_b (see Supplementary Fig. 5.14). As a consequence, bulk-like properties are not attained in the cores of our smaller droplets ($200 \leq N \leq 776$) at low T, resulting in the EOS deviations observed in Fig. 5.3.

In the case of the $N = 100$ droplet, P_L exceeds P_c at low T, and the droplet enters the region of the bulk EOS associated with the high density liquid (HDL); see Fig. 5.8. For the $N = 100$ droplet, ρ_c is comparable to ρ_s, and both are close to the bulk HDL density [Fig. 5.8b]. The signature of an inverted density profile is also weak for $N = 100$ [Fig. 5.6a]. For $P_L > P_c$, we thus find that the droplet behaviour changes suddenly to that of a simple liquid. In sum, our results demonstrate that the droplet density profile correlates well to the bulk regime of the LLPT explored by the droplet: As $T \to T_c$, an inverted density profile indicates a droplet for which $P_L < P_c$, while a monotonic density profile suggests that $P_L > P_c$.

The large radial density change observed in our droplets at low T is perhaps suggestive of nanoscale phase separation in which a LDL-like core is wetted by a HDL-like surface layer. Fig. 5.8b shows that ρ_c and ρ_s grow farther apart as T decreases for all droplets having $P_L < P_c$. The values of ρ_s are consistent with the range expected

for HDL, while ρ_c is lower, and approaches LDL-like values when the droplet is large enough. Certainly, intrinsic surface effects play a large role in determining our density profiles: A droplet with a low-density RTN in the core will have a disrupted RTN, and therefore higher density, near the interface with the vapour. Independent of surface effects, the LLPT of TIP4P/2005 also promotes the appearance of distinct high and low density regions near the critical conditions. These two effects are mutually reinforcing, and it is likely that both contribute to the large density variations in our low T nanodroplets.

A bulk response function such as K_T, which quantifies volume fluctuations, diverges at the critical point of a LLPT. To test for a similar effect in our nanodroplets, we use the fluctuations of the Voronoi volumes for a subsystem of molecules inside our droplet cores to define a quantity K_T^s which is analogous to K_T (see Methods). As shown in Fig. 5.9, we observe a growing maximum in K_T^s along isotherms at $T = 200$ and 180 K, the same T for which strong deviations emerge between the nanodroplet and bulk EOS. This behaviour confirms that the interiors of our coldest droplets exhibit effects directly associated with the approaching LLPT in TIP4P/2005. Experiments have recently provided strong evidence of a K_T maximum in supercooled water, both for water enclosed in micrometer quartz inclusions [34], and for unsupported microdroplets [17]. Our results show that this effect may also be observable in much smaller nanodroplets, which allow even deeper supercooling, and which access higher P closer to the estimated critical conditions of the LLPT proposed for real water.

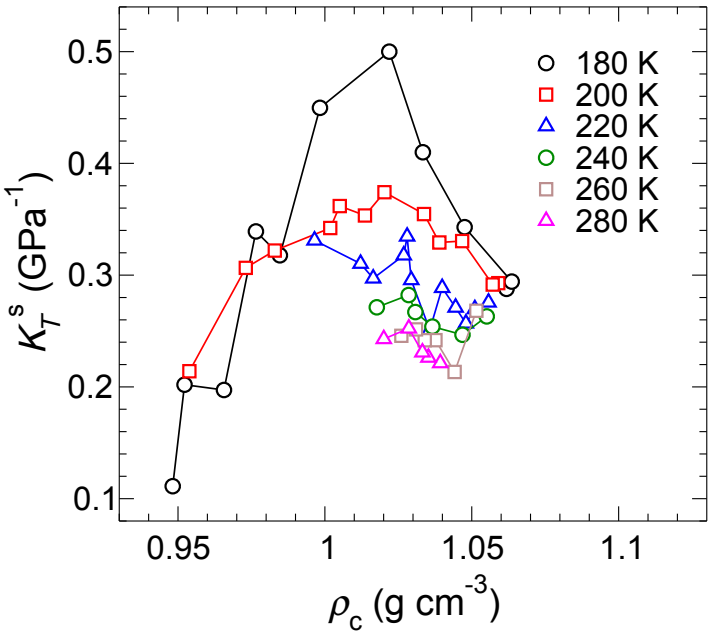

Figure 5.9: Isothermal compressibility of the nanodroplet core. Isotherms of K_T^s versus ρ_c for $200 \leq N \leq 2880$.

5.4 Discussion

It is a central goal of nanoscience to determine the scale at which macroscopic behaviour first emerges. Our results show that bulk-like liquid properties, including the density maximum, can be observed using water nanodroplets as small as several hundred molecules. We also demonstrate that by varying N, the interiors of water nanodroplets explore a remarkably wide range of both density and pressure. This range is large enough to encompass and to reproduce the pattern of thermodynamic anomalies that occurs in bulk water for $T \geq 220$ K, including precursors of the proposed LLPT. Indeed, we have shown that simply measuring the nanodroplet size R as a function of N and T is a viable approach for revealing the qualitative signatures of these anomalies.

For $T \leq 200$ K, we observe dramatic departures from bulk-like behaviour, which arise as T approaches T_c for the LLPT of TIP4P/2005. It is well understood that

the discontinuities at a bulk phase transition are strongly rounded and shifted by finite-size effects in small systems [35]. Explicit surface effects in nanoscale systems also induce deviations from bulk behavior. These two effects are intertwined in our system, and together they generate the complex evolution of nanodroplet properties that we observe as T decreases. Disentangling the relative contributions of finite-size and surface effects is challenging. For example, consider the ρ_c data shown in Fig. 5.5. In the bulk liquid, isobars of the density will decrease more sharply with decreasing T as $P \to P_c$. Although our smaller nanodrolets access higher P, the variation of ρ_c does not sharpen. Finite-size effects are at least partially responsible, since we know that the phase transition exists in our model bulk system, but we also know that ρ_c does not reach the bulk value at low T and small N because of the influence of the dense surface layer, as discussed above. Further work to quantify how finite-size and surface effects combine to produce the novel phenomena observed here would be valuable, for example, to better understand the unusual shape of our density profiles at low T.

Despite these complexities, our results establish the pattern of nanodroplet behaviour that occurs in a water-like system that exhibits a bulk LLPT. The key features of this behaviour are the deviation of nanodroplet properties from the bulk as $T \to T_c$, and the emergence of a large and inverted gradient in the droplet density profile when $P_L < P_c$. These observations have the potential to assist in understanding many systems where water nanodroplets play a central role. For example, for aerosols involved in cloud formation [6], the average position and chemical activity of a solute molecule within a water nanodroplet may be strongly influenced by the changes in the pressure and the density profile that we observe on cooling [36, 37]. Regarding the ongoing efforts to clarify the behaviour of deeply supercooled water, experiments increasingly exploit small water droplets, from the microscale [16, 17, 18]

to the nanoscale [11, 7, 28]. We confirm here that cold water nanodroplets both resist crystallization and generate sufficient Laplace pressure to directly access the region of the proposed LLPT. Furthermore, our results suggest specific ways to use nanodroplets to help locate a possible LLPT. For example, an experimental probe sensitive to the droplet density profile, or to the volume fluctuations of the droplet core, could identify droplets that have entered the critical regime, from which an estimate of T_c and P_c might be obtained.

5.5 Methods

5.5.1 Computer simulations

We simulate liquid water nanodroplets of size $N = 100$ to 2880 molecules. The molecules interact via the TIP4P/2005 water pair potential [19]. We use Gromacs v4.6.1 [20] to carry out our molecular dynamics (MD) simulations. The equations of motion are integrated using the leap-frog algorithm, with a time step of 2 fs. We carry out simulations in the fixed-(N, V, T) ensemble, where N is the total number of molecules in the simulation cell, and V is the volume of the cell. We hold the temperature constant using a Nosé-Hoover thermostat with a time constant of 0.1 ps. Our droplets are located in a cubic simulation cell, with periodic boundary conditions, of various sizes $V = L^3$, as listed in Supplementary Tables 5.1- 5.3. The intermolecular interaction is set to zero for molecules separated by more than $L/2$. We choose L large enough relative to the size of the droplet to avoid any direct interaction between the water droplet and its periodic images. Consequently, all molecules within a nanodroplet interact directly, without cut-offs or approximations for long-range electrostatic interactions.

Individual molecules occasionally escape from the surface of the droplet and con-

tribute to a vapour phase in equilibrium with the droplet. We choose L small enough so that the average number of molecules in the vapour phase is never more than $0.004N$ (see Supplementary Tables 5.1- 5.3). The vapour pressure in our simulations is always much smaller than the size of the error in our estimates for $P_{\rm L}$, and so we consider the vapour pressure to be zero. We note that because of the presence of the vapour phase, and our droplet definition (see below), the average number of molecules in a nanodroplet $N_{\rm d}$ may differ from the number of molecules in the system N. However, as stated above the difference is always less than $0.004N$, and for $T \leq 220$ K we find no difference. Having distinguished here between the definitions of N and $N_{\rm d}$, we note that to calculate the values of ρ_R presented in Fig. 5.2, we use $\rho_R = 3mN_{\rm d}/4\pi R^3$. When labelling data in our figures, we use the N value for the run from which the data are obtained.

For $N = 1440$ and 2880, we create initial configurations by placing N molecules at random within the simulation cell, and then running for long enough so that the molecules condense into a single droplet. Initial configurations for other values of N are obtained from our $N = 1440$ configurations by deleting molecules from the surface until the desired N is reached.

We conduct two types of run to evaluate the equilibrium properties of our droplets: conventional "single long runs" (SLR), and "swarm relaxation" runs [21]. We use SLRs for droplet sizes N = 100, 200, 360, 776, 1100, 1440, and 2880; see Supplementary Tables 5.1- 5.2. In each SLR, the system comes into equilibrium during the first phase of the run, followed by a production phase from which equilibrium configurations are harvested. The relaxation time τ (defined below) is evaluated from the production phase. In each SLR, our equilibration phase is at least 10τ long, and is never less than 100 ns. The length of the production phase of our runs is never less than 46τ, and is typically between $10^2\tau$ and $10^3\tau$.

For droplet sizes $N = 205$, 301, 405, 512, 614, and 729 we use the "swarm relaxation" method, described in detail in Ref. [21]. The initial configurations for these choices of N are obtained from a SLR configuration for $N = 2880$ by deleting molecules from the surface until the desired N is reached. We then run each new configuration for 350 ns at 200 K to generate a starting configuration for our swarm relaxation runs. For our swarm relaxations runs at 220 K, M different initial configurations are generated by randomizing the velocities of the starting configuration according to a Maxwell-Boltzmann distribution appropriate for $T = 220$ K. We use $M = 250$ or 1000, as documented in Supplementary Table 5.3. We then conduct an ensemble of M independent runs (a "swarm"), and monitor the average behaviour of the swarm over time to determine when the runs have attained equilibrium. Swarm relaxation runs at 200 K (180 K) are initiated using the M final configurations from the 220 K (200 K) runs. We evaluate the relaxation time $\tau_{\rm s}$ of each swarm ensemble from the autocorrelation function of the system potential energy. As shown in Ref. [21], swarm runs of length $10\tau_{\rm s}$ are sufficient for reaching equilibrium. Supplementary Table 5.3 shows that the run time $t_{\rm run}$ for each of our swarm runs significantly exceeds this threshold. To estimate equilibrium properties, we carry out an ensemble average over the final M configurations of each swarm run.

5.5.2 Droplet definition

We define the droplet as the largest cluster of water molecules in our system. A molecule belongs to a cluster if its distance to any molecule in the cluster is less than 0.35 nm [40].

5.5.3 Relaxation times

To determine the structural relaxation time τ of the droplets in our SLRs, we use the method of Refs. [41, 42]. We evaluate the bond correlation function $\phi(t)$, which characterizes the likelihood that a bond present at time $t = 0$ remains unbroken at time t:

$$\phi(t) = \left\langle \frac{1}{N_{\mathrm{B}}(0)} \sum_{i<j} n_{ij}(t)\, n_{ij}(0) \right\rangle . \tag{5.1}$$

Here, $n_{ij}(t) = 1$ for all t up to the time that the bond between molecules i and j breaks for the first time. After the bond breaks, $n_{ij}(t) = 0$ for all time, even if the bond later reforms. Molecules i and j are considered bonded if the distance between their O atoms $r_{ij} \leq 0.32$ nm. $N_{\mathrm{B}}(0)$ is the number of bonds at $t = 0$. The average in Eq. 5.1 is taken over multiple choices of the time origin $t = 0$.

In all cases, we find that $\phi(t)$ decays to zero on a time scale much shorter than the length our SLRs. This behaviour confirms that all of our nanodroplets are equilibrium liquid droplets, and not glassy solids. We define τ as the time such that $\phi(\tau) = e^{-1}$. We define the number of independent configurations in each of our SLR simulations as $N_\tau = t_{\mathrm{run}}/\tau$, where t_{run} is the total length of the production phase of a SLR. The values of τ and N_τ for each of our SLRs are listed in Supplementary Tables 5.1- 5.2.

5.5.4 Testing for crystal formation

To determine if crystalline ice forms in our liquid nanodroplets, we use the procedure developed by Frenkel and coworkers [43, 44] to identify clusters of crystal-like molecules, based on quantifying the local bond order using spherical harmonics [45]. The specific procedure we use to identify ice-like clusters is the same as that described in Ref. [46]. We monitor n_{max}, the size of the largest ice-like cluster in the droplet, as a function of time during our SLR simulations. The largest value of n_{max} encountered

in all of our SLR simulations is 12, observed in our $N = 1100$ droplet at 180 K. In the same run, the average value of $n_{\max}$ is 1.4. All such ice-like clusters appear only as transients, and dissipate on a time scale comparable to τ. These observations confirm that our droplets remain in the liquid phase on the time scale of our simulations.

5.5.5 Stability of liquid nanodroplets at low T.

The coexistence temperature for the bulk liquid and ice Ih phases of TIP4P/2005 is 252 K at ambient P, and decreases to 230 K at $P = 200$ MPa [19]. To estimate the minimum T at which we observe a thermodynamically stable liquid droplet, we prepare approximately spherical nanocrystallites of ice Ih of size $N = 360$ and 776. We run each of these nanocrystallites for 4 ns at $T = 180$, 200, 220, 240 and 260 K. During each run we monitor $n_{\max}$, the size of the largest crystalline cluster as a function of time t, using the definition of $n_{\max}$ described in Ref. [46]. As shown in Supplementary Fig. 5.15, our $N = 360$ system completely melts within 4 ns for $T \geq 200$ K, and our $N = 776$ system melts within 4 ns for $T \geq 220$ K. This behaviour demonstrates that liquid nanodroplets of these sizes are thermodynamically stable below the melting temperature for the bulk liquid phase.

5.5.6 Droplet radius

To quantify the droplet radius, we model the droplet as an ellipsoid with uniform density [47, 48]. We first compute the moment of inertia tensor $\mathbf{I}$ from the position vector $\mathbf{r}_i$ for the centre of mass of each molecule i in the droplet, relative to the droplet centre of mass. The elements of $\mathbf{I}$ are given by,

$$I_{jk} = m \sum_{i=1}^{N_{\mathrm{d}}} \left(r_i^2 \, \delta_{jk} - r_{ij} \, r_{ik} \right), \tag{5.2}$$

where $r_i = |\mathbf{r}_i|$; r_{ij} is the j^{th} component (x, y or z) of $\mathbf{r}_i$; and δ_{jk} is the Kronecker delta. The eigenvalues of $\mathbf{I}$ (I_{xx}, I_{yy} and I_{zz}) are related to the lengths of the principal axes (a, b and c) of the ellipsoid via the relations: $5I_{zz} = mN_{\rm d}(a^2+b^2)$; $5I_{xx} = mN_{\rm d}(b^2+c^2)$; and $5I_{yy} = mN_{\rm d}(a^2+c^2)$. We then define the droplet radius as $R = (abc)^{1/3}$. The values of R reported here are averages over the ensemble of droplet configurations generated for each N and T. We note that the qualitative pattern of behaviour observed in Fig. 5.2 does not change if we define R instead as the radius of gyration.

5.5.7 Voronoi volumes and isothermal compressibility

To evaluate the volumes of the Voronoi cells around the O atoms in our nanodroplet configurations, we use the "Voro++" software described in Ref. [49].

To define a quantity similar to K_T in our droplet cores, we exploit the dependence of K_T on the volume fluctuations in a fixed-(N,P,T) ensemble: $K_T = \langle \delta V^2 \rangle / \langle V \rangle kT$, where $\langle \delta V^2 \rangle$ is the variance of the system volume V [50]. We define a fixed-(N,P,T) subsystem within the droplet core by selecting from each configuration the 40 molecules that are closest to the droplet centre of mass. We choose 40 molecules because this is approximately the number of molecules within the core region of our $N = 200$ droplets, allowing us to consider a subsystem of fixed size throughout the range $200 \leq N \leq 2880$. We define the volume of the subsystem $\mathcal{V}_{\rm s}$ as the sum of the Voronoi volumes of these 40 molecules, and thereby define $K_T^{\rm s} = \langle \delta \mathcal{V}_{\rm s}^2 \rangle / \langle \mathcal{V}_{\rm s} \rangle kT$. Fig. 5.9 plots our results for $K_T^{\rm s}$ along isotherms for $N \geq 200$ as a function of $\rho_{\rm c}$.

5.5.8 Surface region of density profiles

To define the portion of $\rho_{\rm v}(r)$ associated with the droplet surface, we first model our data for $\rho_{\rm v}(r)$ by fitting to,

$$\rho_{\rm fit}(r) \;=\; \frac{\rho_0}{2}\left[\tanh\left(\frac{r-r_0}{\sigma_0}\right)+1\right], \tag{5.3}$$

where ρ_0, r_0 and σ_0 are fit parameters. To conduct this fit, we ignore data for $r <$ 0.2 nm, to avoid the larger error in $\rho_{\rm v}(r)$ at small r; see Supplementary Fig. 5.11. We define the surface region of $\rho_{\rm v}(r)$ as the region $r > r_0 - 0.6$ nm, and $\rho_{\rm s}$ as the maximum value of $\rho_{\rm v}(r)$ in the surface region. The density difference between the droplet surface and the core, $\rho_{\rm s} - \rho_{\rm c}$, is plotted in Fig. 5.6a.

5.5.9 Laplace pressure

To find the Laplace pressure $P_{\rm L}$, we first evaluate $P_{\rm N}$ and $P_{\rm T}$, the normal and tangential components of the configurational contribution to the pressure as a function of r within our droplets. We use the approach presented in Ref. [31], modified to suit the case of a rigid molecular model of water as described in Ref. [23]. As illustrated in Fig. 5.7a and Supplementary Fig. 5.12, we find in all cases that $P_{\rm N}$ and $P_{\rm T}$ differ, and display a prominent minimum, near the droplet surface. For smaller r, $P_{\rm N}$ and $P_{\rm T}$ become approximately equal within the error of our calculations. In a bulk liquid, the pressure tensor is isotropic, and so we identify the region inside the droplet where $P_{\rm N} \simeq P_{\rm T}$ as a bulk-like region in which the average total pressure is the Laplace pressure $P_{\rm L}$. The total pressure is given by,

$$P_{\rm tot} = \frac{1}{3}P_{\rm N} + \frac{2}{3}P_{\rm T} + \rho_{\rm o}kT, \tag{5.4}$$

where k is Boltzmann's constant. To evaluate P_{L}, we average P_{tot} from $r = 0$ to $r = R_L$, where R_L is the radius at which P_{N} and P_{T} first cross as r decreases below the surface region where the minima in P_{N} and P_{T} occur.

5.5.10 Error estimates

All error bars presented in our figures represent $\pm\sigma/\sqrt{N_{\mathrm{s}}}$, where σ is the standard deviation of the measured quantity, and N_{s} is the number of independent configurations averaged over. For our SLRs, we use $N_{\mathrm{s}} = N_\tau$. For our swarm runs, we use $N_{\mathrm{s}} = M$.

5.5.11 Data availability

The data that support the findings of this study are available from the authors on reasonable request.

Bibliography

[1] Baker, M. Cloud microphysics and climate. *Science* **276**, 1072-1078 (1997).

[2] Kulmala, M. How Particles Nucleate and Grow. *Science* **302**, 1000 (2003).

[3] Klemperer, W. & Vaida, V. Molecular complexes in close and far away. *Proc. Nat. Acad. Sci.* **103**, 10584-10588 (2006).

[4] Ahadi, E. & Konermann, L. Surface Charge of Electrosprayed Water Nanodroplets: A Molecular Dynamics Study. *J. Am. Chem. Soc.* **132**, 11270-11277 (2010).

[5] Wilhelmsen, O., et al. Coherent description of transport across the water interface: From nanodroplets to climate models. *Phys. Rev. E* **93**, 032801 (2016)

[6] Kulmala, M., et al. Formation and growth rates of ultrafine atmospheric particles: a review of observations. *J. Aerosol Science* **35**, 143-176 (2004).

[7] Manka, A., Pathak, H., Tanimura, T., Wolk, J., Strey, R. & Wyslouzil, B. Freezing water in no-man's land. *Phys. Chem. Chem. Phys.* **14**, 4505-4516 (2012).

[8] Pan, D., Liu, L.-M., Slater, B., Michaelides, A. & Wang, E. Melting the Ice: On the Relation between Melting Temperature and Size for Nanoscale Ice Crystals. *ACS Nano* **5**, 4562-4569 (2011).

[9] Debenedetti, P.G. *Metastable Liquids. Concepts and Principles* (Princeton University Press, Princeton, NJ, 1996).

[10] Caupin, F. Escaping the no man's land: Recent experiments on metastable liquid water. *J. Non-Cryst. Solids* **407**, 441-448 (2015).

[11] Huang, J. and Bartell, L.S. Kinetics of homogeneous nucleation in the freezing of large water clusters, *J. Phys. Chem.* **99**, 3924-3931 (1995).

[12] Debenedetti, P.G. Supercooled and glassy water. *J. Phys. Condens. Matter.* **15**, R1669-R1726 (2003).

[13] Poole, P.H., Sciortino, F., Essmann, U. & Stanley, H.E. Phase behaviour of metastable water. *Nature* **360**, 324-328 (1992).

[14] Gallo, P., et al. Water: A Tale of Two Liquids. *Chem. Rev.* **116**, 7463-7500 (2016).

[15] Mason, B. J. The supercooling and nucleation of water. *Adv. Phys.* **7**, 221-234 (1958).

[16] Sellberg, J.A. et al. Ultrafast X-ray probing of water structure below the homogeneous ice nucleation temperature. *Nature* **510**, 381-384 (2014).

[17] Kim, K.H. et al. Maxima in the thermodynamic response and correlation functions of deeply supercooled water. *Science* **358**, 1589-1593 (2017).

[18] Goy, C. et al. Shrinking of Rapidly Evaporating Water Microdroplets Reveals their Extreme Supercooling. *Phys. Rev. Lett.* **120**, 015501(2018).

[19] Li, T., Donadio, D. & Galli, G. Ice nucleation at the nanoscale probes no man's land of water. *Nat. Commun.* **4**, 1887 (2013).

[20] Malek, S.M.A., Sciortino, F., Poole, P.H. & Saika-Voivod, I. Evaluating the Laplace pressure of water nanodroplets from simulations. *J. Phys.: Condens. Matter* **30**, 144005 (2018).

[21] Biddle, J.W. et. al. Two-structure thermodynamics for the TIP4P/2005 model of water covering supercooled and deeply stretched regions. *J. Chem. Phys.* **146**, 034502 (2017).

[22] Buch, V., Bauerecker, S., Devlin, J.P., Buck, U. & Kazimirski, J. Solid water clusters in the size range of tens-thousands of H_2O: a combined computational/spectroscopic outlook. *Int. Rev. Phys. Chem.* **23**, 375-433 (2004).

[23] Hock, C., et al. Calorimetric Observation of the Melting of Free Water Nanoparticles at Cryogenic Temperatures. *Phys. Rev. Lett.* **103**, 073401 (2009).

[24] Pradzynski, C.C., Forck, R.M., Zeuch, T., Slavicek, P. & Buck, U. A fully size-resolved perspective on the crystallization of water clusters. *Science* **337**, 1529-1532 (2012).

[25] Johnston, J.C. & Molinero V. Crystallization, Melting, and Structure of Water Nanoparticles at Atmospherically Relevant Temperatures. *J. Am. Chem. Soc.* **134**, 6650-6659 (2012).

[26] Bhabhe, A., Pathak, H., & Wyslouzil, B.E. Freezing of Heavy Water (D2O) Nanodroplets. *J. Phys. Chem. A* **117**, 5472-5482 (2013).

[27] Factorovich, M.H., Molinero, V. & Scherlis, D.A. Vapor Pressure of Water Nanodroplets. *J. Am. Chem. Soc.* **136**, 4508-4514 (2014).

[28] Amaya, A.J. & Wyslouzil, B.E. Ice nucleation rates near $\sim$ 225 K. *J. Chem. Phys.* **148**, 084501 (2018).

[29] Nandi, P.K., Burnham, C.J., Futera, Z. & English, N.J. Ice-Amorphization of Supercooled Water Nanodroplets in No Man's Land. *ACS Earth Space Chem.* **1**, 187-196 (2017).

[30] Abascal, J.L.F & Vega, C. A general purpose model for the condensed phases of water: TIP4P/2005. *J. Chem. Phys.* **123**, 234505 (2005).

[31] Ikeshoji, T., Hafskjold, B. & Furuholt, H. Molecular-level calculation scheme for pressure in inhomogeneous systems of flat and spherical layers. *Mol. Simul.* **29**, 101 (2003).

[32] Vega, C. & de Miguel, E. Surface tension of the most popular models of water by using the test-area simulation method. *J. Chem. Phys* **126**, 154707 (2007).

[33] Bruot, N. & Caupin, F. Curvature Dependence of the Liquid-Vapor Surface Tension beyond the Tolman Approximation. *Phys. Rev. Lett.* **116**, 056102 (2016).

[34] Holten, V., Qiu, C., Guillerm, E., Wilke, M., Ricka, J., Frenz, M., & Caupin, F. Compressibility Anomalies in Stretched Water and Their Interplay with Density Anomalies. *J. Phys. Chem. Lett.* **8**, 5519-5522 (2017).

[35] Binder, K. Monte Carlo methods for the study of phase transitions and phase equilibria. *Eur. Phys. J. B* **64**, 307-314 (2008).

[36] Wyslouzil, B.E., Wilemski, G., Strey, R., Heath, C.H. & Dieregsweiler, U. Experimental evidence for internal structure in aqueous-organic nanodroplets. *Phys. Chem. Chem. Phys.* **8**, 54-57 (2006).

[37] Ma, X., Chakraborty, P., Henz, B.J. & Zachariah, M.R. Molecular dynamic simulation of dicarboxylic acid coated aqueous aerosol: structure and processing of water vapor. *Phys. Chem. Chem. Phys.* **13**, 9374-9384 (2011).

[38] Hess, B., Kutzner, D., van der Spoel, D. & Lindahl, E. GROMACS 4: Algorithms for highly efficient, load balanced, and scalable molecular simulation. *J. Chem. Theory Comput.* **4**, 435-447 (2008).

[39] Malek, S.M.A., Bowles, R.K., Saika-Voivod, I., Sciortino, F. & Poole, P.H. "Swarm relaxation": Equilibrating a large ensemble of computer simulations. *Eur. Phys. J. E* **40**, 98 (2017).

[40] Sevick, E.M., Monson, P.A. & Ottino, J.M. Monte Carlo calculations of cluster statistics in continuum models of composite morphology. *J. Chem. Phys.* **88**, 1198-1206 (1988).

[41] Starr, F.W, Nielsen, J.K. & Stanley, H.E. Fast and Slow Dynamics of Hydrogen Bonds in Liquid Water. *Phys. Rev. Lett.* **82**, 2294-2297 (1999).

[42] Sciortino, F., Tartaglia, P. & Zaccarelli, E. One-Dimensional Cluster Growth and Branching Gels in Colloidal Systems with Short-Range Depletion Attraction and Screened Electrostatic Repulsion. *J. Phys. Chem. B* **109**, 21942-21953 (2005).

[43] Auer S. & Frenkel, D. Numerical prediction of absolute crystallization rates in hard-sphere colloids. *J. Chem. Phys.* **120**, 3015-3029 (2004).

[44] Valeriani, C., Sanz, E. & Frenkel, D. Rate of homogeneous crystal nucleation in molten NaCl. *J. Chem. Phys.* **122**, 194501 (2005).

[45] Steinhardt, P.J., Nelson, D.R. & Ronchetti, M. Bond-orientational order in liquids and glasses. *Phys. Rev. B* **28**, 784-805 (2001).

[46] Buhariwalla, C.R.C., Bowles, R.K., Saika-Voivod, I., Sciortino, F. & Poole, P.H. Free energy of formation of small ice nuclei near the Widom line in simulations of supercooled water. *Eur. Phys. J. E* **38**, 39 (2015).

[47] Trudu, F., Donadio, D. & Parrinello, M. Freezing of a Lennard-Jones Fluid: From Nucleation to Spinodal Regime. *Phys. Rev. Lett.* **97**, 105701 (2006).

[48] Wang, H., Gould, H. & Klein, W. Homogeneous and heterogeneous nucleation of Lennard-Jones liquids. *Phys. Rev. E* **76**, 031604 (2007).

[49] Rycroft, C.H. Voro++: A three-dimensional Voronoi cell library in C++. *Chaos* **19**, 041111 (2009).

[50] Allen, M.P. & Tildesley, D.J. *Computer Simulation of Liquids*, Clarendon Press, Oxford (1987).

5.6 Acknowledgements

I.S.-V. and P.H.P. thank NSERC for support. Computational resources were provided by ACEnet and Compute Canada. We thank R.K. Bowles and F. Sciortino for helpful discussions.

5.7 Author contributions

All authors contributed equally to planning the study, interpreting the results, and preparing the manuscript. S.M.A.M. carried out all simulations and data analysis.

5.8 Competing financial interests

The authors declare no competing financial or non-financial interests.

5.9 Additional information

Correspondence and requests for materials should be addressed to I.S.-V. (saika@mun.ca).

5.10 Supplementary information

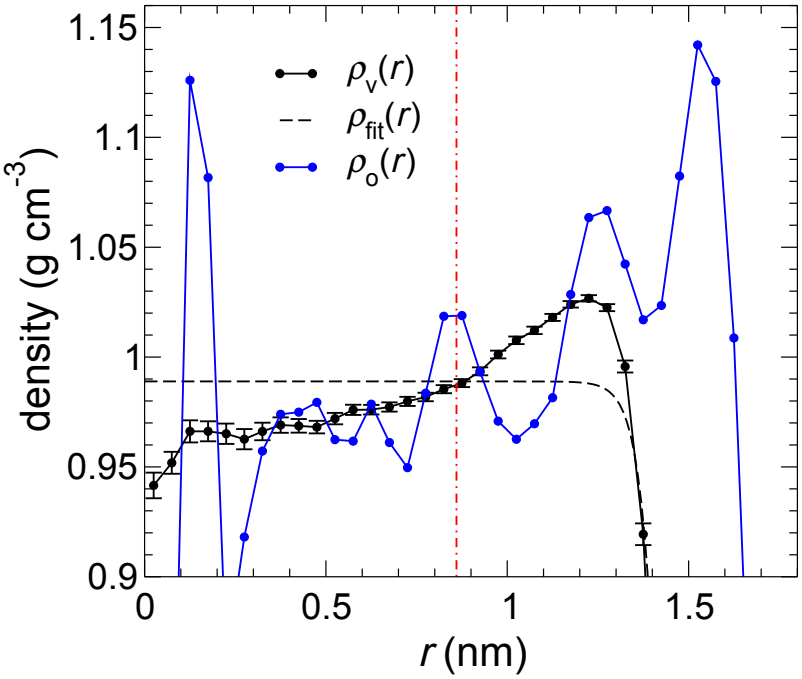

Figure 5.10: Comparison of density profile definitions. Here we plot $\rho_o(r)$ and $\rho_v(r)$ for water nanodroplets with $N = 776$ at $T = 180$ K. The black dashed line is a fit to $\rho_v(r)$ using Eq. 3. The surface region of the droplet, as defined in Methods, is the region where r is larger than that of the red dot-dashed line. Error bars represent one standard deviation of the mean.

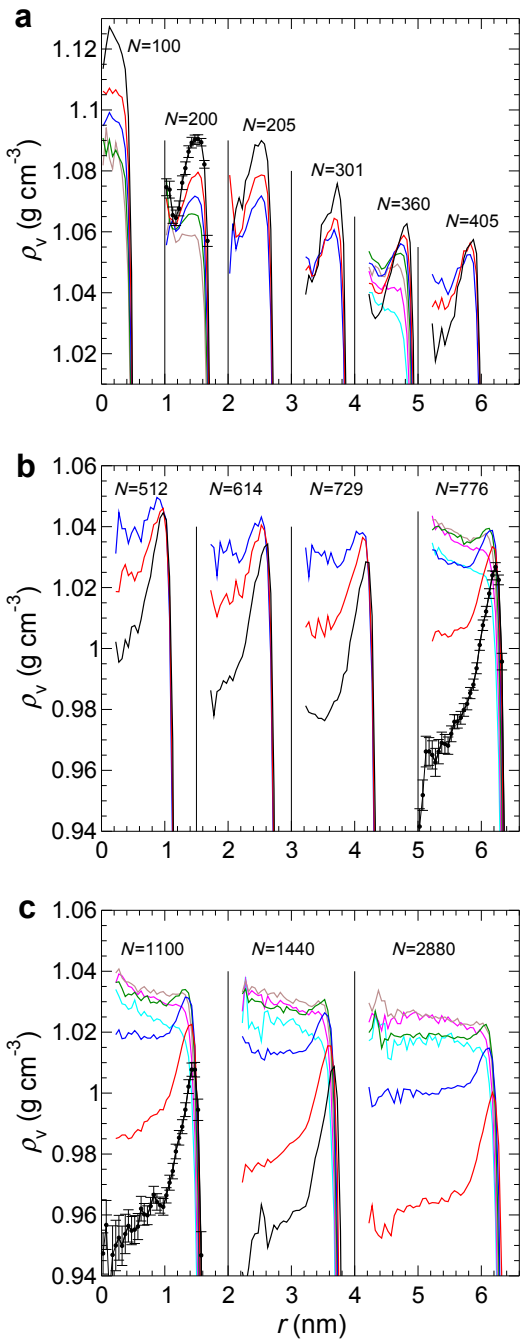

Figure 5.11: Nanodroplet density profiles. Here we show $\rho_{\mathrm{v}}(r)$ for a wide range of N and T. In each panel, one representative curve is shown with error bars. For curves without error bars, data for $r < 0.2$ nm are not plotted for $N \geq 301$, since the error at small r is typically large. Line colours indicate T: 180 K (black), 200 K (red), 220 K (blue), 240 K (green), 260 K (brown), 280 K (magenta), 300 K (cyan). To facilitate comparison, for most data sets the origin of r has been shifted by an integer multiple of 0.5 nm, as indicated by the thin vertical lines. Error bars represent one standard deviation of the mean.

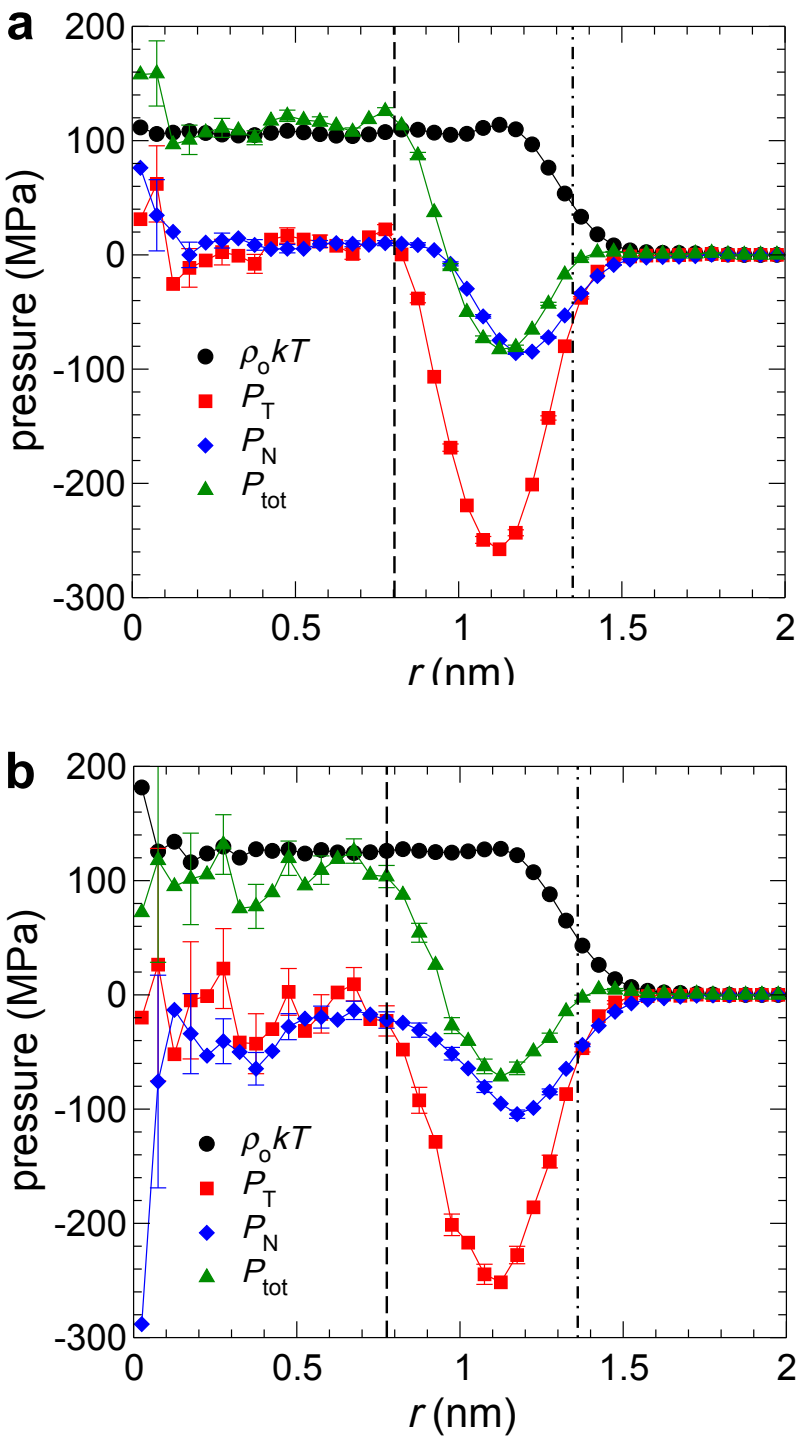

Figure 5.12: Contributions to the pressure inside water nanodroplets. **a** $N = 360$ and $T = 220$ K. **b** $N = 360$ and $T = 260$ K. Vertical lines identify $r = R_L$ (dashed) and $r = R$ (dot-dashed). Error bars represent one standard deviation of the mean.

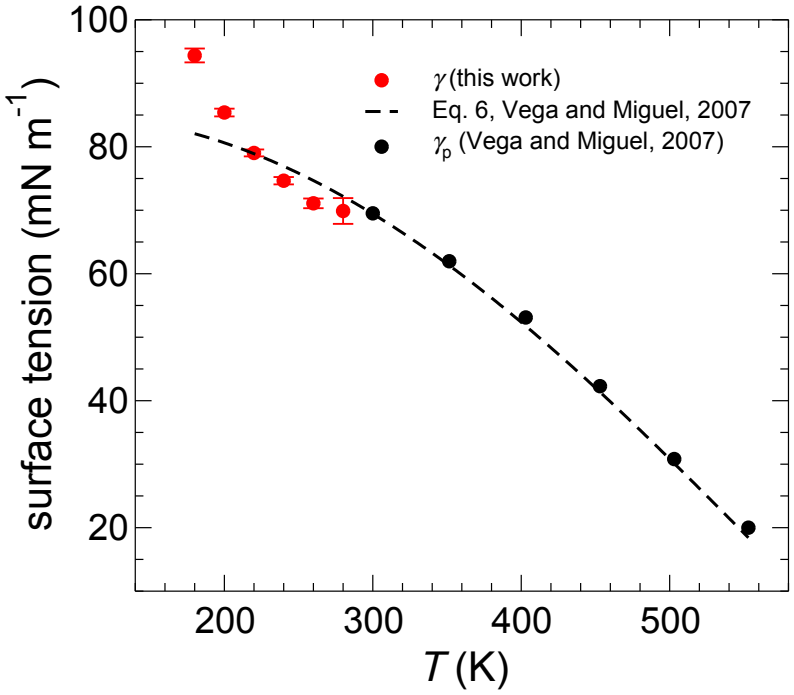

Figure 5.13: Variation of the nanodroplet surface tension with temperature. We compare our results for γ with results for the surface tension γ_p of a planar liquid-vapour interface for TIP4P/2005, taken from Ref. 31. Error bars represent one standard deviation of the mean.

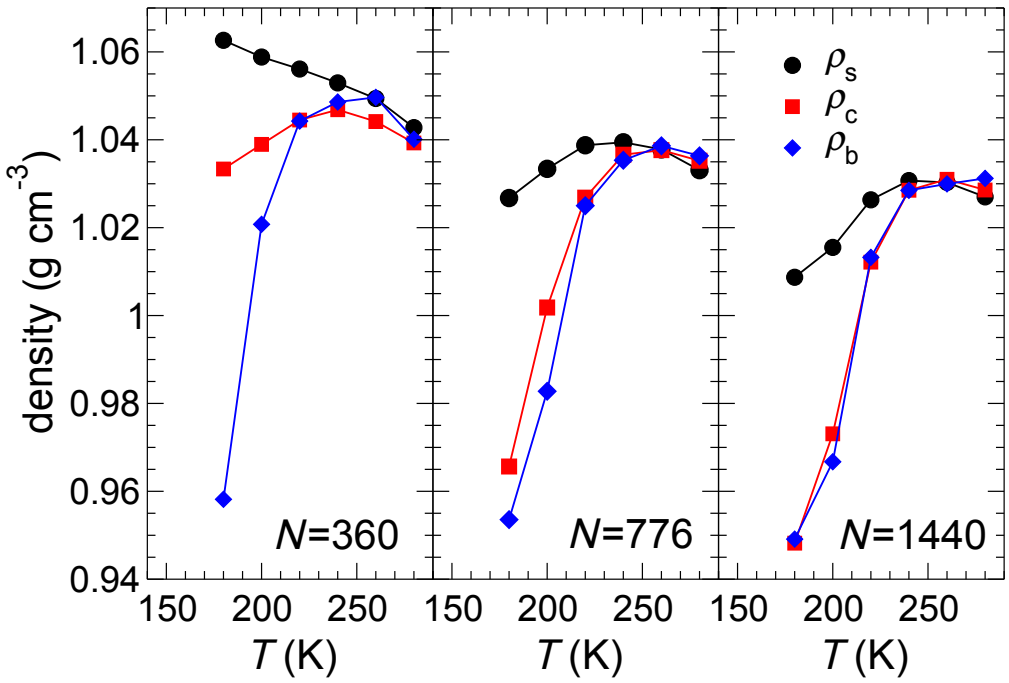

Figure 5.14: Variation with temperature of characteristic densities for nanodroplets. Here we show the dependence of ρ_s, ρ_c and ρ_b on T for droplets of various sizes N. For $N = 1440$, the droplet is large enough for the core density ρ_c to reach the bulk density ρ_b, despite the growing difference between ρ_b and the surface density ρ_s at low T. For smaller droplets, ρ_c does not reach ρ_b at low T.

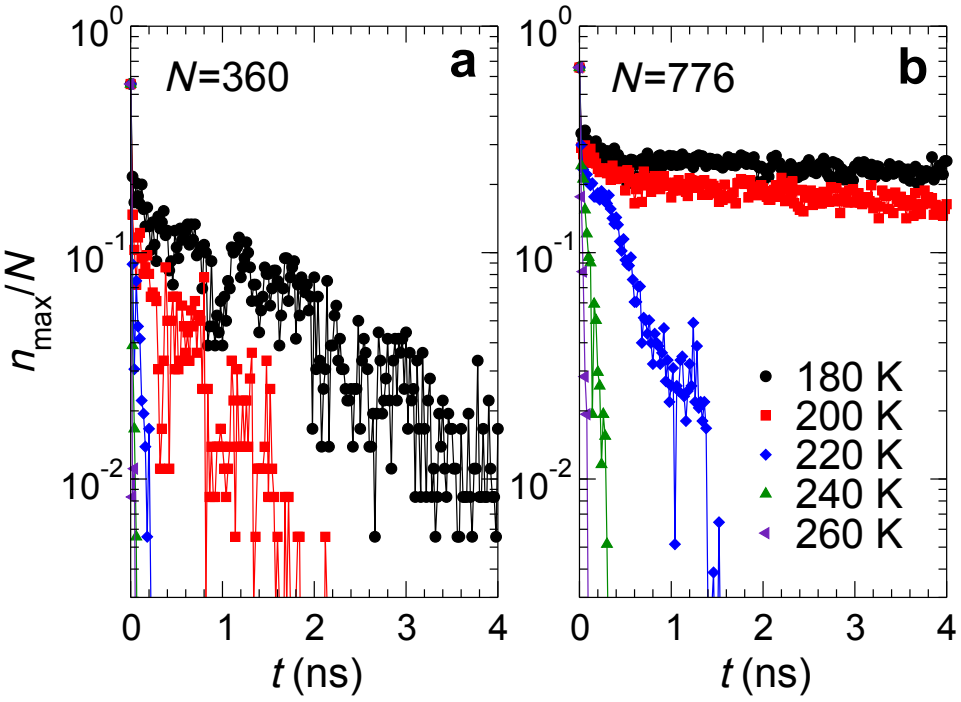

Figure 5.15: Melting of nanocrystals. Variation of $n_{\max}/N$ with time t during melting of ice nanocrystals of size N at various T.

N	L (nm)	T (K)	N_{d}	τ (ns)	N_τ
100	10	180	100.00	2.4	1167
		200	100.00	0.4	3499
		220	100.00	0.8	2892
		240	99.97	0.8	2995
		260	99.75	0.8	3499
200	10	180	200.00	3.2	864
		200	200.00	0.8	3335
		220	200.00	0.8	3453
		240	199.97	0.8	3452
		260	199.82	0.8	3500
360	10	180	360.00	2.4	392
		200	360.00	0.4	5921
		220	360.00	0.2	12113
		240	360.00	0.2	9837
		260	359.94	0.2	1397
		280	359.71	0.2	876
		290	359.56	0.2	10287
		300	359.26	0.2	10247
776	15	180	776.00	6.8	166
		200	776.00	0.8	954
		220	776.00	0.4	1917
		240	775.87	0.4	1808
		260	775.84	0.4	1921
		280	775.32	0.4	1977
		290	774.84	0.4	2040
		300	773.85	0.4	2009

Table 5.1: Run parameters and relaxation time scales for our SLR nanodroplet simulations. Symbols are as defined in the Methods section. For each N, as T increases, τ becomes equal to the time interval between successive stored configurations during each SLR. Since we cannot measure values of τ smaller than this time interval, such a τ value represents an upper bound on the actual value of τ.

N	L (nm)	T (K)	N_{d}	τ (ns)	N_τ
1100	20	180	1100.00	12.8	46
		200	1100.00	1.6	288
		220	1100.00	0.8	562
		240	1099.75	0.8	577
		260	1099.53	0.8	603
		280	1098.32	0.8	594
		290	1097.01	0.8	556
		300	1095.13	0.8	579
1440	20	180	1440.00	8.6	49
		200	1440.00	1.0	360
		220	1439.98	0.2	1588
		240	1439.77	0.2	1502
		260	1439.74	0.2	1153
		280	1438.64	0.2	829
		290	1437.84	0.2	261
		300	1434.91	0.2	205
2880	20	200	2880.00	1.4	74
		220	2880.00	0.2	490
		240	2879.97	0.2	464
		260	2879.89	0.2	443
		280	2879.44	0.2	240
		290	2878.71	0.2	320
		300	2877.31	0.2	148

Table 5.2: Run parameters and relaxation time scales for our SLR nanodroplet simulations. Symbols are as defined in the Methods section. For each N, as T increases, τ becomes equal to the time interval between successive stored configurations during each SLR. Since we cannot measure values of τ smaller than this time interval, such a τ value represents an upper bound on the actual value of τ.

N	L (nm)	T (K)	N_{d}	τ_{s} (ns)	M	t_{run} (ns)
205	8.29	180	205.00	1.63	1000	79.70
		200	205.00	0.14	1000	15.94
		220	205.00	0.05	1000	15.94
301	9.42	180	301.00	1.02	250	15.80
		200	301.00	0.12	250	7.90
		220	301.00	0.04	1000	7.90
405	10.40	180	405.00	1.91	250	63.13
		200	405.00	0.13	1000	7.89
		220	405.00	0.02	1000	7.89
512	11.25	180	512.00	2.36	250	47.71
		200	512.00	0.19	250	7.95
		220	512.00	0.04	250	7.95
614	11.95	180	614.00	2.55	250	96.73
		200	614.00	0.23	250	8.06
		220	614.00	0.05	250	8.06
729	12.65	180	729.00	4.19	250	99.63
		200	729.00	0.28	250	8.27
		220	729.00	0.06	250	8.27

Table 5.3: Run parameters and relaxation time scales for nanodroplet simulations carried out using the swarm relaxation method. Symbols are as defined in the Methods section.

Chapter 6

Surface tension of deeply supercooled TIP4P/2005 water nanodroplets using direct evaluation of the pressure tensor

6.1 Abstract

We estimate the surface tension from direct calculations of the components of the microscopic pressure tensor in water nanodroplets modelled with the TIP4P/2005 potential. We study the validity of the Young-Laplace equation over a wide range of size, from 100 to 2880 molecules, and temperature T, from 300 K down to 180 K. Values of the planar surface tension γ_p are consistent with those of Vega and de Miguel [*J. Chem. Phys.* **126**, 154707 (2007)] down to the crossing of the Widom line at $T = 230\ K$ for ambient pressure. Below this temperature, there is an unexpected increase in γ_p. We can discern no T dependence of the Tolman length δ, but find

that the mechanical route to determining the surface tension yields a higher value of $\delta \approx 0.2-0.3$ nm compared to $\delta \approx 0.06$ nm obtained via the thermodynamic route. The mechanical route gives smaller values for the surface tension for highly curved droplet surfaces γ_s compared to the thermodynamic route, for which γ_s is consistent with results at 293 K from Lau *et al* [J. Phys. Chem. **142**, 114701 (2015)]. Assuming the validity of the thermodynamic route, for water nanodroplet radius as small as 1 nm, the curvature dependence of γ_s is small, and so γ_s can be approximated by γ_p to within approximately 15% at the lowest T. We also report on how local structure changes within the droplets. We find that a well structured random tetrahedral network forms at low T and larger sizes, and that droplet cores are bulk-like from a structural perspective.

6.2 Introduction

The essential role that water nanodroplets play in our lives motivates us to understand the physics inside them and the interplay between the core of small nanodroplets and their surface. Their presence in pivotal systems, such as climate [1, 2], biological applications [3], interstellar space [4], and numerous other systems [5], prompts us to comprehend their complex behaviour, such as their thermodynamic anomalies and nucleation processes. The surface tension plays an important role in water nanodroplet nucleation in the atmosphere. The vapour-liquid surface tension is crucial to determine the nucleation rate from the classical nucleation theory (CNT) [6, 7]. There is still an active debate on how the strong curvature of small condensed nanodroplets affects the surface tension.

Understanding the surface tension of planar surfaces has been a focus of study for many years. In contrast, the surface tension of curved surfaces has not been studied

as extensively as for planar surfaces. It has been accepted that the surface tension of curved surfaces deviates from that of planar surfaces. Laplace and Young [8, 9], through observation and analytical derivation, found the relation that bears their names, the Young-Laplace equation,

$$\Delta P = \frac{2\gamma_s}{R_s}, \tag{6.1}$$

where $\Delta P = P_l - P_v$, where P_l and P_v are the pressures of the two fluids in contact assuming the fluids are liquid and vapor, γ_s is the surface tension of the curved surface, and R_s is the radius of the surface of tension, where the surface tension acts. For relatively large droplets, R_s is simply the radius of the droplet. Once the interfacial width becomes significant compared to the size of droplet, the radius of the droplet is not uniquely defined.

For curved surfaces, like that of a droplet, Tolman derived an expression that shows how γ_s deviates from the planar surface tension, γ_p, as the droplet radius varies, and for which he introduced a curvature correction quantified by what is now termed the Tolman length δ [10],

$$\gamma_s = \frac{\gamma_p}{(1 + 2\delta/R_s)}. \tag{6.2}$$

The magnitude of δ is generally found to be 10-20% of the molecular diameter, while its sign is still under debate [11]. While modeling on the basis of classical density functional theory predicted negative δ, simulations estimated both negative and positive δ. Yan *et al* [12] performed MD simulations of argon nanoclusters of size ranging from 800 to 2000 particles at 78 K. They evaluated the pressure tensor and using the Young-Laplace equation, they concluded that δ is positive for Lennard-Jones (LJ) nanodroplets and negative for LJ vapor bubbles. However, Giessen and Blokhuis [11]

estimated a negative δ for LJ naodroplets. The same disagreement appears in water simulations. Leong and Wang [13] performed MD simulations using the BLYPSP-4F water potential on nanoscale droplets of sizes varying between 1.973 and 7.940 nm at $T = 298$ K. Using an empirical correlation between the pressure and density, they estimated $\delta = -0.048$ nm. The same negative sign for δ was obtained through measuring the free energy of mitosis in a study by Joswiak *et al* [14], while Lau *et al* [15] used a test-area method and obtained a positive δ. Therefore, it is clear that there is a controversy between studies on the surface tension and where it acts, even when the same water model is used.

The sign of δ determines whether γ_s decreases or increases with R_s. For a positive δ, γ_s decreases as R decreases. Moreover, δ relates the equimolar radius R_e and R_s [10],

$$\delta = R_e - R_s, \tag{6.3}$$

where R_e is the radius of a sphere that has a uniform density equal to that of the interior part of the droplet and that has the same number of molecules as the droplet. Since determining R_e is more straightforward than determining R_s, we can rewrite Eqs. 6.1 and 6.2 in terms of R_e,

$$\Delta P = \frac{2\gamma_p}{R_e}\left(\frac{1}{1+\delta/R_e}\right), \tag{6.4}$$

or in the form,

$$\frac{2}{\Delta P R_e} = \frac{1}{\gamma_p}\left(1+\delta/R_e\right), \tag{6.5}$$

and

$$\gamma_s = \gamma_p \frac{R_e - \delta}{R_e + \delta}. \tag{6.6}$$

Aside from the Laplace equation, Rowlinson and Widom proposed a model to de-

rive γ_s from the tangential and normal components of the pressure tensor as functions of the radial distance r from the centre of mass of a droplet, $P_T(r)$ and $P_N(r)$ [16]. The model assumes two homogeneous fluid phases, with homogeneous pressures P^α and P^β far from the interface, and an inhomogeneous interface between them. Under the model assumption that the surface tension acts at a single value of $r = R_s$, the mechanical requirements for static equilibrium, i.e. force and torque balance, yield,

$$\gamma_s = \int_0^\infty \left(\frac{r}{R_s}\right) \left[P^{\alpha,\beta}(r;R_s) - P_T(r)\right] dr, \tag{6.7}$$

$$= \int_0^\infty \left(\frac{r}{R_s}\right)^2 \left[P^{\alpha,\beta}(r;R_s) - P_T(r)\right] dr, \tag{6.8}$$

where $P^{\alpha,\beta}(r;R_s)$ is P^α for $r < R_s$ and P^β for $r > R_s$. These equations in turn give an expression for R_s,

$$R_s = \frac{\int_0^\infty r^2 \left[P^{\alpha,\beta}(r;R_s) - P_T(r)\right] dr}{\int_0^\infty r \left[P^{\alpha,\beta}(r;R_s) - P_T(r)\right] dr}. \tag{6.9}$$

With the assumption that the two phases are homogeneous, we can assume that $P^\alpha = P_l$ and $P^\beta = P_v$. Since $P^{\alpha,\beta}(r;R_s)$ depends on the location of R_s, Eq. 6.9 can be evaluated numerically.

From the condition of mechanical stability, $\nabla \cdot \mathbf{P} = 0$, it can be proved that,

$$\int_0^\infty r^2 \left[P^{\alpha,\beta}(r;R_s) - P_N(r)\right] dr = 0, \tag{6.10}$$

and hence γ_s can be obtained using the $P_N(r)$ component of the pressure in Eqs. 6.7

and 6.8, yielding,

$$\gamma_s = \int_0^\infty \left(\frac{r}{R_s}\right) [P_N(r) - P_T(r)]\, dr, \tag{6.11}$$

$$= \int_0^\infty \left(\frac{r}{R_s}\right)^2 [P_N(r) - P_T(r)]\, dr, \tag{6.12}$$

and

$$R_s = \frac{\int_0^\infty r^2 [P_N(r) - P_T(r)]\, dr}{\int_0^\infty r [P_N(r) - P_T(r)]\, dr}. \tag{6.13}$$

Moreover, through the mechanical stability, the surface tension at any radius R inside the the droplet shows a minimum at the surface of tension R_s with value of γ_s,

$$\gamma(R) = \int_0^\infty \left(\frac{r}{R}\right)^2 \left[P^{\alpha,\beta}(r; R_s) - P_T(r)\right] dr. \tag{6.14}$$

However, we can also find γ_s while avoiding the need for R_s by combining Eqs. 6.1 and 6.12,

$$\gamma_s^3 = \frac{(P_l - P_v)^2}{4} \int_0^\infty r^2 [P_N(r) - P_T(r)]\, dr \tag{6.15}$$

In this study, we use the TIP4P/2005 model to simulate water nanodroplets under a wide range of temperatures and sizes to compare the two methods of evaluating δ and γ_s. Following Tompson *et al* [17], we refer to Eqs. 6.1, 6.4, and 6.5 as the thermodynamic route, and to Eqs. 6.7- 6.15 as the mechanical route. This should help in understanding the physics of surface tension of curved surfaces.

The paper is organized as follows. In Section 6.3, we provide details of our simulations. In Section 6.4, we report our results. We present a discussion and our conclusions in Section 6.5.

6.3 Simulations

We recently studied the thermodynamic and structural properties of simulated water nanodroplets ranging in size from N =100 to 2880 molecules, over a temperature T range of 180 to 300 K [18], with molecules interacting through the TIP4P/2005 model [19]. The same data set is used in the present study. We summarize the simulation details below for the reader's convenience.

We carry out the simulations in the canonical ensemble – constant N, volume V, and T. The droplets are located in a cubic box of side length L that increases with N and ranges from 10 to 20 nm. We ensure the box is large enough to avoid any direct interaction between the water droplet and its periodic images, and small enough to ensure that few molecules are in the vapour phase. We use a potential cutoff of $L/2$, ensuring that all molecules in the droplet interact without truncation of the potential. Occasionally, some molecules depart from the droplet surface into the vapour phase. Hence, we employ periodic boundary conditions to ensure that vapour molecules can return to the droplet in order to avoid complete evaporation. We use Gromacs v4.6.1 [20] to carry out our molecular dynamics (MD) simulations. We hold the temperature constant with the Nosé-Hoover thermostat with time constant 0.1 ps. The equations of motion are integrated with the leap-frog algorithm with a time step of 2 fs.

We set up two kinds of runs in this study: the conventional "single long runs" (SLR), and using a "swarm relaxation" method (SWRM) [21]. For droplet sizes $N = 100$, 200, 360, 776, 1100, 1440, and 2880, we use SLRs. For $N = 1440$ and 2880, we start our simulations by placing N molecules randomly within the simulation box, and run long enough for the molecules to condense into a single droplet. We harvest an equilibrated $N = 1440$ configuration, and progressively remove molecules from the droplet surface to obtain starting configurations for the other droplet sizes. The

slowest relaxation times are approximately 12 ns, and our longest post-equilibration simulations last 2.8 μs.

For droplet sizes $N = 205$, 301, 405, 512, 614, and 729, we use SWRM. To generate initial configurations for each of these droplet sizes, we first remove molecules from the surface of an equilibrated $N = 2880$ configuration to obtain the desired size. We first conduct SLRs for each size at $T = 200$ K for not less than 350 ns. We then take the last configuration of each run and randomize the velocities using the Maxwell-Boltzmann distribution at $T = 220$ K to generate M different configurations, which are used to initiate our swarm relaxation runs. We determine the relaxation time τ_s of each swarm ensemble from the potential energy autocorrelation function of the system. See Ref. [21] for details. The final equilibrated M configurations of each ensemble is then used to conduct ensembles at $T = 200$ K. Similarly, we take the final equilibrated M configurations of each ensemble at $T = 200$ K to start swarm ensembles at $T = 180$ K.

Additionally, we carry out simulations for bulk TIP4P/2005 with T varying from 300 to 180 K with 360 molecules with density varying approximately between 0.96 and 1.12 g/cm^3 using the protocols described in Ref. [22].

6.4 Results

6.4.1 Surface tension

The mechanical route to finding the surface tension of a droplet requires determining both $P_T(r)$ and $P_N(r)$. We compute kinetic and configurational contributions to the pressure inside our droplets; see Ref. [23] for details. Fig. 6.1 shows all contributions to the pressure. We define R_L such that the configurational contributions to the pressure, $\overline{P}_N$ and $\overline{P}_T$, are equal to each other within error for $r < R_L$ (dashed line in Fig. 6.1),

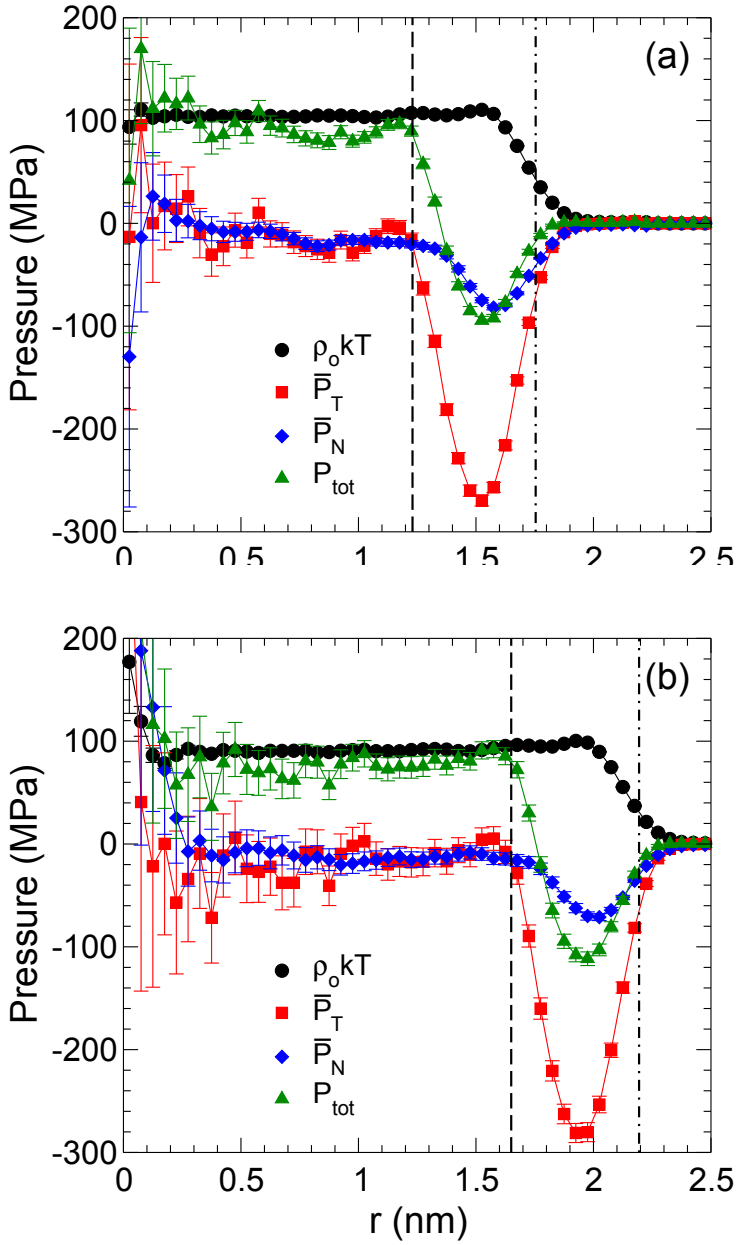

Figure 6.1: Contributions to the pressure inside water nanodroplets as a function of r, for (a) $N = 776$ and $T = 220$ K, and (b) $N = 1440$ and $T = 200$ K. Vertical lines identify $r = R_L$ (dashed) and $r = R_e$ (dot-dashed)

and they differ near the surface. To define the pressure in the interior of the droplets P_L, we average the total (isotropic) pressure $P_{tot}(r) = \overline{P}_N(r)/3 + 2\overline{P}_T(r)/3 + \rho_\circ(r)k_\mathrm{B}T$ over the spherical volume of radius R_L, where $\rho_\circ(r)$ is the local number density.

We also use the Young-Laplace equation in the form of Eq. 6.4 to determine γ_p and δ, and refer to this approach as the thermodynamic route [10]. We plot the isotherms of P_L as a function of R_e^{-1} in Fig. 6.2. The isotherms show that there is a significant pressure that naturally builds up in the interior of the droplets, and it can reach as high as 200 MPa for $R_e^{-1} \simeq 1.2$ nm^{-1} ($R_e \simeq 0.83$ nm).

In Fig. 6.2 we study the curvature correction to P_L as a function of R_e. Assuming $\delta = 0$, the fits in Fig. 6.2a using Eq. 6.1 show that there is no obvious curvature correction to the Young-Laplace equation. To see how small δ is in our range of droplet sizes, we fit P_L as a function of R_e^{-1} at each T with Eq. 6.4, as shown in Fig 6.2b. We report the value of δ as a function of T in Fig. 6.3, and can discern no dependence of δ on T. The average small and positive value of Tolman length $\bar{\delta} = 0.055$ nm explains the absence of strong curvature in Fig. 6.2.

To exclude the effect of the linear term in Eq. 6.4, we plot, in analogous form to Fig. 6.2b, $2/P_L R_e$ as a function of R_e in Fig 6.4. Since δ does not have an apparent dependence on T, we fit the isotherms in Fig. 6.4 to Eq. 6.5 assuming a single fitting parameter δ across all T. As shown in Fig. 6.4, this global fit reasonably describes all the isotherms, and gives a value of $\delta = 0.036$ nm that is similar to $\bar{\delta}$. The intercepts in Fig. 6.4 yield γ_p for each T, and indicate that γ_p decreases with T.

As discussed in Sec. 6.2, γ_p and δ can also be obtained using the mechanical route. To find γ_p and δ, we first evaluate γ_s using Eq. 6.8, where we set $P^\alpha = P_L$ for and $P^\beta = 0$ since the vapour pressure in our simulations is negligible. In Fig. 6.5a we show isotherms of γ_s as a function of R_s^{-1}, where R_s is obtained from Eq. 6.9. We see that γ_s decreases with increaing R_s^{-1} along isotherms, indicating that δ is positive. Fitting these isotherms with Eq. 6.2 yields curves with γ_p as intercepts. However, another way of evaluating γ_s is through Eq. 6.12. Isotherms of γ_s from Eq. 6.12 as a function of R_s^{-1}, where R_s^{-1} comes from Eq. 6.13, are shown in Fig. 6.5b. Although

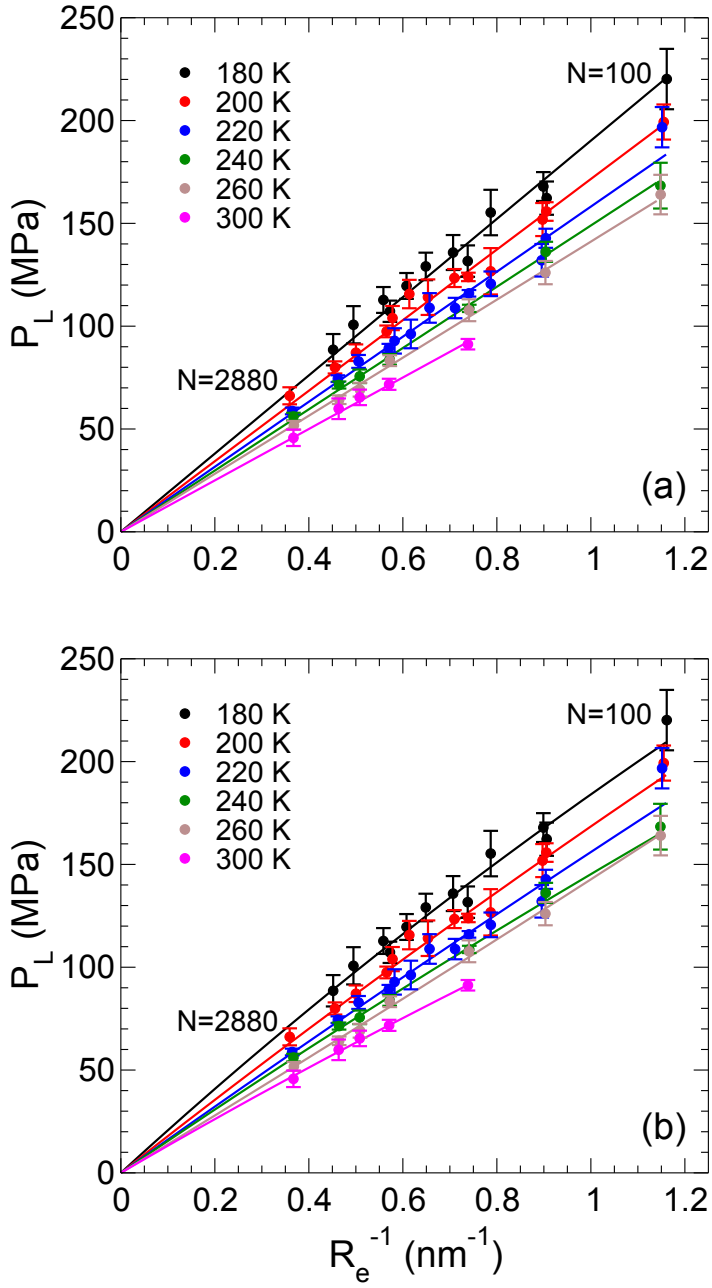

Figure 6.2: Isotherms of P_L as a function of R_e^{-1}. Along each isotherm, N decreases with R_e. (a) The straight lines are fits to Eq. 6.1, with assumption that $\delta = 0$. (b) The curves are two-parameter fits to Eq. 6.4.

the trend seems to indicate that γ_s decreases with R_s^{-1} using Eqs. 6.12 and 6.13, the noise resulting from subtracting $P_N(r)$ and $P_T(r)$ prevents useful fitting of γ_s. The solid curves shown in Fig. 6.5b are simply the fits taken from Fig. 6.5a, and show

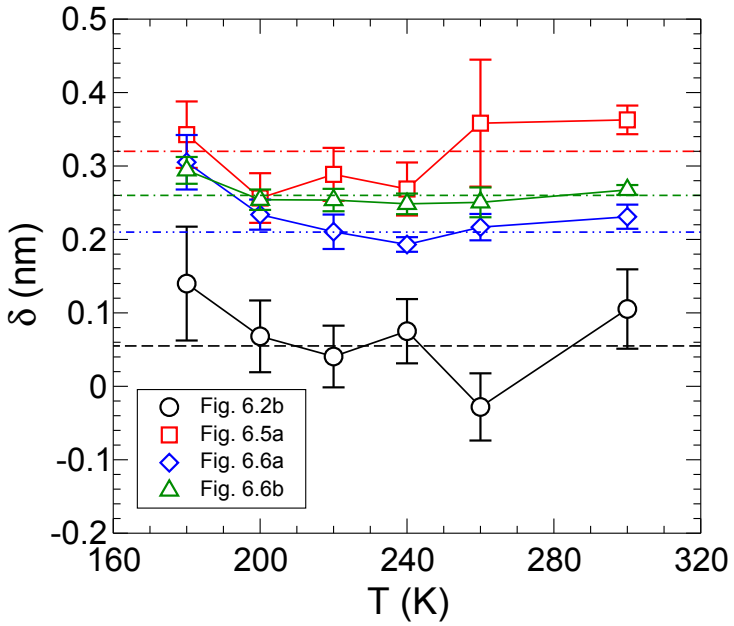

Figure 6.3: Tolman length δ as a function of T obtained from different means: fits of $P_L(R_e)$ to Eq. 6.4 shown in Fig. 6.2b (black circles); fits of $\gamma_s(R_s)$ to Eq. 6.2 shown in Fig. 6.5a (red squares) with average value of 0.32 ± 0.02 nm (dot-dashed); fits of $\gamma_s(R_s)$ to Eq. 6.2 shown in Fig. 6.6a (blue diamonds) with average value of 0.21 ± 0.01 nm (dot-dashed-dashed); and fits of $\gamma_s(R_e)$ to Eq. 6.6 shown in Fig. 6.6b with average value of 0.26 ± 0.005 nm (dot-dot-dashed).

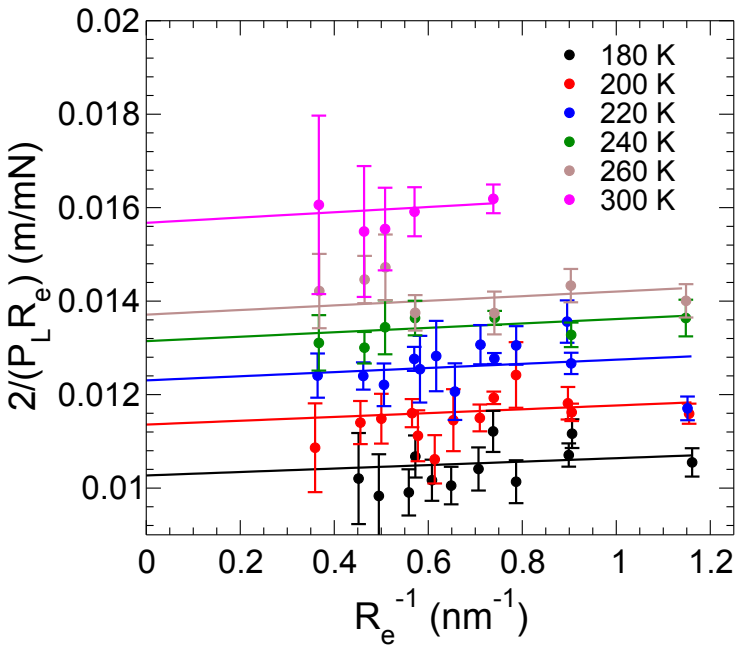

Figure 6.4: Isotherms of $2/(P_L R_e)$ as a function of R_e^{-1}. Along each isotherm, N decreases with R_e. The straight lines are fits to Eq. 6.5, where $\delta = 0.055$ nm is a global fit parameter.

a general consistency between using Eqs. 6.8 and 6.9, and using Eqs. 6.12 and 6.13, with the former set suffering from less statistical scatter.

Unlike both Eqs. 6.8 and 6.12, which require the determination of R_s to evaluate γ_s, Eq. 6.15 does not involve calculating R_s. We plot γ_s obtained from Eq. 6.15 as a function of R_s^{-1} in Fig. 6.6a. We choose R_s from Eq. 6.13 because γ_s in Eq. 6.15 is derived from Eq. 6.12. The absence of R_s in Eq. 6.15 seems to suppress the noise from $P_N(r)$. We again fit the isotherms in Fig. 6.6a to Eq. 6.2, and we find that the trends of the fits are similar to the trends in Fig. 6.5a.

To avoid any difficulty inherent in calculating R_s, another way of representing γ_s is as a function of R_e^{-1}, as shown in Fig. 6.6b. Regardless of which variant of the mechanical route is taken, we observe that γ_s decreases as R_e and R_s decrease, δ is positive with little evidence for a dependence on T, and γ_p decreases with T. The values of δ obtained from each variant of the mechanical route are shown for each T

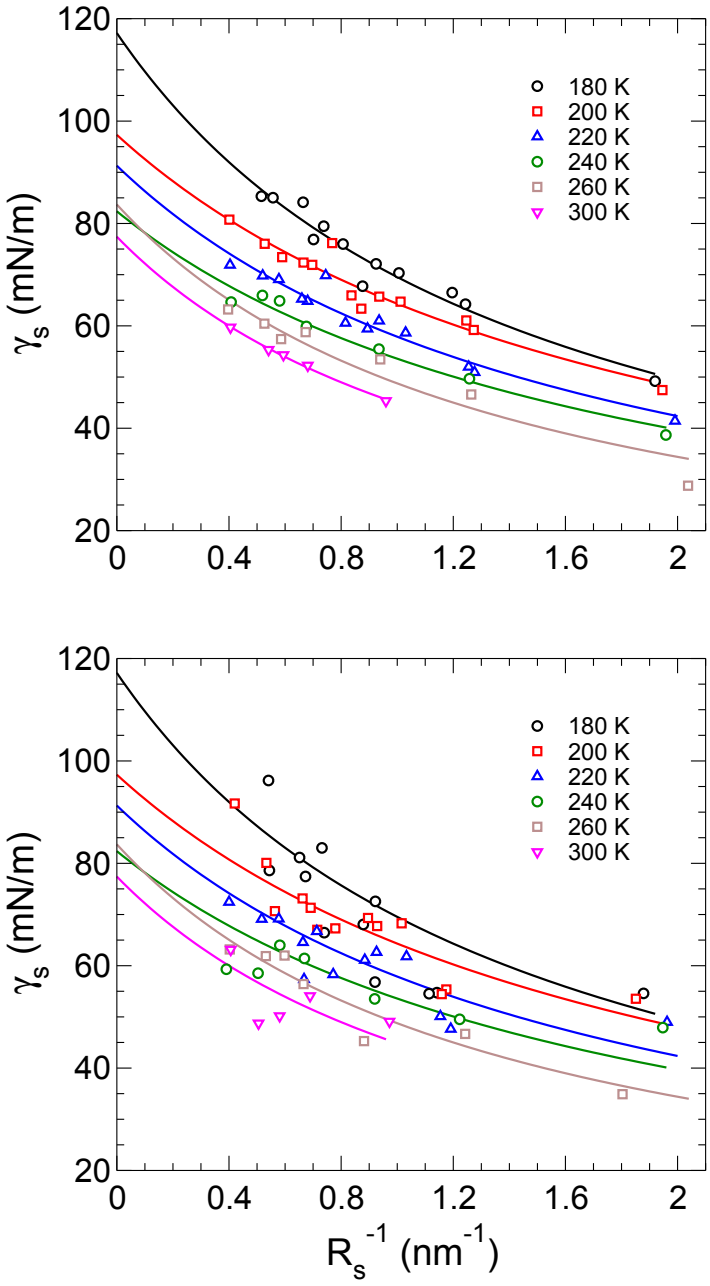

Figure 6.5: γ_s as a function of R_s^{-1}. (a) γ_s obtained from Eq. 6.8 (symbols), where curves are fits to Eq. 6.2. (b) γ_s obtained from Eq. 6.12 (symbols), where curves are replotted from panel (a). Curve intercepts equal γ_p, and steepness is proportional to δ.

in Fig. 6.3.

We show γ_p as obtained from the thermodynamic routes in Fig. 6.7a. Since δ

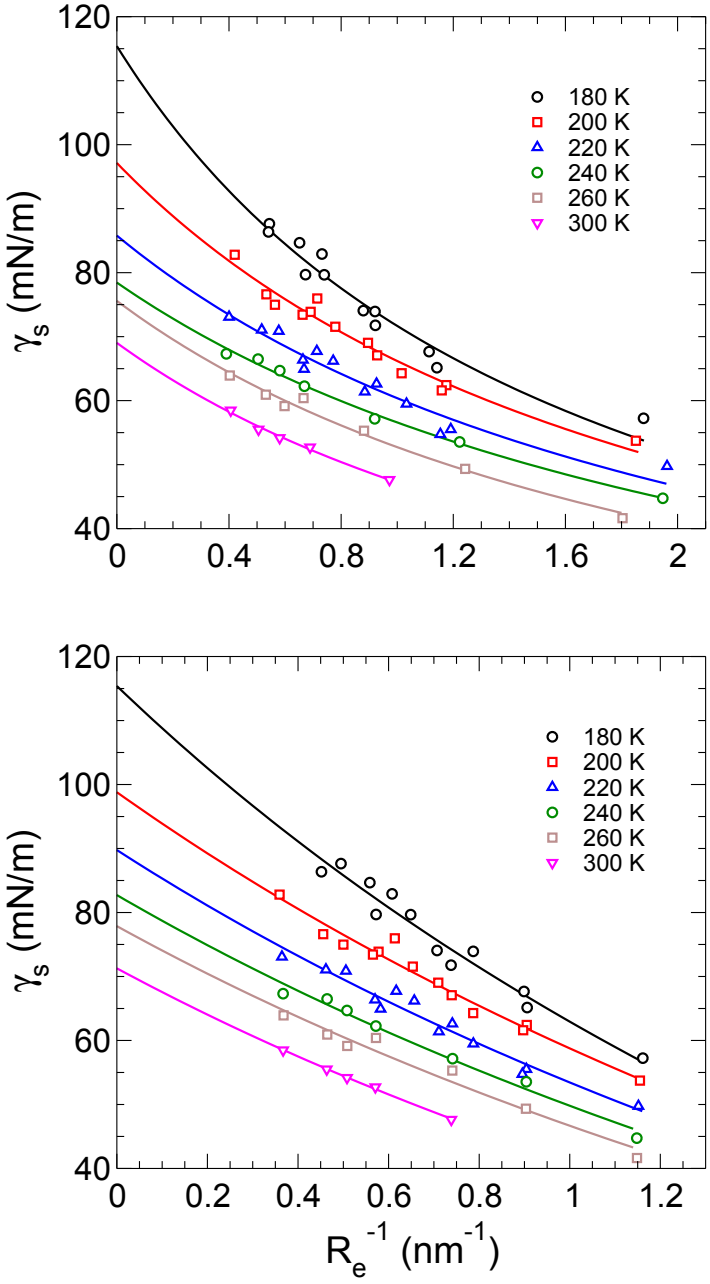

Figure 6.6: γ_s from Eq. 6.15 as a function of (a) R_s^{-1}, with fits to Eq. 6.2 (solid lines). (b) R_e^{-1}, with fits to Eq. 6.6 (solid lines). Curve intercepts equal γ_p, and steepness is proportional to δ.

is small, the thermodynamic route yields similar estimates of γ_p whether or not the curvature correction is considered down to $T = 220$ K. At $T = 180$ K the discrepancy between $\delta = 0$ and $\delta \neq 0$ appears to be outside of error, with the curvature-corrected

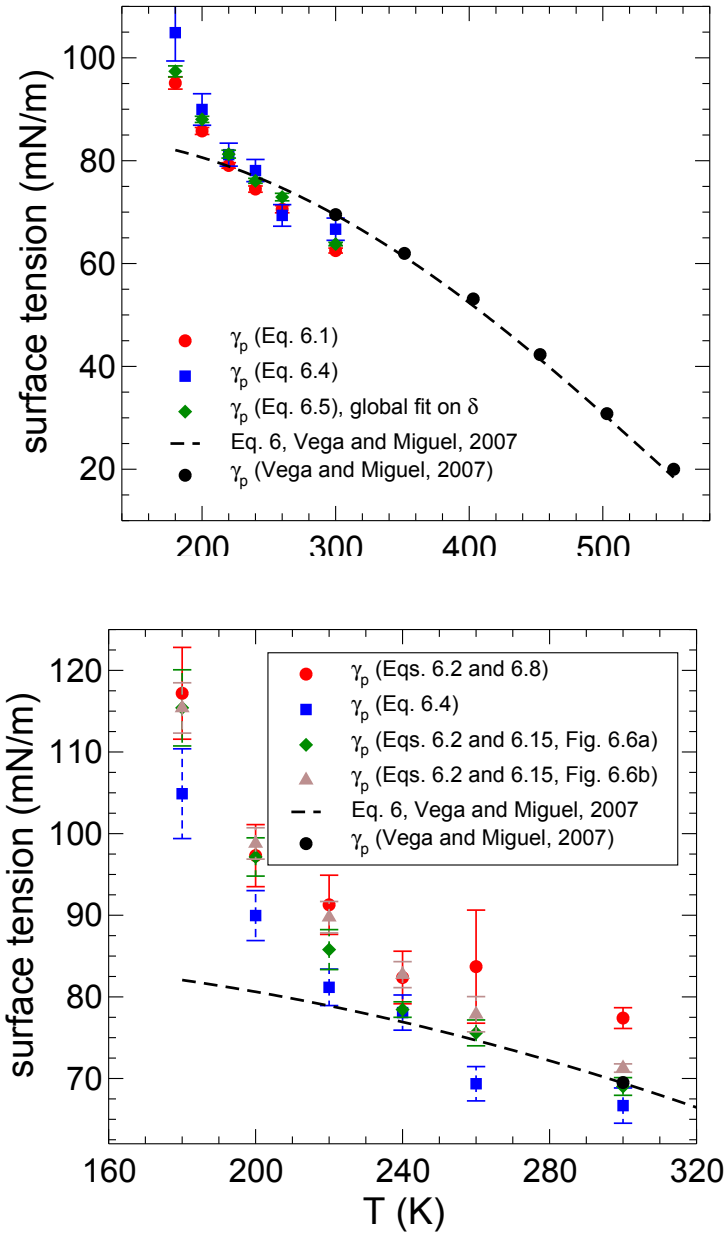

Figure 6.7: The variation of planar surface tension γ_p with T. (a) γ_p via the thermodynamic route obtained from the fits in Fig. 6.2a (red circles), Fig. 6.2b (blue squares), Fig. 6.4 (green diamonds). (b) γ_p via the mechanical route obtained from the fits in Fig. 6.5a (red circles), Fig. 6.2b (blue squares), Fig. 6.6a (green diamonds), and Fig. 6.6b (brown triangles).

result yielding a value of γ_p approximately 10% higher (blue squares versus red circles in Fig. 6.7a). For $T \geq 220$ K our estimates of γ_p are also consistent with the extrapolation down to low T of γ_p obtained using the test-area method, taken from Eq. 6 in the work of Vega and de Miguel [24].

For $T = 200$ and 180 K, there is a rapid increase in our estimation of γ_p in water compared to the extrapolation to low T. This change in trend may arise as a consequence of crossing the Widom line at $T = 230$ K along ambient pressure [25] as $R \to \infty$ and $N \to \infty$ ($P \simeq 0$). In the phase diagram, the Widom line is the locus of correlation length maxima, close to which lie loci of maxima in response functions, such as the isothermal compressibility. In this case, the rapid increase in γ_p below 220 K may be connected to the proposed liquid-liquid critical point (LLCP) [26]. Malek *et al* [18] also observed an emergence of complex radial density profiles at these temperatures, indicative of the formation of low density liquid (LDL) in the core.

In the case of the mechanical route, the planar surface tension as obtained from the fits in Fig. 6.5a is larger than when the thermodynamic route is taken, as shown in Fig. 6.7b, where the values obtained from these equations are systematically above both Vega and de Miguel's extrapolation [24] and γ_p as obtained from the fits in Fig. 6.2b. Interestingly, γ_p from the fits in Fig. 6.6a which use R_s from Eq. 6.13 is consistent with the thermodynamic route for $T \geq 220$ K and overlaps with Vega and de Miguel's extrapolation within error for $T \geq 240$ K, and is lower than γ_p from the fits in Fig. 6.6b. This shows that Eqs. 6.2 and 6.6 give different estimates of γ_p even if they are used to fit the same γ_s as obtained from Eq. 6.15, and perhaps the case for using Eq. 6.3 in the Tolman length (Eq. 6.2) requires closer inspection.

For another independent comparison, we show in Fig. 6.8 our results for γ_s as obtained from both thermodynamic and mechanical routes at $T = 300$ K with the values in Ref. [15] obtained using the test-area method at $T = 293$ K. We see that our

results for γ_s from the thermodynamic route are consistent with Laue *et al.* However, the mechanical route gives smaller values of γ_s. Smaller values of γ_s and R_s and larger values of δ for the mechanical route are also observed in nanodroplets interacting through the Lennard-Jones potential studied by Thompson *et al* [17].

To compare the difference in γ_s as obtained from the mechanical and thermodynamic routes, we plot in Fig. 6.9 isotherms of γ_s as a function of R_e. Fig. 6.9a shows a significant change in γ_s obtained from Eq. 6.15 as droplet size varies. For a change in the nanodroplet radius from 1 to 3 nm, there is a 50% increase in γ_s at $T = 180$ K, and 44% at $T = 300$ K. However, if we compare this with γ_s estimated from the thermodynamic route using δ from the fits in Fig. 6.2 and P_L values for all N and T, we see that the isotherms are almost flat for $T \geq 220$ K while there is only a %15 difference in γ_s across the droplet size range. We also can see that γ_s from the thermodynamic route is systematically larger than the mechanical route, which is once again consistent with Thompson *et al* [17].

6.4.2 Local structure ordering

Studying the ordering of the water molecules in the interior of the droplets and how it changes as we reach the surface is important to enhance our understanding of water at the nanoscale. To quantify the structure of the interior in our water nanodroplets, we calculate the distance $d_5(r)$ between a molecule located at a distance r from the centre of the droplet and its fifth nearest neighbouring molecule (using centres of mass when defining distances). A large value of $d_5(r)$ indicates that, at that radial distance from the centre of the droplet, molecules tend to be four-coordinated, i.e. that the local tetrahedral network is well formed. We show in Fig. 6.10a $d_5(r)$ over a wide range of N and T. We observe that $d_5(r)$ for droplet size $N = 100$ is small and stays rather constant. The absence of any change in $d_5(r)$ as we approach the surface indicates

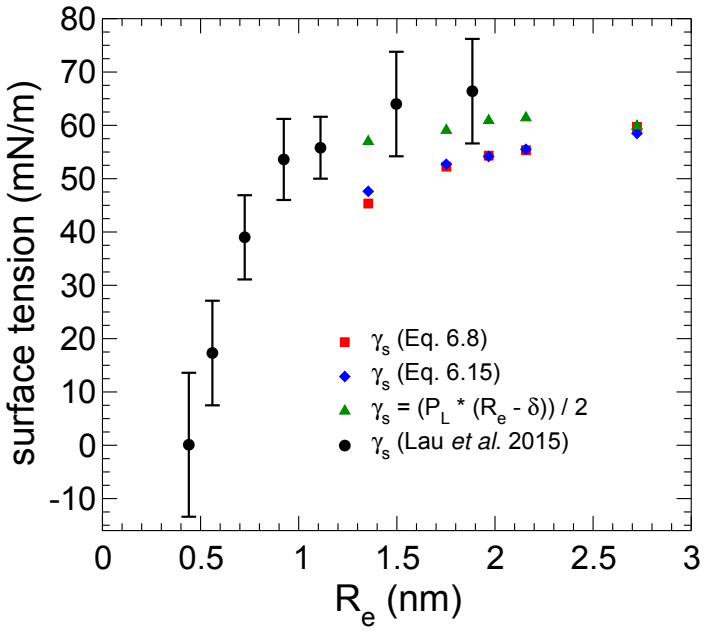

Figure 6.8: Surface tension of curvature γ_s as a function of R_e at $T = 300$ K from Eq. 6.8 (red squares), Eq. 6.15 (blue diamonds), using the two-parameter fit, $\delta = 0.105$ nm and $\gamma_p = 66.68$ mN/m from Fig. 6.2 (green triangles), and from Lau *et al.* [15] at $T = 293$ K (black circles).

a disturbance in the tetrahedral network in the whole droplet. The low value of d_5 indicates a collapse of the second neighbour shell around each molecule. This collapse is representative of the high density liquid (HDL) form of water. The overlap of the curves at different T for $N = 100$, suggests that droplets at this small size remain HDL-like both in the interior and at the surface regardless of how deeply we supercool them. As we increase the droplet size to $N = 360$, the profiles systematically shift to higher value of d_5 in the interior as we cool to 180 K. This change is a signature of a transition from HDL at high T to a low density liquid (LDL) at low T. However, for $T \leq 220$ K and $N = 360$ in Fig. 6.10a, there is a decrease in d_5 going from interior to surface, which indicates a disturbance of the tetrahedral network and an increase in density at the surface. For larger droplets, such as $N = 776$, we see similar behaviour as $N = 360$, but the transformation scans a wider range of d_5. Moreover, for $N = 776$

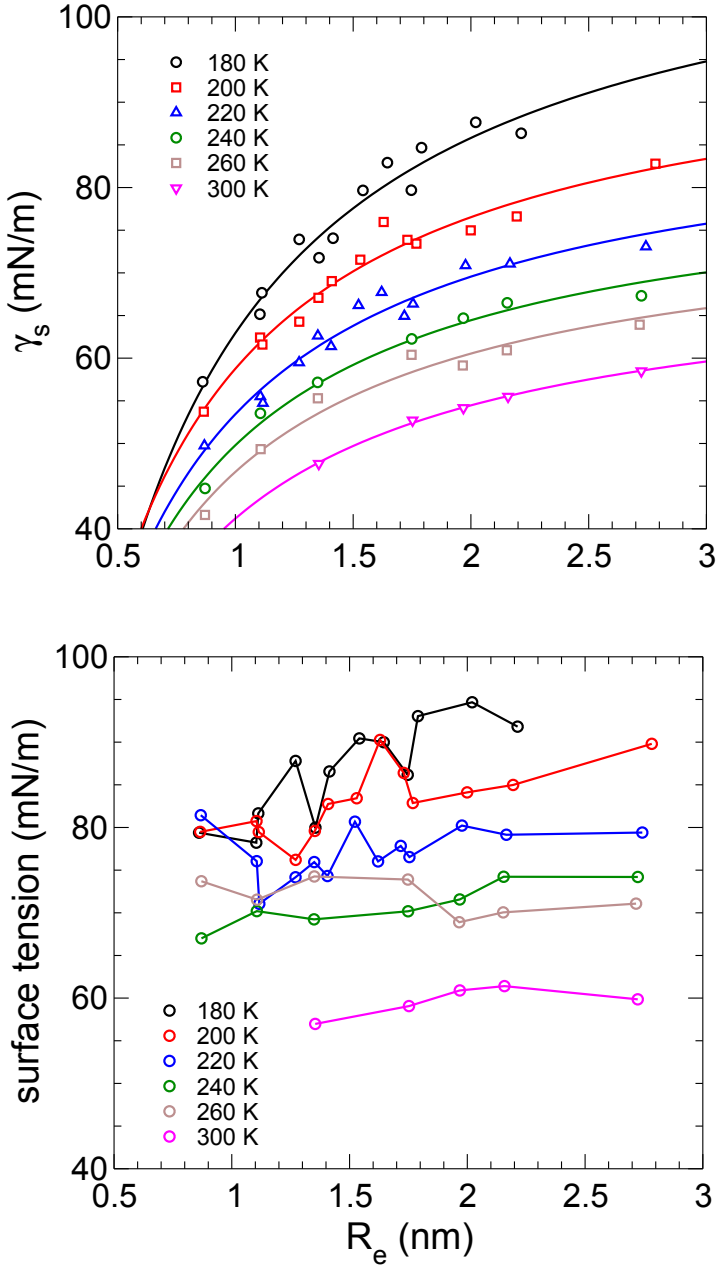

Figure 6.9: Isotherms of γ_s as a function of R_e. (a) γ_s obtained from mechanical route through Eq. 6.15 and fitted with Eq. 6.6. (b) Through the thermodynamic route, $\gamma_s = P_L\,(R_e - \delta)/2$.

at $T = 180$ K we see a monotonic decrease in d_5 as we approach the surface. This may reflect the emergence of structural transformation within the droplet. The same scenario presents itself for $N = 1440$. At $T = 180$ K, as N increases from 100 to 1440, d_5 in the interior monotonically increases. This indicates that as N increases, a better LDL forms in the interior of the droplets. The transformation from HDL to LDL in the interior may explain the change in behaviour in γ_p for $T \leq 200$ K in Fig. 6.7.

To further probe the ordering inside the nanodroplets, we compute the local tetrahedral order parameter [27],

$$q_i = 1 - \frac{3}{8} \sum_{j}^{3} \sum_{j=k+1}^{4} \left[\cos \psi_{jik} + \frac{1}{3} \right]^2 \tag{6.16}$$

where ψ_{jik} is the angle between the centre water molecule i and its nearest neighbour water molecules j and k. Using this definition, we define the average of the tetrahedral order parameter of water molecules at radius r from the droplet centre of mass as,

$$q_T(r) = \sum_i \frac{q_i \cdot \delta\left(r_i - r, \Delta r\right)}{n\left(r, \Delta r\right)} \tag{6.17}$$

$$n\left(r, \Delta r\right) = \sum_i \delta\left(r_i - r, \Delta r\right) \tag{6.18}$$

where $\delta\left(r, \Delta r\right) = 1$ for $|r| < \Delta r$ and zero otherwise, r_i is the distance of the oxygen atom of the i^{th} water molecule from the centre of mass of the droplet, and hence $n\left(r, \Delta r\right)$ is the number of molecules that have their oxygen atoms located within Δr of r.

We show how $q_T(r)$ changes in Fig. 6.10b. We see that q_T is low for $N = 100$ and it increases as we supercool the droplet. Similar behaviour appears for $N = 360$, 776,

and 1440. However, for $T = 200$ and 180 K, the increase in q_T upon increasing N becomes quite dramatic, supporting the suggestion that a better tetrahedral network forms as N increases. For $N = 1440$ at $T = 180$ K, the core reaches 90% of perfect tetrahedral order. The monotonic decrease in q_T for $N = 776$ and 1440 at $T = 180$ K is consistent with the decrease we observe in d_5.

To illustrate the structurally bulk-like character of droplet interiors, we plot d_5 and q_T as a function of density in Fig. 6.11. To compute the density, we define the density for droplet interiors as $\rho = m\langle \mathcal{N}/\mathcal{V} \rangle$, where $\mathcal{N}$ is the number of O atoms within a defined core radius $r_c = 0.5$ nm of the droplet centre, $\mathcal{V}$ is the total volume of the Voronoi cells for these atoms, and m is the mass of a water molecule. Since in the smallest droplets surface effects extend closer to the centre of droplet, we use $r_c = 0.25$ nm for $N \leq 205$. Fig. 6.11 shows the agreement between d_5 and q_T as functions of ρ for bulk systems and droplets. This shows clearly that the core of the droplets for our range of N is bulk-like. This agreement is supported also by the match between bulk and droplet core q_T, as shown in Fig. 6.11.

6.5 Discussion and conclusions

We estimate the surface tension of water nanodroplets using the TIP4P/2005 model over a wide range of N and T. We do so from an evaluation of the components of the pressure tensor inside the droplets [18] using the coarse-graining method described in Ref. [23]. From the pressure tensor components, we determine the isotropic pressure in the interior of the droplets P_L. This allows us to calculate the surface tension with two approaches: using the Young-Laplace equation directly, and using the variation of the pressure tensor components with distance form the droplet center. The direct route, which we call the thermodynamic route, requires P_L and R_e to estimate γ_s,

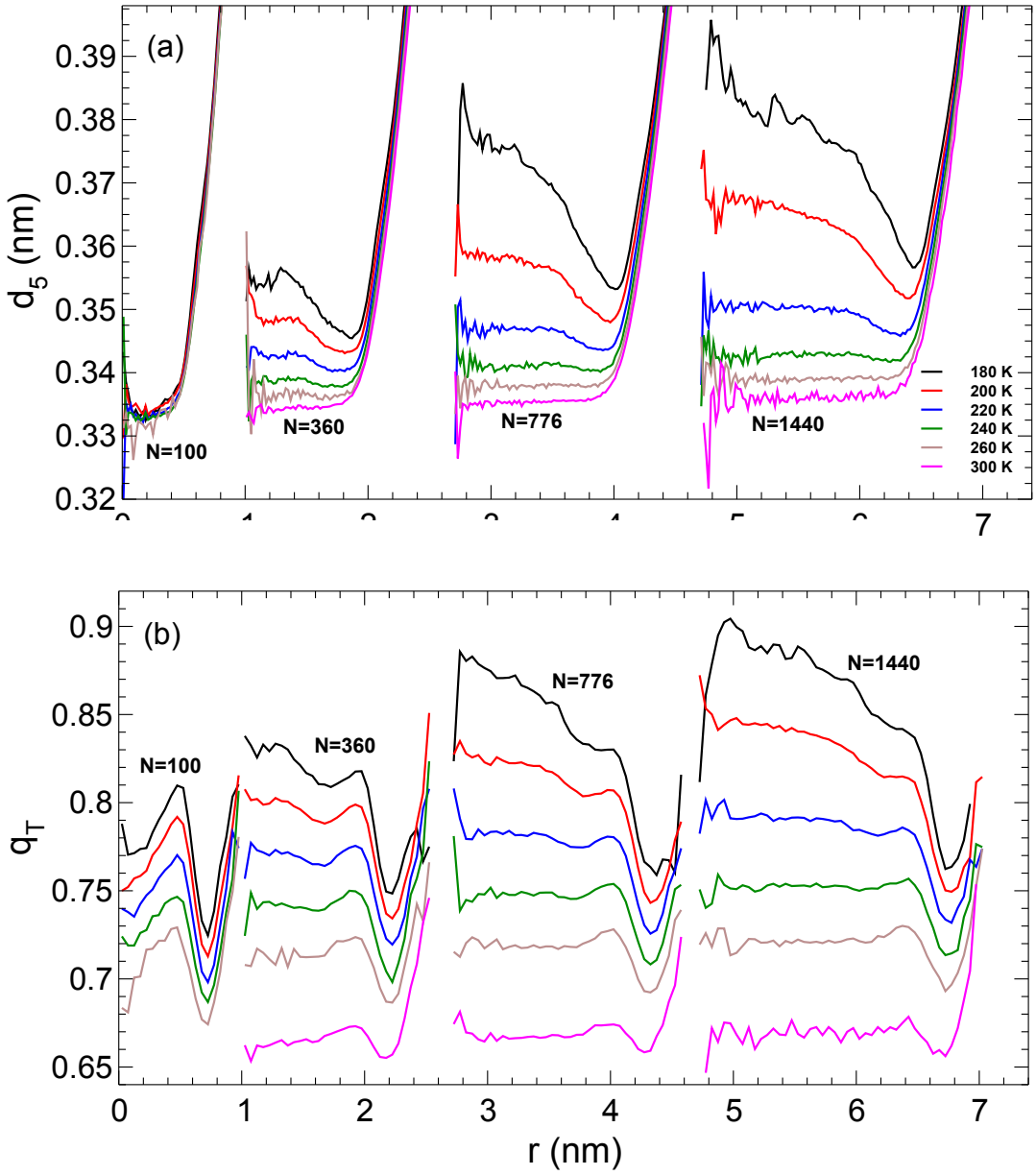

Figure 6.10: (a) d_5 as a function of radius r from the centre of mass for various N and T. The curves have been shifted horizontally by 1 nm for $N = 360$, by 2.7 nm for $N = 776$, and by 4.7 nm for $N = 1440$. (b) q_T as a function of radius r from the centre of mass for various N and T. The curves have been shifted horizontally by 1 nm for $N = 360$, by 2.7 nm for $N = 776$, and by 4.7 nm for $N = 1440$.

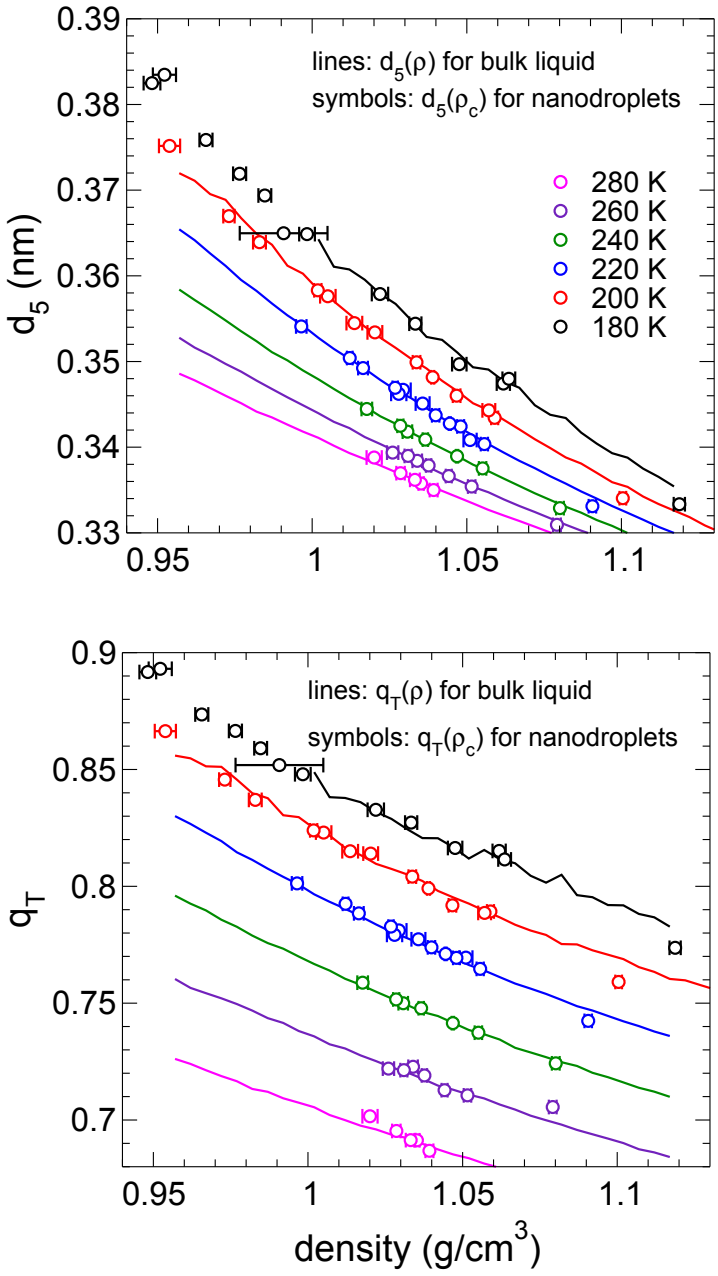

Figure 6.11: Local measures of structure as a function of density.

γ_p and δ as fit parameters, and the mechanical route evaluates γ_s and R_s from the pressure tensor components, and yields γ_p and δ from fitting.

Isotherms of P_L plotted as a function of R_e^{-1} on the assumption that the surface of tension acts at R_e (i.e. that $\delta = 0$) show a linear dependence between P_L and R_e^{-1} that is valid for droplets as small as 0.86 nm in radius. To validate this apparent linearity, we insert the Tolman length correction into the Young-Laplace equation and find that δ is positive and small with a value of 0.055 ± 0.021 nm. Moreover, γ_p values for $T \geq 220$ K from this route, regardless of whether we assume δ is zero or not, are consistent with the extrapolation of γ_p obtained for TIP4P/2005 using the test-area method [24], a thermodynamic method, down to low T, as shown in Fig. 6.7a.

We compute γ_p from the mechanical approach by first finding γ_s and R_s using Eqs. 6.8 and 6.9 (using Eqs. 6.12 and 6.13 produces consistent, but noisier results) and again using Eqs. 6.15 and 6.13. For our range of T and N, we show that γ_s decreases as R_e decreases. Fitting these two sets of results with Eq. 6.2 results in positive and rather large values of $\delta = 0.32 \pm 0.02$ nm from Fig. 6.5a, and $\delta = 0.21 \pm 0.01$ nm from Fig. 6.6a. Although these two values do not overlap within error, they both suggest that δ from the mechanical route is significantly larger than the value from the thermodynamic route. Moreover, estimates of γ_p obtained from fitting mechanical-route results tend to be higher than thermodynamic-route results, as apparent in Fig. 6.7b. However, if we consider γ_s from Eq. 6.15 as a function of R_s^{-1} as shown in Fig. 6.6a, the γ_p resulting from fitting with Eq. 6.2 is consistent with the thermodynamic route and with Vega and de Miguel's extrapolation for $T \geq 240$ K.

We also conclude that γ_s from the thermodynamic route remains relatively constant as we vary R_e for $T \geq 220$ K, but shows larger variation at $T = 200$ and 180 K, where it changes by 15% over the range of droplet sizes we use. In contrast, γ_s from the mechanical route increases significantly with R_e , resulting in almost 50%

change in γ_s at $T = 180$ K. These results are equivalent to δ being small for the thermodynamic route and large for the mechanical route.

At 300 K, our thermodynamic results for γ_s as a function of droplet size are consistent with those of Lau *et al* [15], while those from the mechanical route are not. One might conclude, therefore, that the mechanical route for determining γ_s and δ lacks validity, and the relatively large value of $\delta = 0.2$ - 0.3 nm should be rejected in favour of the smaller value of $\delta \approx 0.06$ determined from the thermodynamic route. However, as δ is the difference between R_e and R_s, which is understood to be where the surface tension acts, values in the range of 0.2 to 0.3 nm are reasonable given the locations of R_e and the negative pressure minima in Fig. 6.1. Our work confirms the discrepancy between the mechanical and thermodynamic routes that has been previously noted in the literature, and so supports the need for a better theoretical understanding of the connection between the two.

The marked increase in γ_p for $T < 220$, as shown in Fig. 6.7, approximately coincides with the crossing of the Widom line at $T = 230$ K as $R \to \infty$ and $N \to \infty$ ($P \simeq 0$), and hence, it may be connected to the LLCP in water. This increase in γ_p is consistent across both the mechanical and thermodynamic routes.

Characterizing how local structure varies with radial distance from the center of the droplet with d_5 and q_T, we see behavior consistent with the formation of a well-ordered random tetrahedral network at low T and large N within droplet interiors. Furthermore, the dependence of these structural measures on local density match that of bulk TIP4P/2005 water. Hence, from a structural perspective, the interiors of our nanodroplets are characteristic of the bulk.

We conclude that γ_s and R_s determined from the mechanical route are smaller than the values evaluated in the thermodynamic route, and this leads to a larger value of δ and planar surface tension γ_p in this route. However, both routes give a positive

value of δ for our range of T and N, and show that δ has no obvious dependence on T. Moreover, assuming the validity of thermodynamic route, for $R_e \geq 1$ nm we can ignore the curvature correction and use the planar surface tension to estimate the Laplace pressure inside water nanodroplets to within 15% down to 180 K. This last point is of practical importance for the estimation of the interior pressure in real water nanodroplet systems.

6.6 Acknowledgments

ISV and PHP thank NSERC for support. Computational resources were provided by ACEnet.

Bibliography

[1] M. Baker, Science **276**, 1072-1078 (1997).

[2] Ø. Wilhelmsen, T. T. Trinh, A. Lervik, V. K. Badam, S. Kjelstrup, and D. Bedeaux, Phys. Rev. E **93**, 032801 (2016)

[3] H. Ohno, N. Nishimura, K. Yamada, Y. Shimizu, S. Iwase, J. Sugenoya, and M. Sato, Skin Res. Technol. **19**, 375 (2013)

[4] S. Tachibana, A. Kouchi, T. Hama, Y. Oba, L. Piani, I. Sugawara, Y. Endo, H. Hidaka, Y. Kimura, K. Murata, H. Yurimoto, and N. Watanabe, Sci. Adv. **3**, : eaao2538 (2017)

[5] W. Klemperer, and V. Vaida, Proc. Nat. Acad. Sci. **103**, 10584-10588 (2006).

[6] M. Kulmala, Science **302**, 1000 (2003).

[7] P. G. Debenedetti, *Metastable Liquids: Concepts and Principles* (Princeton University Press, Princeton, 1996)

[8] T. Young, Philos. Trans. R. Soc. Lond. **95**, 65 (1805).

[9] P. S. M. de Laplace, Traité de mécanique céleste **4**, 1 (1805).

[10] R. C. Tolman, J. Chem. Phys. **17**, 333 (1949).

[11] A. E. van Giessen and E. M. Blokhuis, J. Chem. Phys. **131**, 164705 (2009).

[12] H. Yan, J .Wei, S. Cui, S. Xu, Z. Sun, and R. Zhu, Russ. J. Phys. Chem. A **90**, 635 (2016).

[13] K. Leong and F. Wang, J. Phys. Chem. **148**, 144503 (2018).

[14] M. N. Joswiak, N. Duff, M. F. Doherty, and B. Peters, J. Chem. Phys. Lett. **4**, 4267 (2013).

[15] G. V. Lau, I. J. Ford, P. A. Hunt, E. A. Müller, and G. Jackson, J. Phys. Chem. **142**, 114701 (2015).

[16] J. S. Rowlinson and B. Widom, *Molecular Theory of Capillarity.* Dover Publications, Inc. New York (1982).

[17] S. M. Thompson, K. E. Gubbins, J. P. R. B. Walton, R. A. R. Chantry, and J. S. Rowlinson, J. Phys. Chem. **81**, 530 (1984).

[18] S. M. A. Malek, P. H. Poole, and I. Saika-Voivod, Nat. Commun. **9**, 2402 (2018).

[19] J. L. F. Abascal and C. Vega, J. Chem. Phys. **123**, 234505 (2005).

[20] H. J. C. Berendsen, D. van der Spoel, and R. van Druren, *GROMACS: A message-passing parallel molecular dynamics implementation.* Comput. Phys. Commun. **91**, 43 (1995); E. Lindahl, B. Hess, and D. van der Spoel, *GROMACS 3.0: A package for molecular simulation and trajectory analysis.* J. Mol. Model. **7**, 306 (2001); van der Spoel, E. Lindahl, B. Hess, G. Groenhof, A. E. Mark, and H. J. C. Berendsen, *GROMACS: Fast, Flexible and Free.* J. Comput. Chem. **26**, 1701 (2005); Hess, C. Kutzner, D. van der Spoel, and E. Lindahl, *GROMACS 4: Algorithms for highly efficient, load balanced, and scalable molecular simulation.* J. Chem. Theory Comput. **4**, 435 (2008).

[21] S.M.A. Malek, R.K. Bowles, I Saika-Voivod, F. Sciortino, and P.H. Poole, Eur. Phys. J. E. **40**, 98 (2017).

[22] I. Saika-Voivod, F. Smallenburg, and F. Sciortino, J. Chem. Phys. **139**, 234901 (2013)

[23] S. M. A. Malek, F. Sciortino, P. H. Poole, and I. Saika-Voivod, J. Phys.: Condens. Matter **30**, 144005 (2018).

[24] C. Vega and E. de Miguel, J. Chem. Phys. **126**, 154707 (2007).

[25] J. L. F. Abascal and C. Vega, J. Chem. Phys. **133**, 234502 (2010).

[26] P. H. Poole, F. Sciortino, U. Essmann, and H. E. Stanley, Nature **360**, 324 (1992).

[27] C. Yang, S. Jang, and Y. Pak, Nat. Commun. **5**, 5773 (2014).

Chapter 7

Summary and Future Work

7.1 Summary

The structure, anomalies, and surface tension of water nanodroplets are studied carefully in this thesis. Extensive MD simulations are performed using the TIP4P/2005 potential to study water nanodroplets over a wide range of N and T. To ensure that the nanodroplets are in equilibrium, two methods have been adopted in these simulations. The conventional "single long run" (SLR) simulations and the new "swarm relaxation" method developed in Ch. 3. Using the swarm relaxation strategy, the completely independent microstates that feed into the analysis of ensemble averages make the determination of equilibrium quantities and their uncertainties required to study water nanodroplets very precise. The ease of conducting the runs in this method, the lack of ambiguity in computing the error bars, and the significant reduction of wall time required to obtain equilibrated configurations are all convincing reasons that with the availability of computational resources, the swarm relaxation method can expedite the production of equilibrated and trusted configurations of simulated systems. However, for new or complex systems, SLRs may be needed. Although the

potential energy autocorrelation is used to monitor the individual runs in the swarm relaxation method, any observable autocorrelation can be used. In case of limitations on the availability of computational resources, asynchronous or extended swarm relaxation runs to generate independent configurations within individual runs can be adopted. After harvesting configurations using both methods, all desired quantities are obtained.

Studying the anomalies of water in nanodroplets and their relation to the proposed LLPT can be achieved by computing many quantities, such as R, ρ, and P_L. The local pressure inside nanodroplets is calculated using our modification of a coarse-graining pressure tensor method explained in detail in Ch. 4. The modified method enables us to probe the pressure inside nanodroplets and whether it shows signs of bulk-like behaviour without prior assumptions. Once the pressure tensor and density inside nanodroplets are evaluated, we can study many properties and anomalies inside simulated water nanodroplets.

We find that water nanodroplets show bulk-like liquid properties and reproduce bulk water anomalies, such as density maximum. By varying N, water nanodroplets explore a wide range of density and pressure. The EOS of bulk and nanodroplet water agree for $T \geq 220$ K, and depart for $T \leq 200$ K. This departure arises as T approaches T_c for the LLPT that occurs in TIP4P/2005. This departure is accompanied by the emergence of complexity in structure going from surface to the interior. We also observe that the interior density of some N do not reach the bulk value at low T because of the influence of the denser layer at the surface. Moreover, we find that when $P_L < P_c$, the nanodroplets show inverted density gradients at low T. These changes in density and pressure profile may influence the role of water nanodroplets in essential systems and applications, such as chemical activities of solute molecules inside the nanodroplet. And for these findings, we propose the utilization of water

nanodroplets to probe liquid water properties in extreme temperature conditions as the small size of water nanodroplets suppresses nucleation, while bulk water fails to remain in the liquid state below approximately 232 K.

Motivated by the structural complexity and the appearance of HDL-like and LDL-like environments within nanodroplet interiors depending on the size and temperature, we find the surface tension from two approaches, mechanical and thermodynamic routes. We find that the mechanical route gives smaller values of γ_s and R_s and a larger value of δ. Fitted values of γ_p obtained by this route are higher than the planar surface tension of TIP4P/2005 calculated from the thermodynamic route and by Vega *et al*. We also show, assuming the validity of the thermodynamic route, that for water nanodroplets of radius as small as 1 nm, the curvature dependence of surface tension can be ignored, and that it can be approximated by the planar surface tension. Moreover, we find a sudden increase in γ_P as a function of T from both routes. This increase coincides with crossing the Widom line and therefore likely arises from the emergence of a more LDL-like network in the interior.

7.2 Future work

A clear liquid-liquid phase transition in nanodroplets may be observed by imposing a vapour pressure on the biggest nanodroplets in this thesis. The vapour pressure can be simulated by filling the box with an inert gas, i.e. a gas that will not not penetrate the droplet.

A comprehensive study of water nanodroplets requires understanding crystal nucleation within water nanodroplets and the connection to their thermodynamic and structural anomalies. The nucleation within water nanodroplets can be studied through umbrella sampling MC techniques [1]. Using both MC and MD, the nucleation rates

can be determined.

Supercooling water nanodroplets might subject the nanodroplets to slow dynamics in the interior compared to the surface. Therefore, characterizing the dynamics as a function of radius in the nanodroplets is also important for understanding the nucleation process.

The vitrification of water nanodroplets can be studied through two techniques, normal supercooling where the nanodroplet is cooled from a temperature close to melting to a very low temperature, while the other technique uses vapour deposition, where the glassy nanodroplet is formed by successive deposition of a few water vapour molecules onto a growing cluster. One fundamental question is whether the vapour deposition technique can access low energy states that are inaccessible through normal supercooling [2].

Bibliography

[1] D. Frenkel and B. Smit, *Understanding Molecular Simulation: From Algorithms to Applications* (Academic, New York, 2002).

[2] W. Qi and R. K. Bowles, ACS Nano **13**, 3416-3423 (2016).